MECHANICAL PROPERTIES OF ST. PETER SANDSTONE
A COMPARISON OF FIELD AND LABORATORY RESULTS

A THESIS
SUBMITTED TO THE FACULTY OF THE GRADUATE SCHOOL
OF THE UNIVERSITY OF MINNESOTA

BY
MICHAEL EUGENE DITTES

IN PARTIAL FULFILLMENT OF THE REQUIREMENTS
FOR THE DEGREE OF
MASTER OF SCIENCE

DECEMBER, 2015

This thesis contains previously published material (Appendix E) in the “Journal of Geotechnical and Geoenvironmental Engineering” © 2002 ASCE.

All other material © 2015 Michael E. Dittes

All Rights Reserved.

ACKNOWLEDGMENTS

I would like to extend my thanks to those, who without their help I would not have been able to bring this project to completion.

First and foremost, I thank Professor Joseph Labuz who took a chance on me, by offering me a TA-ship. Through my time in school, Joe helped me stay focused when I started to move off on tangents, offered timely advice, and over the years has become much more than my advisor. I am proud to think of him as a friend.

Professors Andrew Drescher and Peter Huddleston also deserve special thanks for providing critical review of my work, and agreeing to sit on my thesis committee.

To Ms. Tiffany Ralston who had an uncanny way of knowing what I needed to do, and how, before I knew myself.

To Charles Nelson who helped me streamline my thesis project and helped me gain access to the Minnesota Library Archives construction site.

To my fellow graduate students with whom I debated, joked and laughed, you helped me see things that I was missing. Your input was invaluable and you have my deep appreciation.

To my parents who always pushed myself, and my sisters, to never stop learning and achieving. Thank you.

Finally, to my wife Chantale a very special thank you. She has supported me while seeing the best and the worst of me, without flinching, and her talents in everything Word was indispensable in completing this work. You are my friend and my love.

DEDICATION

This work is dedicated to my late father, Richard E. Dittes, who constantly pushed me to “finish what I start.”

Through the twists and turns in life, I did not forget that advice, and though it has taken some years, this project is finally complete.

This one is for you, Dad.

ABSTRACT

The St. Peter sandstone is an arenaceous, ortho-quartzitic, sublittoral cratonic sheet sand of middle Ordovician age. It is remarkable in geographic extent, mineralogical composition, thickness and engineering properties. A vast majority of its extent is buried; only in the Upper Mississippi River valley is it readily exposed.

The St. Peter sandstone behaves as a locked sand, a nearly cohesionless geo-material characterized by brittle behavior, a lack of interstitial cement, and high dilation rates at failure. When confined it is capable of supporting large loads with small deformations, even under saturated conditions, yet when confinement is removed it disintegrates and readily flows. Dry intact samples have a uniaxial strength of approximately 1 MPa and a Young's Modulus of about 1 GPa. Triaxial tests conducted at confining pressures of less than 150 kPa yield an angle of internal friction of approximately 60°. Because the St. Peter sandstone disintegrates so readily when unconfined, sampling the material is quite difficult.

The St. Peter sandstone has been excavated as foundation material, and for tunnels and sewers, by the cities of Minneapolis and St. Paul for decades. Earliest testing was for those endeavors. As the interest in the design of underground spaces has grown, testing of the St. Peter sandstone has changed to meet that need but testing has been done predominantly in the laboratory.

The purpose of this project was to evaluate the mechanical properties of St. Peter sandstone by comparing in situ tests with laboratory test results. Direct shear tests were conducted to evaluate strength-dilatancy behavior. Transmitted light and scanning electron microscopy were used to help explain the high friction angle of the material. At

low confining pressures the St. Peter sandstone exhibits a friction angle of around 60° but with small cohesion, less than 100 kPa. The high angle of internal friction at failure may be due to locked sand particles or to post-depositional quartz overgrowths. Tests on pulverized, densely packed samples (with void ratios similar to intact samples) and loosely packed samples were conducted in the same fashion as the intact samples and yielded friction angles of approximately 45° and 35° respectively. Pressuremeter tests were performed in situ and the results were interpreted using elasto-plastic analysis. By properly considering system stiffness, a Young's modulus of approximately 0.5 GPa was determined and a friction angle between 60° and 40° was estimated, depending on the assumed dilation angle.

Table of Contents

List of Tables

List of Figures

INTRODUCTION

The last 40 years have brought considerable change to the metropolitan area of Minneapolis-St. Paul. Business and people interact with the Twin Cities from as far away as St. Cloud to the north, Hutchinson to the west, Rochester to the south, and Hudson, WI to the east (Figure 1-1). With this increasing urban area come the associated problems of urban sprawl.

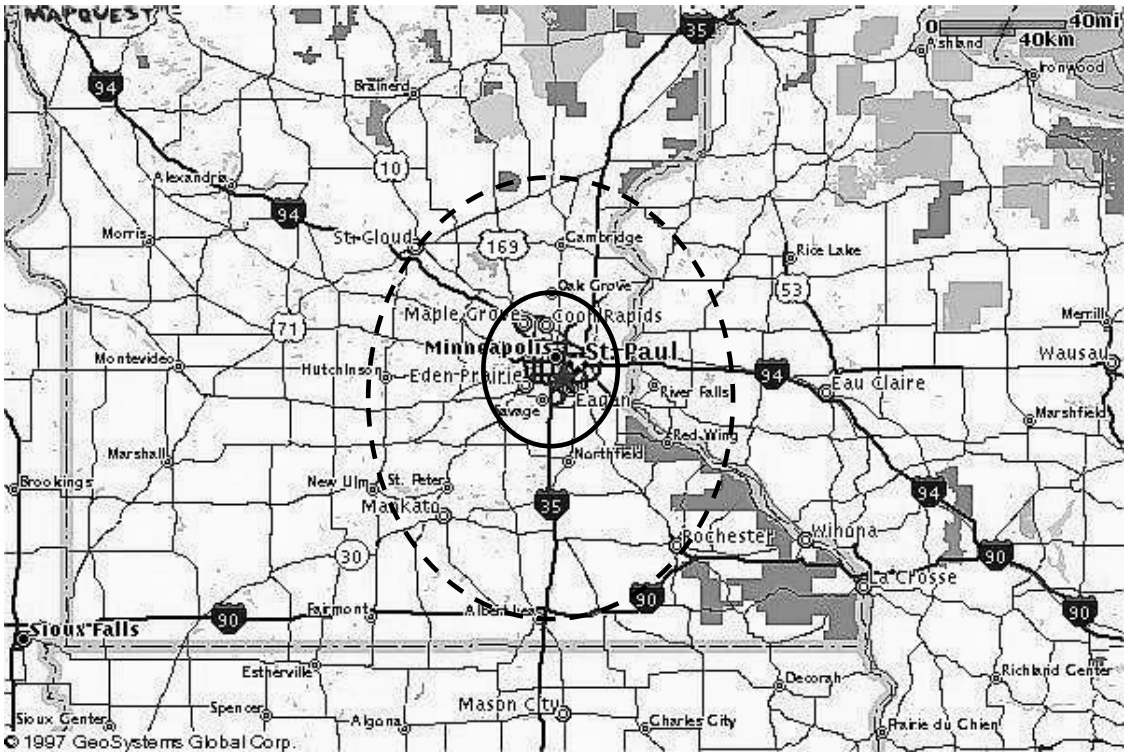

Figure 1-1: Minneapolis-St. Paul metropolitan area showing increases in approximate commuting distances from 1959 to present. Solid oval is 1959, hashed oval is 1999.

The metropolitan area is located on the confluence of the Mississippi and Minnesota rivers. The last glacial period in Minnesota's history (the Wisconsin) is responsible for the development of the Minnesota and Mississippi river valleys. At the close of the Wisconsin glacial period, retreat of the Des Moines lobe had opened up Lake Agassiz and the enlarged water volume dramatically increased the Glacial River

Warren's erosive powers undercutting the Platteville limestone and cutting a gorge that was as much as 54m below the present floodplain (Wright, 1972). Upstream progress of the River Warren Falls was rapid and the Mississippi River at this time was only a tributary of the River Warren.

St. Anthony Falls was formed where Ft. Snelling is now located, and migrated upstream to its present location by undercutting the Platteville limestone as St. Peter sandstone was eroded away in the plunge pool at the base of the falls. The result of ~12,000 years of this activity is a region where the St. Peter sandstone is readily accessible for excavation for the development of underground structures.

The cities of Minneapolis-St. Paul have excavated the St. Peter sandstone for decades as foundation material and for utility and sewer tunnels. Underground excavation for tunnels has been done with low-pressure water jets demonstrating the friable nature of the St. Peter sandstone, and the lower than average cost of excavation as opposed to harder rock formations. The St. Peter sandstone is covered by the Platteville limestone, which is a very competent layer that functions very well as a roof. Located between the St. Peter sandstone and the Platteville limestone is the Glenwood shale, which would be excavated in conjunction with the St. Peter sandstone (Figure 1-2).

With the increase in urban area and corresponding congestion in both Minneapolis and St. Paul, excavating the St. Peter sandstone for light industrial and commercial applications is becoming more feasible as a means of combating urban sprawl. Ease of climate control, and the corresponding monetary savings, is certainly an attractive reason for underground development, as is the aesthetic value of not littering

the landscape with parking lots and storage facilities. In addition, security measures for these structures would be considerably enhanced because access, by the very nature of being underground, would be easily controlled.

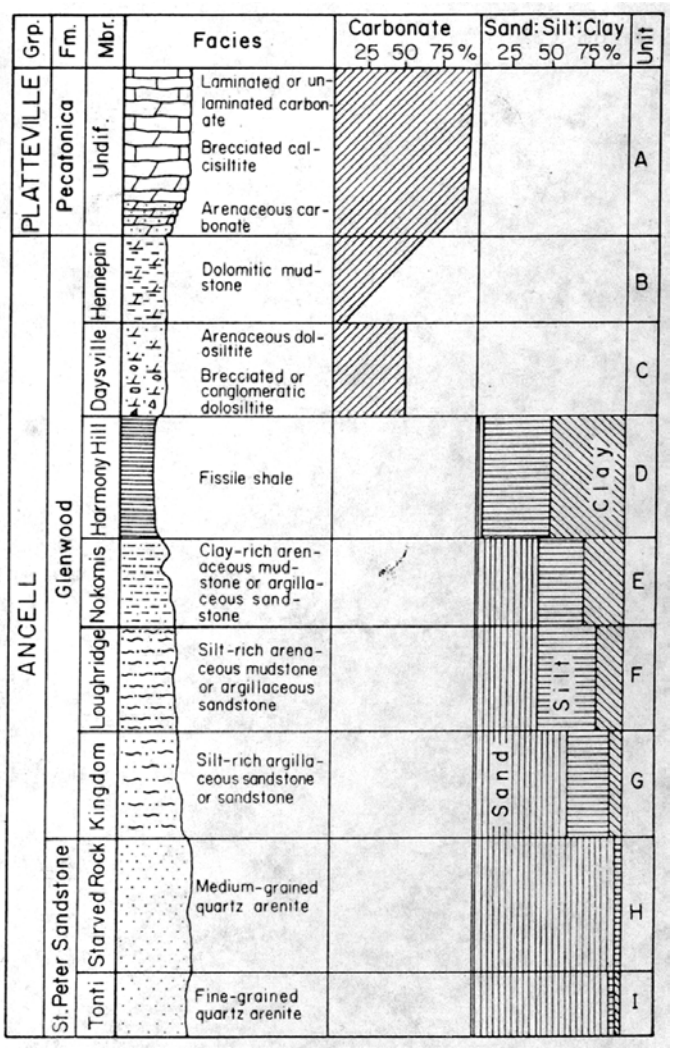

Figure 1-2: Stratigraphic cross-section from the St. Peter sandstone to the Platteville limestone. In the Minneapolis-St. Paul area, the Glenwood shale varies in thickness from several centimeters to approximately one meter (Fraser, 1976).

The St. Peter sandstone is a unique formation that exhibits characteristics of both rock and soil. When confined, it is capable of supporting large loads with small deformations, even under saturated conditions, yet when confinement is removed it

disintegrates and readily flows. The St. Peter sandstone is nearly cohesionless yet shears at friction angles of 59° - 69° (Watson, 1938), with an average value of approximately 63° (Watson, 1938; Labuz, et al., 1996). When dry specimens are subjected to unconfined compression testing, the St. Peter sandstone exhibits low values for unconfined compressive strength (approximately 3 MPa), and Young's modulus (approximately 2 GPa).

Recorded field studies of the St. Peter sandstone have been limited to plate bearing tests (U.S. Army Corps of Engineers, 1952) for foundation design. Analysis of intact and unconsolidated samples for shear strength, and unconfined compressive strength have been confined to laboratory studies under dried conditions (Army Corps of Engineers, 1958; Payne, 1967; and Peterson, 1978) or saturated conditions (Watson, 1938). Analyses of the St. Peter sandstone under in situ conditions seem to be lacking. The purpose of this project is to evaluate mechanical properties of the St. Peter sandstone by in situ testing, and then comparing the in situ test results with laboratory results.

The second chapter of this report will cover the geology of the St. Peter sandstone, paying particular attention to the lithology and mode of deposition to help explain grain size distribution and mineralogy, and the inverse nature of grain shape as a function of grain size. Chapter three concentrates on laboratory analyses used to determine index parameters, grain size distribution, mechanical strength parameters, and permeability. Chapter four covers thin section analysis to establish that the St. Peter sandstone is a locked sand, and to attempt to find evidence of post-depositional quartz overgrowths. Chapter five involves in situ testing using the pressuremeter, and

corresponding analyses for mechanical strength and angle of internal friction. Chapter six lists conclusions.

GEOLOGY

Introduction

Captain Jonathan Carver, while exploring the interior of the continent in 1766-1768, provided the initial description of the St. Peter sandstone. Carver described a cave in sandstone so soft he could cut it with his knife. This cave, named Carver's Cave, is located approximately 48 km (30 miles) down river from St. Anthony Falls. Major Stephen H. Long visited St. Anthony Falls in 1817. His description of the St. Peter sandstone is that of whitish-yellowish sandstone that was so soft Major Long felt it could be described as a sandbank rather than sandstone. Commissioned by the general government is 1820 to explore the sources of the Mississippi River, H.R. Schoolcraft also described the St. Peter sandstone (James, 1894).

Examining a section at Fort Snelling in 1824, Professor William Keating made the first attempt at establishing the depositional environment of the St. Peter sandstone. He described the sandstone as very friable but every fragment seemed to be a regular crystal. This evidence and the apparent lack of fossils is what lead Professor Keating to the conclusion that the St. Peter sandstone was formed by rapid chemical precipitation. Belief in this mode of deposition would endure until 1878 when Professor T. C. Chamberlin discovered fossil remains. This evidence convinced researchers that the mode of deposition of the St. Peter sandstone was mechanical rather than chemical (Sardeson, 1896).

Dr. John Locke also made a report on the St. Peter sandstone in 1839 but it was not until Dr. D.D. Owen, in a paper in 1847, described the geologic formation by name

for the first time. He called it St. Peter's sandstone for the excellent exposures found below Ft. Snelling at the mouth of the St. Peter's River. With the St. Peter's River renamed the Minnesota River, the name St. Peter's sandstone was eventually amended to St. Peter sandstone (Sardeson, 1896).

Geographic Distribution

The St. Peter sandstone is a cratonic sheet sand that covers more than 576,000 km^2 (225,000 square miles) of middle North America. Most of this arenaceous terrain is subsurface (Thiel, 1935; Amaral and Pryor, 1977; Mazzullo and Ehrlich, 1987).

Early efforts to map the St. Peter sandstone were limited to exposures in southeastern Minnesota, northeastern Iowa, the southern third of Wisconsin, and northern Illinois (Sardeson, 1896). The extent of the St. Peter sandstone at the time of deposition is not known. It was generally acknowledged that the St. Peter sandstone was derived from the Potsdam sandstone that outcropped around the southern edge of the Pre-Cambrian Shield but grain-size analysis demonstrates that this was unlikely. The most likely source material comes from pre-Croixian sandstone of the Laurentian Shield (Thiel, 1935). North of Minneapolis-St. Paul, the St. Peter sandstone pinches out in heavily torn and glaciated terrain. The formation dips to the south and is identified through borehole cuttings. The St. Peter sandstone was originally considered to be limited in distribution to the Upper Mississippi Valley (Minnesota, Wisconsin, Iowa, Illinois, and Missouri). It is now recognized that the St. Peter sandstone probably existed into Canada at the time of deposition, extended as far south and west as Nebraska, South Dakota, Kansas, Arkansas, and Tennessee, and extended eastward into Michigan, Ohio and northeastern Kentucky. Studies by E. C. Dapples in 1955 indicate that the St. Peter

sandstone may exist contemporaneously with sandstone units of the Simpson Group. This means that the St. Peter sandstone could possibly exist as far south as the Oklahoma-Texas border (Figure 2-1).

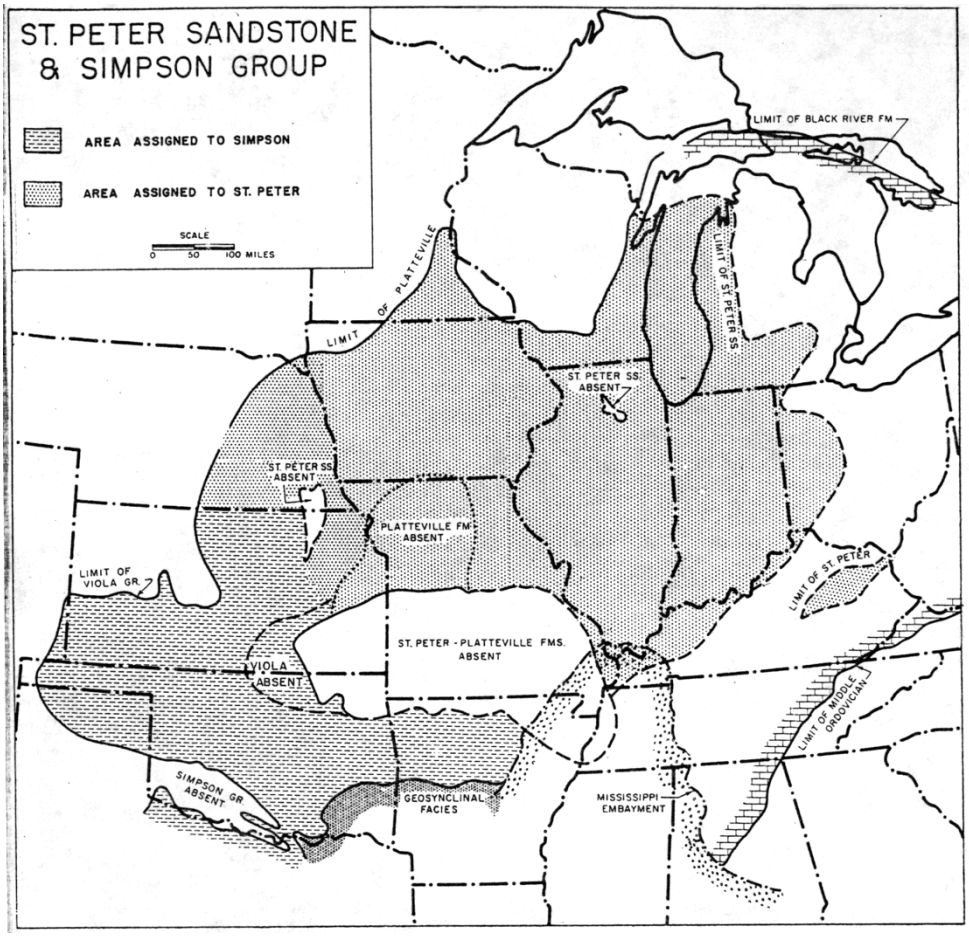

Figure 2-1: Geographical extent of the St. Peter sandstone and the Simpson Group (Dapples, 1955).

Stratigraphic Position

The St. Peter sandstone is Middle Ordovician in age, and in southern Minnesota, southwestern Wisconsin and in Iowa unconformably overlies the Shakopee dolomite of the Lower Ordovician Prairie du Chien group. North of the Twin Cities basin, the St. Peter sandstone unconformably overlies the Jordan sandstone of the Cambrian Croixian series (Figure 2-2).

The St. Peter sandstone itself is composed of two members. The lower unit is the Tonti member, which is a fine-grained quartz arenite with a thin basal unit that contains

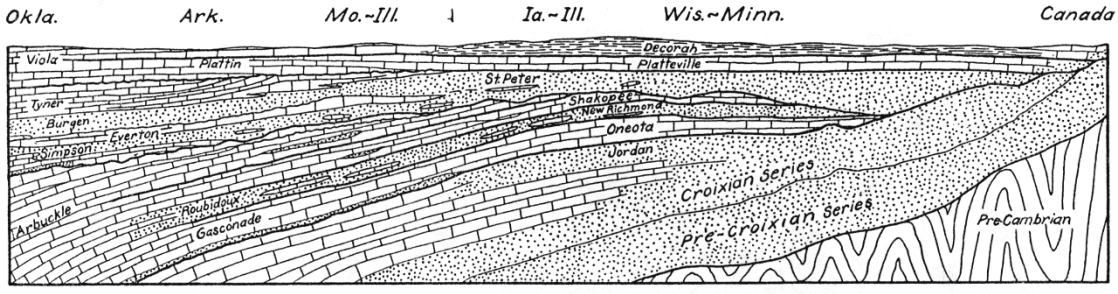

Figure 2-2: Reconstructed cross-section of the St. Peter sandstone showing its relationship with underlying and overlying units (Thiel, 1935).

cross-bedded sandstone, green silty shales, and brecciated limestone and cherty nodules. The upper unit is the Starved Rock member, a medium-grained quartz arenite that grades conformably into the Glenwood formation. Separating the two members is an unnamed band. Originally described as a shale band, it was classified by drill cuttings as a marl-rock zone (Sardeson, 1932) and later reclassified as a silt bed that varies in thickness from approximately 1.5 meters (5 feet) to 9 meters (30 feet) (Thiel, 1935; Schwartz, 1936). The upper contact is a conformable transition crossing three formations marking a lithologic change from quartz arenites of the St. Peter sandstone to sandy shale, shale, and calcareous shale of the Glenwood formation to shallow water carbonates of the Platteville limestone (Schwartz, 1936; Fraser, 1976).

Thickness

The St. Peter sandstone varies in thickness from several centimeters in eastern Wisconsin to greater than 150 meters (500 feet) at Joliet, Illinois (Thiel, 1935). Throughout its distribution, the St. Peter sandstone averages 30 meters (100 feet) in thickness. In the Twin Cities basin, measurements from 57 wells have resulted in an

average thickness of 48 meters (158 feet). Lateral variations in thickness are extreme, and the St. Peter sandstone may vary in thickness by 30 meters (100 feet) in as little as 0.4 km (0.25 miles) (Thiel, 1935).

Lithology

The St. Peter sandstone has a SiO_2 content that is approximately 99% on average. The silica is in the form of clear limpid grains of quartz (Sardeson, 1896). The sandstone is extremely friable with almost no cementing material of any kind. However, irregular masses are cemented with calcium or silica (Schwartz, 1936) and form dense sandstone. The sandstone is typically white but where water is able to infiltrate, iron oxide stains the sand grains yellow, brown or red (Sardeson, 1896). Sand grains are cemented by iron oxide into dark brown nodules that are dense and hard (Figure 2-3).

Figure 2-3: Iron-oxide nodules found in the St. Peter sandstone.

Chemical analyses (Table 2-1) performed throughout its geographic extent show a remarkable consistency in SiO_2 content (average content is 98.83%). This indicates that the St. Peter sandstone is pure silica sand. Because of the purity of the St. Peter sandstone, heavy accessory minerals are all but absent (Thiel, 1935). To obtain sufficiently large numbers of heavy minerals needed for analysis, several 111 N (25 lb) bags of samples have been separated mechanically and the heavier fractions retained and analyzed (Table 2-2). Heavy accessory minerals appear in the following order of abundance; zircon, tourmaline, rutile or leucoxene, garnet, and hypersthene, titanite, xenotime monozite, ceylonite, and anatase (Thiel, 1935).

Table 2-1: Chemical analyses of St. Peter sandstone (Thiel, 1935).

Sample Number	SiO_2	Al_2O_3	$Fe2O_3$	FeO	MgO	CaO	Na_2O	K_2O
1*	98.91	0.62	0.09	n/d	0.02		0.01	0.02
2	99.78	n/d	trace	n/d	trace	n/d	n/d	n/d
3	97.67	1.31	0.55	n/d	n/d	0.41	0.15	0.02
4**	97.39	1.25	0.24	0.07	n/d	n/d	0.02	0.36
5	96.74	0.71	1.45	n/d	0.11	0.84	n/d	n/d
6	98.64	1.10		n/d	n/d	n/d	n/d	n/d
7	98.66	0.39	n/d	0.16	0.18	0.45	n/d	n/d
8	99.82	0.05		n/d	n/d	0.13	n/d	n/d
9	98.58	0.28	0.09	n/d	0.00	0.02	n/d	n/d
10	99.89	0.05	trace	n/d	0.01	n/d	n/d	n/d
11	99.45	0.30		n/d	trace	0.13	n/d	n/d
12	99.89	0.05	n/d	n/d	0.01	n/d	n/d	n/d
13	99.07	0.46	0.11	n/d	0.16	0.01	n/d	n/d
14	99.40	0.98	0.05	n/d	0.07	0.16	n/d	n/d
15	99.61	0.04	0.08	n/d	0.07	0.07	n/d	n/d
16	99.70	0.01	0.06	n/d	0.06	0.06	n/d	n/d
17	97.60	0.20	0.10	n/d	0.22	1.02	n/d	n/d
18	98.41	0.43	0.28	n/d	0.00	0.15	n/d	n/d
19	98.39	0.29	0.30	n/d	0.00	0.02	n/d	n/d
20	99.08	0.26	0.06	n/d	0.00	0.00	n/d	n/d

*TiO2=0.05%
**TiO2=0.10%
1. Mendota, MN
2. South St. Paul, MN
3. Fort Snelling, Minneapolis, MN
4. "Green Sand" layer 5 feet from top of layer in North Minneapolis, MN
5. Mineral Point, WI
6. Wisconsin
7. Wisconsin
8-12. Illinois
13. Perryville, MO
14. Franklin County, MO
15. Jefferson County, MO
16. St. Charles County, MO
17. Jefferson County, MO
18. Sidney, AR
19. Pilot Knob, AR
20. Wilcockson, AR

Iron minerals appear as Fe_2O_3 and FeO in order of abundance. These mineral occurrences are mostly limited to the top 6 meters (20 feet) of the St. Peter sandstone. They appear in horizontal bands ranging from approximately 2 to 15 centimeters (1 to 6 inches) in thickness (Thiel, 1935). Examination shows the sand grains to be stained by limonite. It is possible that the iron was deposited by infiltration along bedding planes or, as is hypothesized by Dake (1921), each band represents an exposed surface where

standing water remained for a sufficiently long period of time to allow oxidation of Fe-solutions to stain the sand grains. Below a conspicuous layer of green sand, iron staining of the sand grains diminishes rapidly with depth. Just below this green sand layer the

Table 2-2: Average percentages of heavy minerals by weight in the St. Peter sandstone (Thiel, 1935).

Location of samples		Number of samples	Percent by weight of heavy minerals
Geographic	Stratigraphic		
Caledonia	Upper 50 feet	5	0.0177
Castle Rock	Upper 40 feet	4	0.0066
Chatfield	Upper 40 feet	4	0.0057
	90 feet from top	1	0.0045
Chimney Rock	Upper 30 feet	2	0.0283
Decorah, Iowa	Upper 30 feet	3	0.0107
Mendota	Upper 50 feet	5	0.0156
N. Minneapolis	Upper 20 feet	2	0.0587
Zumbrota	80-110 feet from top	3	0.0062
Preston	15 feet from base	1	0.0045
Rochester	Upper 40 feet	2	0.0112
Illinois*	.....	15	0.0407
Arkansas	.....	11	0.0120
Missouri	Upper 50 feet	6	0.0240

highest occurrence of iron-nodules are found. These iron nodules also diminish rapidly in size and number with depth (Figure 2-4).

The green sand layer is approximately 20 centimeters (8 inches) thick, and is observable throughout the Twin Cities area (Payne, 1967). It is hard when dry and forms a relatively impermeable boundary. The author viewed perched water in several locations while cutting sandstone samples for laboratory analysis. This layer shows irregular patches of clean sand and green clay. X-ray diffraction of the green clay shows well-defined peaks for illite (Payne, 1967).

Structure

The St. Peter sandstone can be divided into two facies based on grain size and sedimentary structures (Fraser, 1976). The lower member, the Tonti member, is finer grained than the Starved Rock member and exhibits marked changes in structure moving

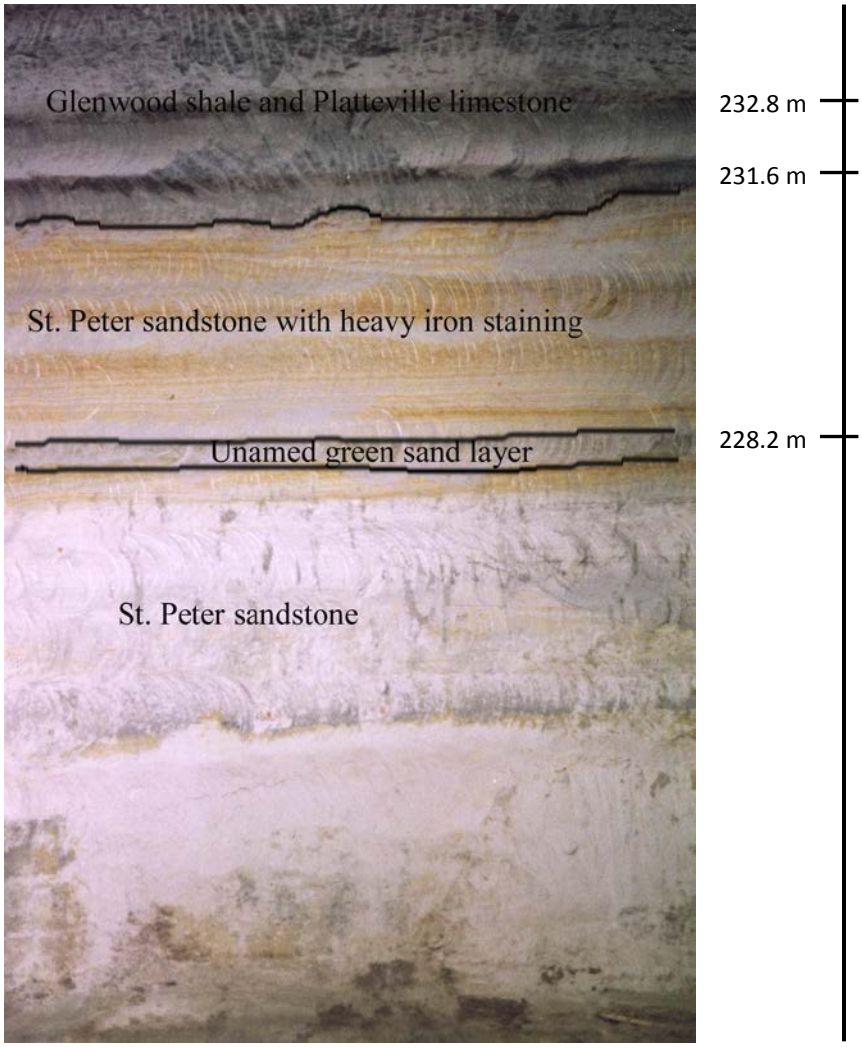

Figure 2-4: Stratigraphic sequence from St. Peter sandstone to Platteville limestone. The photo is of the west face, just inside the entrance at the bottom of the bluff along the Mississippi River.

north to south. In Illinois, the Tonti member exhibits structure similar to sublittoral sheet sandstones with thin beds, wavy bedding planes, and small amounts of silty laminae. The Tonti member shows extensive burrowing that has been filled with coarse material (Goldring, 1966). In south-central Wisconsin, the St. Peter sandstone is more coarse grained compared to north-central Illinois, and exhibits tabular and concave upwards cross strata that is as much as 15 meters (49 feet) thick (Fraser, 1976). These features are postulated to be analogous to the formation of sand waves on the tide-dominated North Sea shelf (Pryor and Amaral, 1971; Dott and Roshardt, 1972). The Tonti member in southwestern Wisconsin and southeastern Minnesota exhibits large and small-scale trough cross strata (Fraser, 1976). The general trend of these strata is agreed to be northeast to southwest following longshore currents moving along northeast-southwest oriented shorelines. (Dapples, 1955). Extensive examination of these sedimentary structures by Dott and Roshardt (1972) show a preferred orientation to the southwest for the large sets of approximately 260° and the trough axes plunge significantly to the northwest. The small sets were determined to be complex, and may even be randomly oriented (Dott and Roshardt, 1972). In the Minneapolis area, large and small-scale trough cross-strata and low angle planar cross-strata are evident indicating a shoreline environment for the deposition of St. Peter sandstone (Fraser, 1976).

The Starved Rock member is medium to coarse grained and may be divided into five structural zones based on characteristic sequences of bedding structures from the base upward:

1) small-scale trough and tabular cross beds;
2) large-scale tabular to convex upward cross beds;

3) large-scale trough cross beds;
4) alternating beds of low-angle, small-scale trough cross beds and beds of irregular horizontal laminae; and
5) apparently massive beds (Fraser, 1976).

These structures compared to modern structures indicate that the Starved Rock member is not tidal, eolian dune, fluvial or deltaic in origin (Fraser, 1976). Characteristics of tidal zones and eolian dunes are lacking, and while many of the structures associated with fluvial environments are present, the sequence is reversed. In addition, the Starved Rock member is an elongate sand body parallel to the shoreline of the basin it was deposited in, and it laterally separates the Glenwood formation to the north and the Joachim and Dutchtown formations to the south. The Starved Rock member was deposited in progressively shallower water upward in section, and it overlies deepwater deposits. All this indicates that the Starved Rock member was deposited in a backwater region behind a barrier island system (Figure 2-5).

The clear whiteness of the sandstone gives it the appearance of being massive (Sardeson, 1896) but fissures are present. These fissures run parallel to bedding (Figure 2-6) and also are vertical (Figure 2-7). The vertical fissures trend northwest to southeast, and seems to run parallel to seams in the overhead Platteville limestone. The fissures probably started out as tight joints and seams while the St. Peter was covered with possibly hundreds of meters of overlying sediments (Schwartz, 1939). These joints and seams are most likely the result of regionally mild deformational events, such as isostatic adjustments in the basin or far reaching orogenic events such as the Alleghanian orogeny. In addition to the fissures, caves are present in the St. Peter and may be more than a

kilometer in length. These caves are irregular in shape and size, and are always found at the top of the Starved Rock member with the Platteville limestone acting as the roof. The sides are nearly vertical and rubble is found on the floors (Payne, 1967). The rubble is most likely Glenwood shale, which is expansive, and separates and detaches when confinement is removed. The caves locations are near present river channels, and outlets to the river may have existed and later backfilled (Schwartz, 1936).

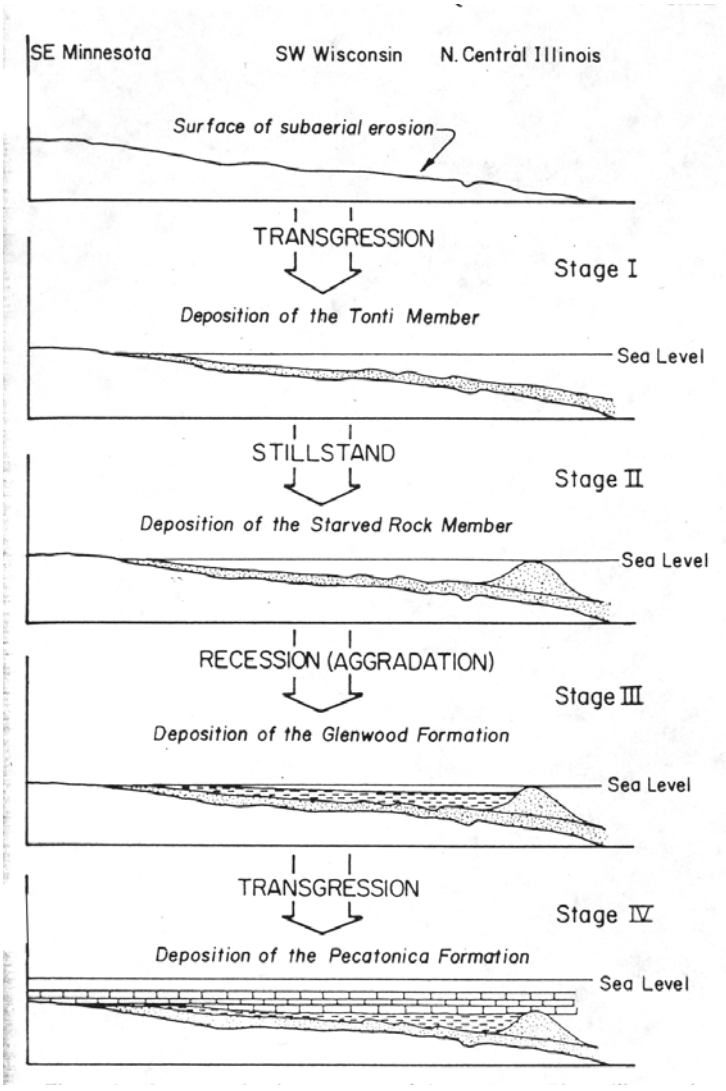

Figure 2-5: Depositional sequence of the St. Peter sandstone through the Platteville limestone (Fraser, 1976).

Depositional Environment

The determination of the processes responsible for the deposition of early Paleozoic cratonic sheet sands remains problematic because pre-Devonian transport processes on cratonic shelves have no clear-cut Holocene analogues (Dott and Byers, 1981; Mazzullo and Ehrlich, 1983). This difficulty is due in large part to the inability to study the formation using traditional field and laboratory methods.

Figure 2-6: The north wall of cavern 1 showing a horizontal seam in the St. Peter sandstone.

The North American continent was large, mature, and wind-swept during Pre-Devonian times with little binding vegetation resulting in eolian processes being dominant in surficial erosion and sediment transport. Due to the lack of topographic relief, streams of the time were broad, shallow, and poorly channelized, and did not make a significant contribution to continental erosion and sediment transport (Cotter, 1978). These sands are composed almost entirely of quartz, show few size trends vertically or laterally,

contain few intercalations of other lithologies, and many times lack recognizable structures. The St. Peter sandstone is a classic example of this homogeneous, featureless, problematic lithology (Mazzullo and Ehrlich, 1983).

Early efforts to determine the St. Peter sandstone's depositional environments (prior to 1935) were limited because standard petrographic procedures had not yet been developed and grain-size texture was limited to crude industrial terms such as

Figure 2-7: View of west wall of cavern 1 showing vertical jointing in the St. Peter sandstone.

"fineness," "effective size," and "uniformity coefficient" (Amaral and Pryor, 1977). Work by Thiel (1935) was the first attempt to categorize the St. Peter in statistical terms applicable to sedimentology, but these studies were limited to sampling procedures that were applicable to industrial purposes but not for sedimentological study. These sampling methods, such as channel sampling, destroyed characteristic grain-size distribution because the depositional units were mixed together (Amaral and Pryor, 1977).

Later efforts at textural analysis and depositional environments were based on bivariate grain-size parameter combinations and linear discriminant functions. These methods were judged inadequate because of inherent flaws in these methods. Texture analysis based on cumulative probability curve techniques of Sindowski (1957) and Visher (1969), and stratigraphic variations in single grain-size parameters led to a shallow marine sand bank as a predicted final depositional environment for the St. Peter sandstone (Amaral and Pryor, 1977).

Further efforts by Mazzullo and Ehrlich (1980, 1983) using Fourier grain shape analysis and grain morphology, which include grain roundness and surface textures, determined that eolian processes, along with fluvial-deltaic processes were the transport mechanisms for the sandstone's source material (Figure 2-8). Sampling at close discrete intervals indicated that the St. Peter may not have been deposited in a continuously transgressive sequence but may have been the result of brief, incorporated regressions which would have contributed greatly to the thickness of the unit (Mazzullo and Ehrlich, 1980).

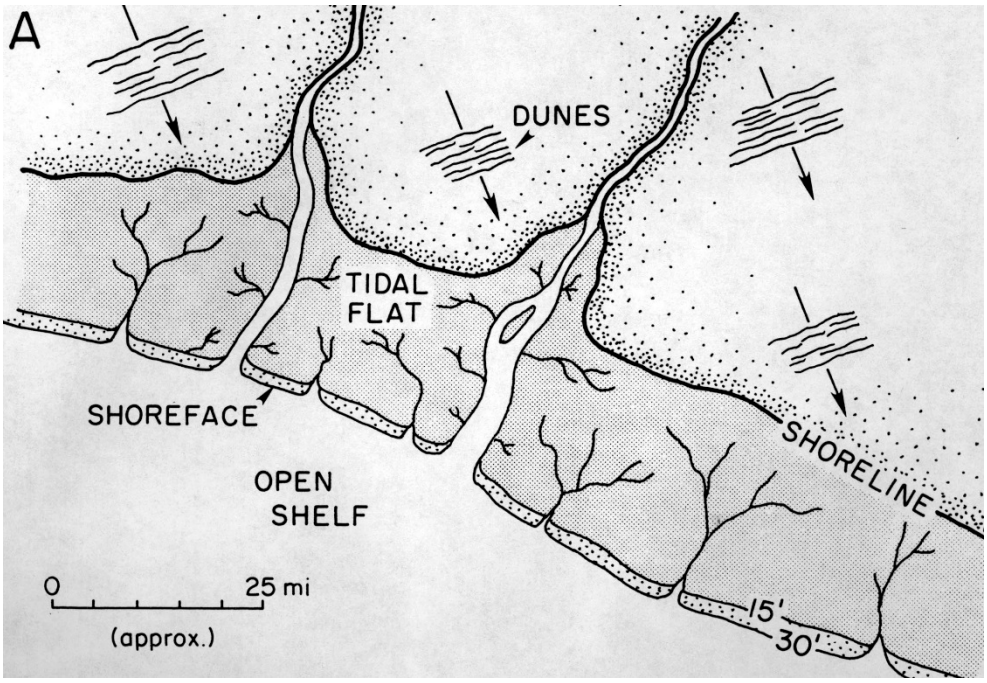

Figure 2-8: Transport mechanisms for deposition of the St. Peter sandstone (Mazzullo and Ehrlich, 1983).

Petrography

The St. Peter sandstone is an arenaceous, ortho-quartzitic, sublittoral sand sheet of remarkable mineralogical composition and grain size uniformity. Its appearance is very conspicuous, and the white to gray smooth cliff faces (Figure 2-9) and hummocky topography (Figure 2-10) make it an easy formation to identify visually. The mineralogy of the St. Peter is unusual in that it is essentially made up of pure quartz (98.83% SiO_2 on average) with trace amounts of heavy accessory minerals, iron oxides, feldspars, and clay. A number of years ago, a petrographic analysis of the clay minerals was performed by the University of Minnesota Mineral Resource Research Center, and the test results showed the clay composition to be kaolinite, illite, and montmorillonite, with possible minor amounts of vermiculite. Samples were taken from 16 sites throughout southern Minnesota, and tests showed the distribution of these clay minerals varied drastically in

quantity and variety from site to site both laterally and vertically (Parham, 1970). In addition, minor amounts of detrital feldspars were found (Figure 2-11).

Figure 2-9: Outcrop of St. Peter sandstone found on Shepard Road next to the Interstate 35-E overpass.

Figure 2-10: Characteristic hummocky topography located at the entrance to the Crosby Farm Nature Center.

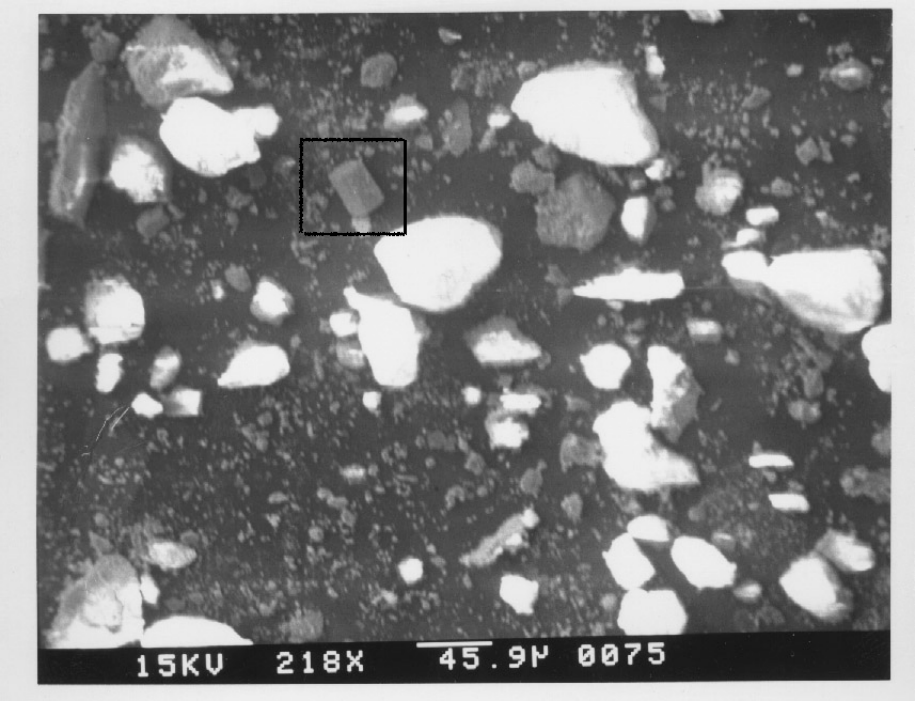

Figure 2-11: Detrital feldspar grain located in St. Peter sandstone fines. Note the angularity of the quartz grains.

Another unique quality of the St. Peter sandstone is that unlike most sandstones or sand deposits, the grains of the St. Peter sandstone become more angular as the grain size decreases. This is a reversal of normal grain shape patterns where the grains become more rounded as they decrease in size. This reversal in grain shape could be the result of preferential transport mechanisms of Pre-Devonian times. The lack of binding vegetation and flat, mature continents result in eolian mechanisms being the dominant means of material transport. Rivers of Pre-Devonian times were broad, shallow and exhibited very low hydraulic gradients. The result is that they were incapable of transporting anything but the smallest grains downstream. Eolian transport mechanisms are the most efficient at eroding and rounding angular material. Fluvial transport mechanisms are not nearly as efficient at rounding angular grains.

Economic Value

The St. Peter and Oriskany sandstones of early Paleozoic age are the two most important sources of glass-sand in the central and eastern United States. These two sources supply 30% of the glass-sand production of the United States (Heinrich, 1981).

INDEX PROPERTIES

Specific Gravity, G_s

Previous reports provide a number of values for G_s of the St. Peter sandstone (Table 3-1). Specific gravity tests were performed in accordance with ASTM D 854

Table 3-1: Previously recorded specific gravity values.

Author or Agency	G_s
Us Army Corps of Engineers, 1939	2.64
Payne, 1967	2.67

and AASHTO T 100 procedures, and the tests were carried out using a 1000ml volumetric flask and a model 911 Nelson vacuum pump. Following these procedures, and using the expression

$$G_s = \frac{\alpha M_s}{M_{bw} + M_s - M_{bws}} \qquad (3\text{-}1)$$

where M_{bw} = the mass of the flask and water (g)

M_{bws} = the mass of the flask, water and sample (g)

M_s = the mass of the sample (g), and

α = the water density correction factor.

An average value for the specific gravity of $G_s = 2.63$ was obtained (Table 3-2). This value for specific gravity is consistent with the values previously reported.

Table 3-2: Results of specific gravity tests performed on pulverized St. Peter sandstone.

Test	T_W (^oC)	M_{bw} (g)	M_{bws} (g)	M_{s+EV} (g)	EV#	M_s (g)	α	G_s
1	23	759.26	830.29	542.86	2	115.44	0.9993	2.60
2	23	761.86	827.92	544.96	1	105.57	0.9993	2.67
							G_s (avg) = 2.63	

Unit Weight, Porosity, and Voids Ratio

Publications dealing with the St. Peter sandstone have been incomplete concerning unit weight, porosity, and voids ratio (Table 3-3). No author or agency has recorded values for these three index properties in the same publication.

Table 3-3: Recorded values for dry unit weight, porosity and voids ratio for St. Peter sandstone.

Author or Agency	γ_{dry}	n (%)	e
Giles, 1930	N/A	N/A	0.388 - 0.459
Thiel, 1935	N/A	26.8 - 31.1 (28.3 avg.)	0.394 (avg.)
Watson, 1938	N/A	N/A	0.41 - 0.46 (0.438 avg.)
Schwartz, 1939	N/A	25 - 30	N/A
US Engineer Sub-Office, Hydraulic laboratory, Iowa City, Iowa, 1939	N/A	N/A	0.283 - 0.296 (0.289 avg.)
US Army Corps of Engineers, St. Paul District , 1952	18.0 - 19.6 kN/m^3 (115 - 125 pcf)	N/A	N/A
Payne, 1967	19.9 kN/m^3 (avg.) (126.4 pcf avg.)	27 - 31 (28.3 avg.)	N/A
Dusseault, 1977	N/A	25.8 - 28.5	N/A
Dusseault and Morgenstern, 1979	N/A	27.0 (avg.)	N/A
University of Waterloo, 1996	N/A	N/A	0.330 - 0.450 (0.391 avg.)

The index property of dry unit weight (γ_d) can be calculated from the expression

$$\gamma_d = \frac{Mg}{V} \qquad (3-2)$$

where γ_d = dry unit weight, M = mass of sample (kg), g = force of gravity (m/sec^2), and V = volume of the sample (m^3).

Porosity (n) is calculated from the unit weight and an experimentally determined value for specific gravity. The expression used to calculate n is

$$n = 1 - \frac{\gamma_d}{G_s \gamma_w} \tag{3-3}$$

where G_s = specific gravity of the solids, and γ_w = unit weight of water.

The voids ratio (e) is determined from

$$e = \frac{n}{1-n} \tag{3-4}$$

where n = porosity. The values for 21 samples and their average values are recorded in Table (3-4).

Grain-Size Distribution

For grain sizes larger than those that can pass through a #200 sieve, grain-size analysis is done mechanically using a standard set of sieves. This test was performed in accordance with ASTM standards D 421 (Sample Preparation), D 422 (Test Procedures), AASHTO T 87 (Sample Preparation), T 88 (Test Procedures), and US Army Corps of Engineers EM 1110-2-1906, Appendix V: Grain-Size Analysis.

Grain size analysis was performed on samples taken at elevations of approximately 229m and 224m. An unnamed green sand layer is at an elevation of ~228m (Figure 3-1). The St. Peter sandstone above the green sand layer is heavily stained with iron oxides and has a predominant grain-size fraction of 0.425mm (0.0167in.) (Figure 3-2). Below the green sand layer, oxidizing fluids rapidly diminish with depth, and as a result of this, oxide staining diminishes as well. Iron oxide nodules are prominent, some are large, and the iron nodules also diminish in size and frequency rapidly with depth. Along with this loss of oxidizing fluids comes a significant change

Table 3-4: Calculated average values for dry unit weight, porosity, and voids ratio. DSD-direct shear dry, DSS-direct shear saturated, and UX- uniaxial.

Sample	M_s (kg)	W_s (kN)	V (m^3)	γ_d (kN/m^3)	n (%)	e
DSD-1	0.6180	0.0061	0.0003	17.88	30.68	0.443
DSD-2	0.6371	0.0062	0.0003	18.55	28.12	0.391
DSD-3	0.6139	0.0060	0.0003	18.31	29.05	0.409
DSD-4	0.6396	0.0063	0.0003	19.01	26.30	0.357
DSD-5	0.6544	0.0064	0.0003	18.77	27.25	0.374
DSD-6	0.6081	0.0060	0.0003	18.58	27.97	0.388
DSS-1	0.6665	0.0065	0.0003	18.95	26.54	0.361
DSS-2	0.6196	0.0061	0.0003	18.99	26.38	0.358
DSS-3	0.6776	0.0066	0.0004	18.94	26.60	0.362
DSS-4	0.6298	0.0062	0.0003	19.01	26.32	0.357
DSS-5	0.6318	0.0062	0.0003	18.61	27.86	0.386
DSS-6	0.6834	0.0067	0.0003	19.21	25.55	0.343
UX_1-1	0.3131	0.0031	0.0002	19.44	24.65	0.327
UX_1-2	0.3181	0.0031	0.0002	19.26	25.34	0.339
UX_1-3	0.3204	0.0031	0.0002	20.02	22.40	0.289
UX_2-1	0.5572	0.0055	0.0003	19.95	22.68	0.293
UX_2-2	0.5414	0.0053	0.0003	20.04	22.32	0.287
UX_2-3	0.5529	0.0054	0.0003	19.94	22.71	0.294
UX_3-1	2.3517	0.0231	0.0012	19.13	25.86	0.349
UX_3-2	2.3982	0.0235	0.0013	18.58	27.97	0.388
UX_3-3	2.4499	0.0240	0.0012	19.43	24.70	0.328
		average values =		**19.08 (121.4 pcf)**	**26.06**	**0.354**

in color. The St. Peter sandstone below this "green sand" layer takes on the characteristic white color that is described in the literature, and along with this change in color comes a substantial change in grain-size distribution (Figure 3-3).

From graphically determined particle sizes D_{10}, D_{30}, and D_{60} the effective grain size (D_{10}), coefficient of uniformity (C_u), and the coefficient of gradation (C_c) can be calculated

using the following expressions:

$$C_u = \frac{D_{60}}{D_{10}} \qquad (3-5)$$

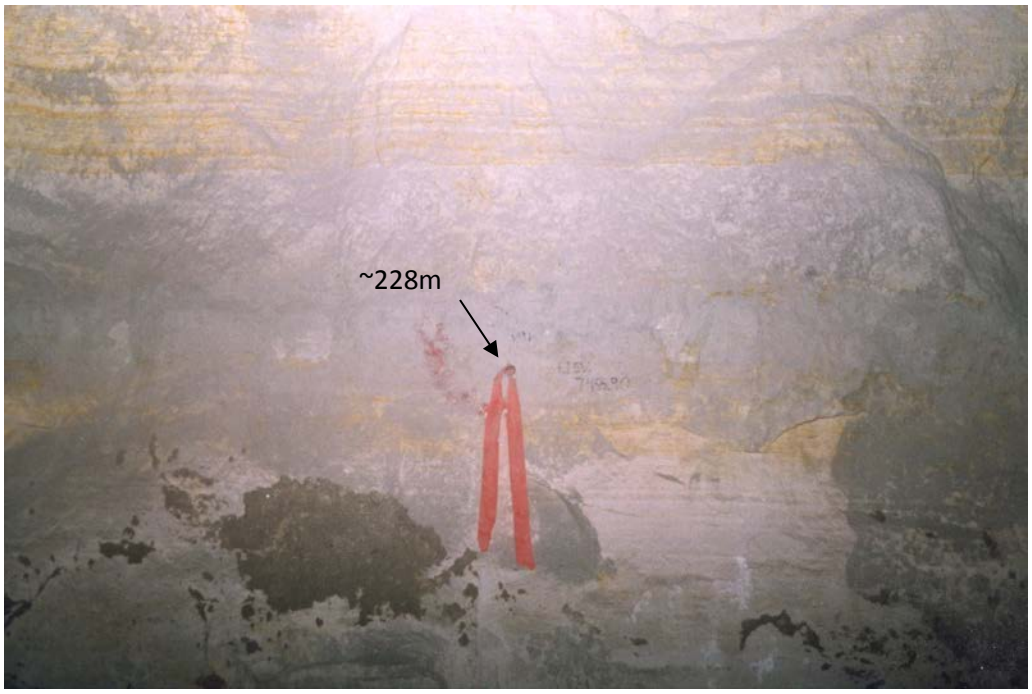

Figure 3-1: Elevation benchmark in the Minnesota Library Access Center excavation in the St. Peter sandstone. The benchmark is located just below an unnamed green sand layer.

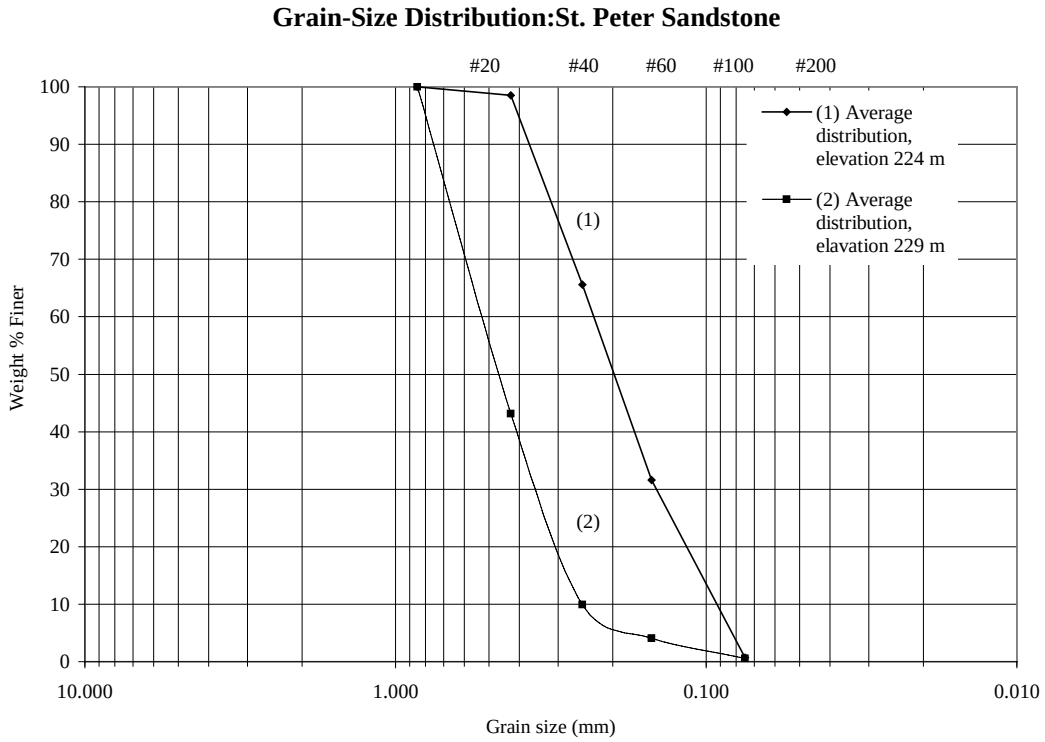

Figure 3-2: Average grain-size distributions of St. Peter sandstone.

where D_{60} = grain-size at 60% finer by weight, and D_{10} = grain-size at 10% finer by weight and

$$C_c = \frac{D_{30}^2}{D_{60} D_{10}} \tag{3-6}$$

where D_{30} = grain-size at 30% finer by weight. Using these expressions, the following values for effective grain size, coefficient of uniformity (C_u), and the coefficient of gradation (C_c) are calculated and shown in Table (3-5).

Table 3-5: Grain-size parameters for St. Peter sandstone.

Sample Elevation (m)	D_{10} **(mm)**	D_{30} **(mm)**	D_{60} **(mm)**	C_u	C_c
~229	0.214	0.331	0.515	2.407	0.994
~224	0.095	0.136	0.208	2.189	0.936

Using the grain-size parameters listed in Table 3-5 and the average values of grain size distribution determined from grain size analysis (Table 3-6), the following expressions can be used to classify the St. Peter sandstone according to the Unified Soil Classification System (*USCS*)

$$R_{200} = 100 - F_{200} \tag{3-7}$$

where R_{200} = percentage of soil retained on a #200 sieve, and F_{200} = fraction of soil passing through a #200 sieve, and

$$R_4 = 100 - F_4 \tag{3-8}$$

where R_4 = percentage of soil retained on a #4 sieve, and F_4 = fraction of soil passing a #4 sieve (Table 3-7). In addition, sands can be further qualified by describing the sand

grains as coarse, medium, or fine grained based on grain size in millimeters (Table 3-8).

Using the values from Table 3-6, Table 3-7 and Table 3-8, the St. Peter sandstone sampled from an approximate elevation of 229 m can be classified as a poorly graded, angular to well rounded, medium to fine grained lightly rust-colored sand with little fines.

Table 3-6: Average grain-size distribution values for St. Peter sandstone.

Sieve Size	Slot Size (mm)	Average ~224m $W\%_{total}$	Average ~229m $W\%_{total}$
20	0.850	0.00	0.00
40	0.425	1.50	56.87
60	0.250	32.93	33.23
100	0.150	33.95	5.82
200	0.075	30.91	3.49
Catch Pan	N/A	0.75	0.56

Table 3-7: Values for R_4, F_4, R_{200} and F_{200} for St. Peter sandstone.

Elevation (m)	R_4 (%)	F_4 (%)	R_{200} (%)	F_{200} (%)
~229	0.00	100.00	99.40	0.60
~224	0.00	100.00	99.28	0.72

Table 3-8: Sizes used to describe sand grains as coarse, medium or fine (Means and Parcher, 1963).

Description	**size (mm)**	**sieve size**
Coarse	2.0 - 0.6	8 - 28
Medium	0.6 - 0.2	28 - 65
Fine	0.2 - 0.06	65 - 200

For St. Peter sandstone samples taken from the lower entrance, and at an approximate elevation of 224m, the grain size distribution shifts significantly toward smaller grain sizes and is much more evenly distributed from the #60 to #200 sieve sizes.

Grains retained by the #40 sieve are almost nonexistent and grains passing through the #200 sieve are similar in weight percent to the sandstone samples taken from 229m (Table 3-6).

Application of USCS parameters and using the values given in Table 3-6, Table 3-7 and Table 3-8, the St Peter sandstone sampled from an elevation of 224m, is poorly graded, angular to well rounded, medium to fine-grained white-colored sands with little fines, and infrequent occurrences of iron nodules that are 0.43mm to 0.25mm in size.

Shear Strength

Coulomb described the shear strength (τ_f) of a geo-material at a point on a particular plane as a linear function of the normal stress (σ_f) on the plane at the same point (Craig, 1996). This results in the expression

$$\tau_f = c + \sigma_f \tan\phi \qquad (3-9)$$

where c = apparent cohesion, and ϕ = The angle of internal friction.

Terzaghi later recognized that shear stress could only be developed in the skeleton of a geo-material, resulting in an expression for shear stress as a function of the effective normal stress:

$$\tau_f = c' + \sigma'_f \tan\phi' \qquad (3-10)$$

with the shear strength parameters c' and ϕ' described in terms of effective stresses.

A geo-material's shear strength can also be described in terms of σ_1' and σ_3', at failure, which are the major and minor principal stresses respectively (Figure 3-3). The failure envelope may be taken as a straight line at failure, which is represented by

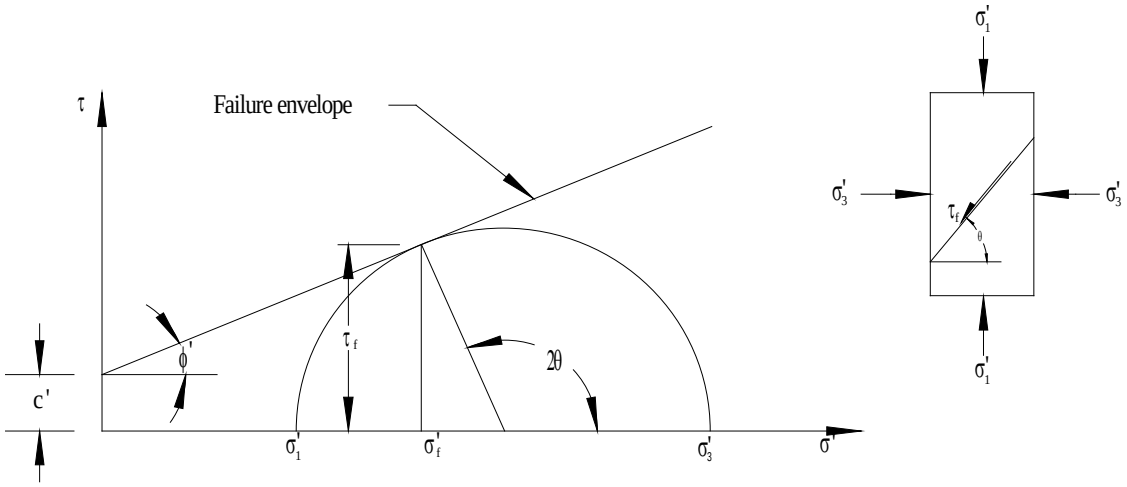

Figure 3-3: Stress conditions represented by the Mohr-Coulomb failure envelope.

expression (3-10), and is tangent to Mohr's circle shown in Figure 3-3. The coordinates of the tangent point are τ_f and σ_f' and

$$\tau_f = \frac{1}{2}\left(\sigma_1' - \sigma_3'\right)\sin 2\theta \tag{3-11}$$

$$\sigma_f' = \frac{1}{2}\left(\sigma_1' + \sigma_3'\right) + \frac{1}{2}\left(\sigma_1' - \sigma_3'\right)\cos 2\theta \tag{3-12}$$

where θ is the theoretical angle between the major principal plane and the plane of failure (Craig, 1996). It is evident that

$$\theta = 45^o + \frac{\phi'}{2} \tag{3-13}$$

and from Figure 3-3 the relationship between τ_f and σ_f' and σ_1' and σ_3' can be obtained:

$$\sin\phi' = \frac{\frac{1}{2}\left(\sigma_1' - \sigma_3'\right)}{c'\cot\phi' + \frac{1}{2}\left(\sigma_1' + \sigma_3'\right)} \tag{3-14}$$

Rearrangement of (3-14) leads to

$$\left(\sigma_1' - \sigma_3'\right) = \left(\sigma_1' + \sigma_3'\right)\sin\phi' + 2c'\cos\phi' \tag{3-14a}$$

and results in

$$\sigma_1^{'} = \sigma_3^{'} \tan^2\left(45^o + \frac{\phi'}{2}\right) + 2c' \tan\left(45^o + \frac{\phi'}{2}\right) \qquad (3\text{-}14b)$$

Expression (3-14b) is the Mohr-Coulomb failure criterion. Knowing multiple stress states, a common tangent can be drawn touching all of the Mohr's circles. This common tangent is the failure envelope.

Direct Shear

The direct shear test is used to determine the Mohr-Coulomb failure envelope of a geo-material by confining the material in a box (square or circular) that is split mid height so the two halves are allowed to move relative to each other. Typically one half of the shear box is pinned to a load cell or proving ring and the shear force is measured either directly or by calculating shear force from measured displacements in the proving ring. Normal force (*N*)is applied to the soil from the top through a metal plate, and shear force (*T*)is generated by shearing the box at a constant rate of strain (Figure 3-4).

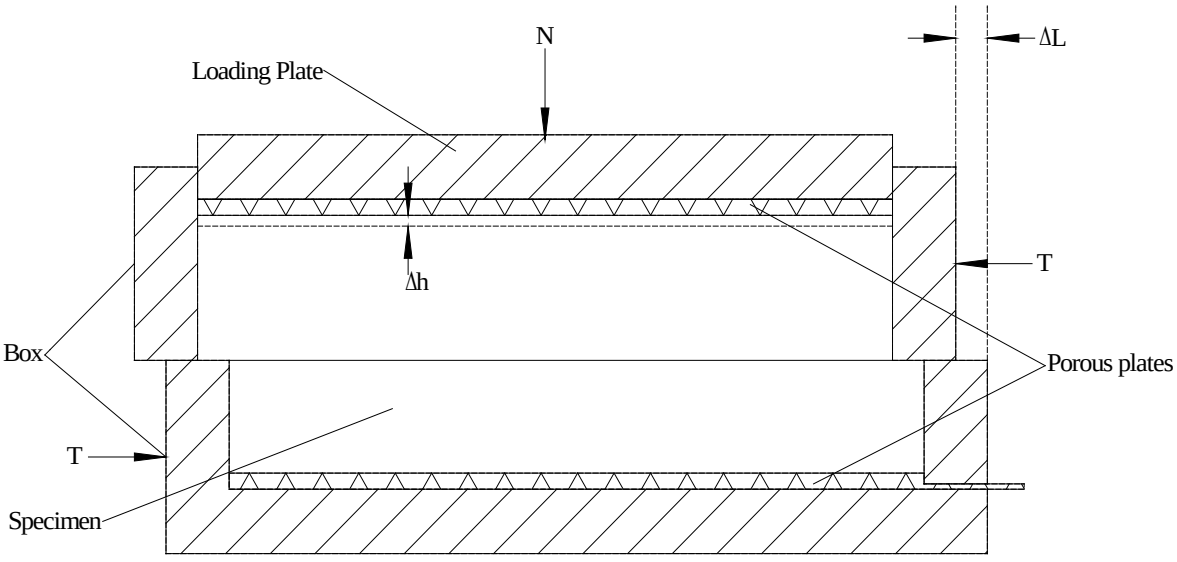

Figure 3-4: Cross-sectional diagram of a direct shear box.

The normal stress (σ') is calculated by dividing the normal load by the cross-sectional area of the top plate. The shear stress is calculated by dividing the shear force by the current cross-sectional area, the cross-section of soil under shear is changing with constant rate, so the shear stress (τ) for a rectangular specimen needs to be calculated with the following expression:

$$\tau = \frac{T}{A_0 - \Delta L\sqrt{A_0}} \qquad (3\text{-}15)$$

where A_0 is the initial area and ΔL is the change in length.

The advantages of the direct shear test are that it is an easy and quick test to run, and for cohesionless geo-materials (sand), it is an easy test to prepare. The disadvantages are there is no way to control drainage conditions and pore water pressure cannot be determined; so under undrained conditions, the effective normal stress is not known. In addition, only the average shear stress can be determined because shear stress is not uniform throughout the failure plane, with failure occurring progressively from the edges to the center of the sample (Craig, 1996).

For shear testing, the samples were oven dried for 24 hours at 105°C prior to preparation. The intact samples were trimmed with a hacksaw and a steel square to within (0.5mm x 1.0 mm) of the dimensions of the shear box, and then pressed into the shear box. The extremely friable nature of the St. Peter is a blessing and a curse. As has been described, the sandstone is easily shaped for testing; the drawback is that considerable care needs to be taken or the samples will break rendering them useless. The edges of the box performed the final act of trimming resulting in a sample that matched the inside dimensions of the shear box. The height from the top of the sample to

the top of the shear box was measured in each corner and an average value was taken assuming that the surface of the sample was planar.

Knowing the area and height of the sample the volume was calculated, and the dry unit weights for the samples were determined (Table 3-9).

Table 3-9: Average unit weights of intact and pulverized St. Peter sandstone samples that have undergone direct shear testing.

	σ (kPa)	Dry, Intact γ_d (kN/m$_3$)	Saturated, Intact γ_d (kN/m^3)	Dry, Loose γ_d (kN/m^3)	Dry, Dense γ_d (kN/m^3)	Saturated, Dense γ_d (kN/m^3)
	5	17.89	18.97			
	19	18.53	18.98	17.15	18.89	19.83
	38	18.31	18.94	17.26	19.01	19.94
	76	19.01	19.03	17.42	19.22	19.50
	152	18.79	18.64	17.36	19.25	19.28
	304	18.61	19.20	17.33	18.95	19.58
$\gamma_{sample\ (avg)}$ (kN/m^3) =		**18.65**	**18.96**	**17.30**	**19.06**	**19.63**
$\gamma_{sample\ (avg)}$ (pcf) =		**118.72**	**120.69**	**110.15**	**121.36**	**124.94**

For the unconsolidated samples, the loosely packed samples were poured into the shear box through a funnel, and then smoothed approximately parallel and within 5mm to 10mm of the top of the shear box. The densely packed samples were poured into the shear box in 5 lifts and each lift was vibrated with 10 taps from an 8-ounce ballpeen hammer on each side of the shear box. The samples were then smoothed until they were approximately parallel and within 5mm to 10mm of the top of the shear box. The procedure for determining dry unit weight is the same as for the intact samples.

The direct shear tests, for both intact and pulverized St. Peter sandstone samples, were performed with a GEOTEST model S2215A direct shear machine, which conforms to all aspects of ASTM D3080 and U.S. Army Corps of Engineer standards.

Measurements used to establish unit weights of intact, loosely packed, and densely packed St. Peter sandstone were made in a standard square, 101.6mm (4 in.) shear box.

Results

Intact samples that were sheared exhibited very high dilation rates at failure (Figure 3-5), where us is the shear displacement and these dilation rates are much higher than loosely packed or even densely packed sand (Figure 3-6). In addition, examination of Figure 3-5 shows that initially there is almost no contraction at low normal stress (< 38 kPa), indicating the St. Peter sandstone had undergone considerable post-depositional

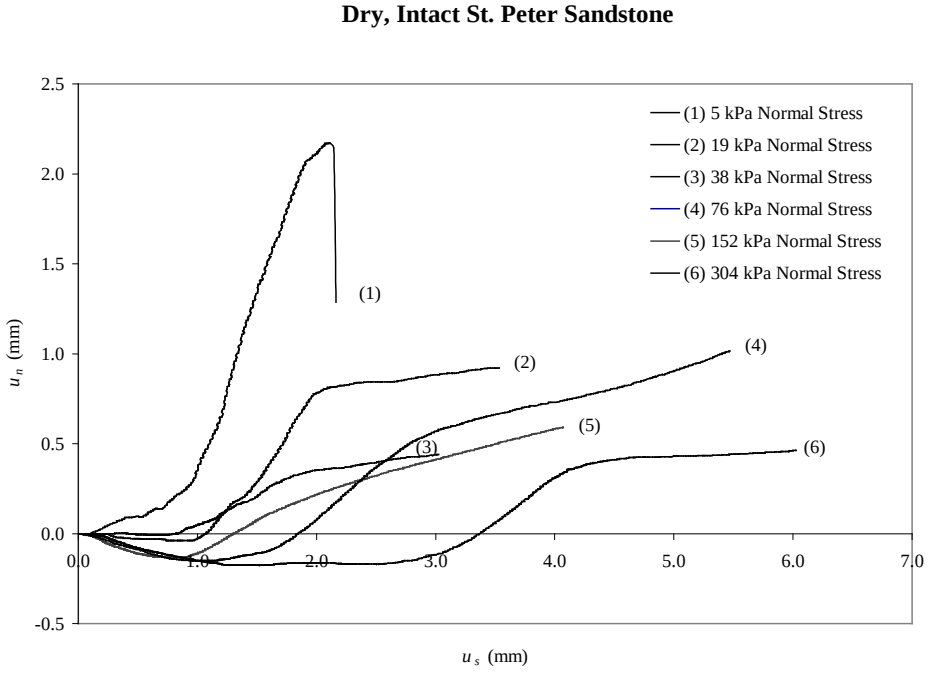

Figure 3-5: u_n vs u_s for intact St. Peter sandstone over a range of normal stresses.

compression. With higher normal stresses, the sandstone started to behave more like the densely-packed sand though the dilation rate at failure remains higher than the densely-packed sand samples tested (Figure 3-7). The very high dilation rates at failure are indicative of high peak frictional strengths (Figure 3-8).

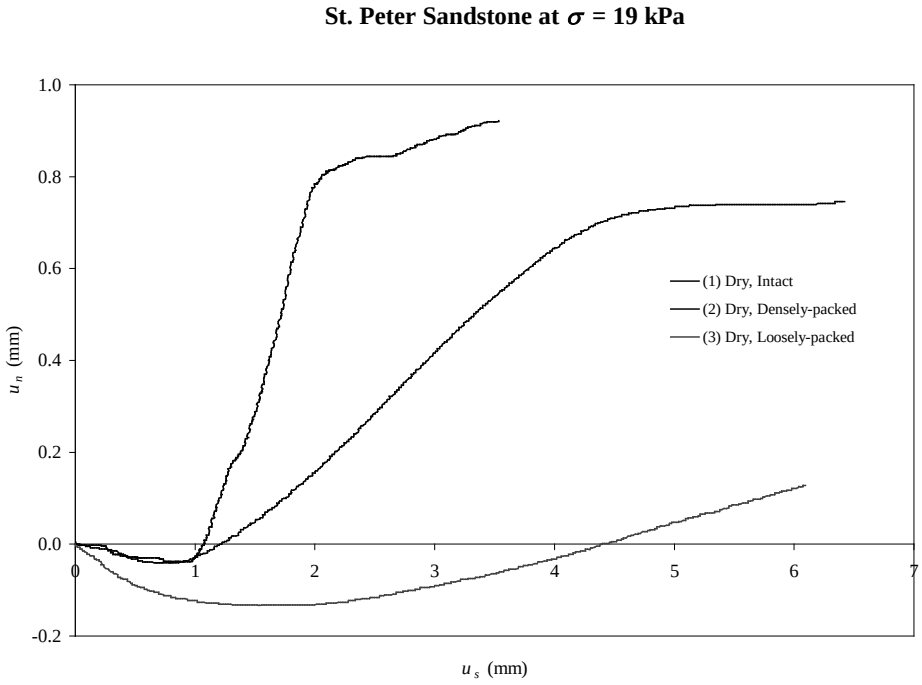

Figure 3-6: Comparison of dilation of intact, St. Peter sandstone, and densely packed and loosely packed St. Peter sand.

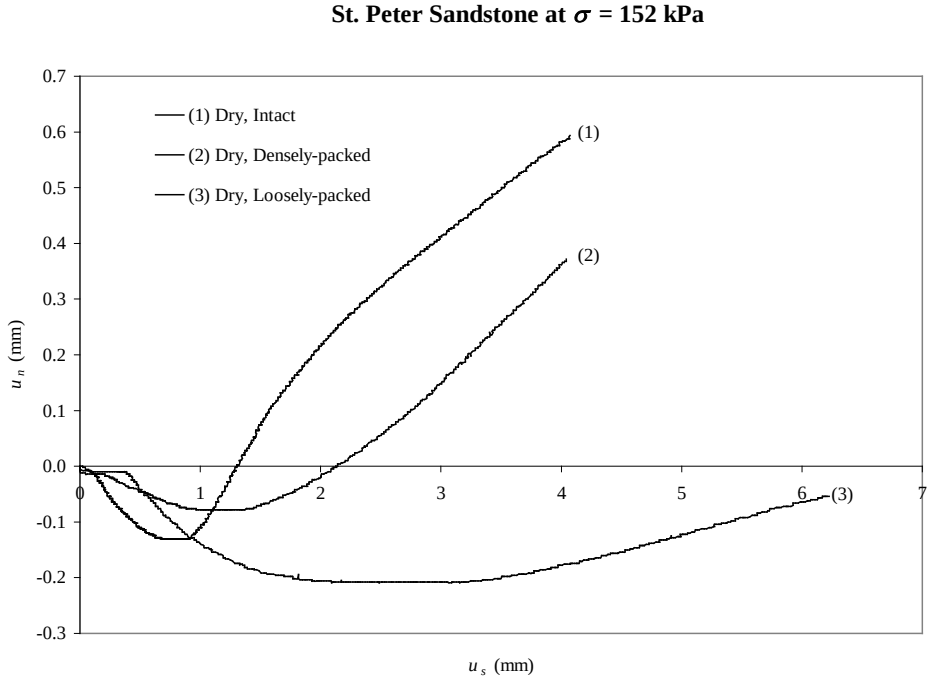

Figure 3-7: Comparison of dilation of intact, St. Peter sandstone, and densely packed and loosely packed St. Peter sand.

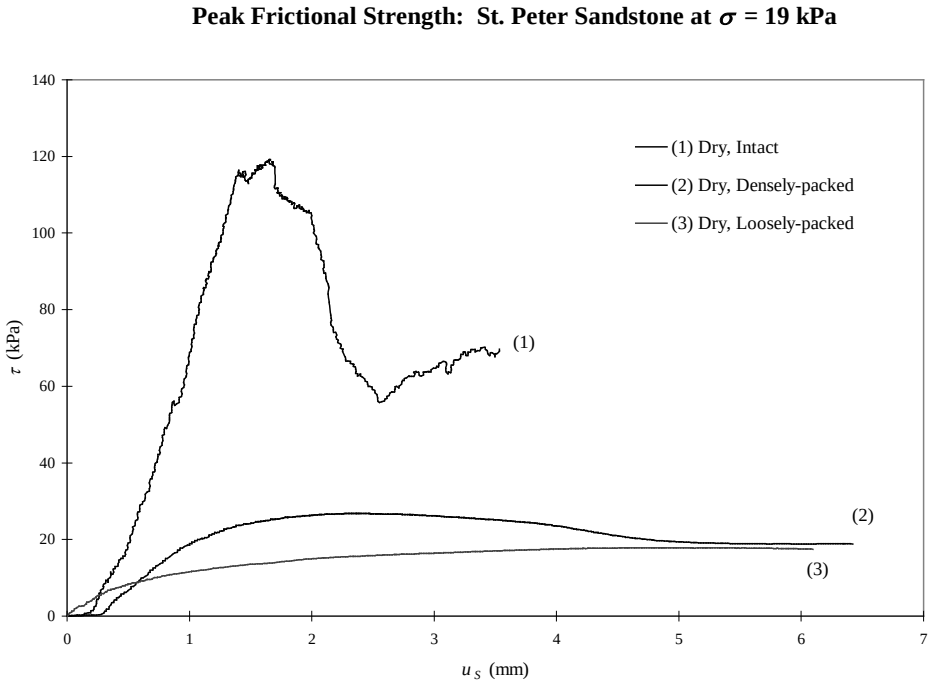

Figure 3-8: Comparison of peak frictional strengths of intact St. Peter sandstone, and densely packed and loosely packed St. Peter sand.

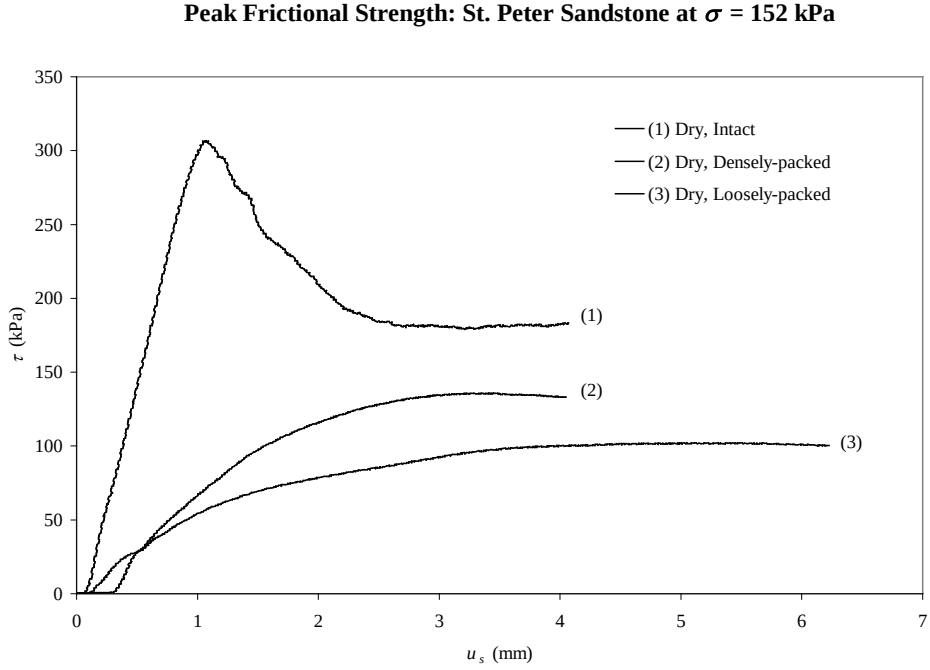

Figure 3-9: Comparison of peak frictional strengths for intact St. Peter sandstone and densely packed and loosely packed St. Peter sand.

With an increase in normal stress, dilation rates at failure changed noticeably. At normal stresses (> 38 kPa), as shown in Figure 3-7, dilation rates of intact samples became more similar to dilation rates of densely packed sand. Examining Figure 3-10, it is evident that there is also a substantial change in the slope of the Mohr-Coulomb failure envelope. This change in the failure envelope is attributed to the increasing normal stress subduing the dilation. Dusseault and Morgenstern (1979) assign a highly curved failure envelope to intact, directly sheared samples. Looking closely at the failure envelope indicates another option. This option is that the St. Peter sandstone behaves in a bilinear fashion (Figure 3-11) that is largely a result of the locked sands that make up the St. Peter sandstone, and is also, to a smaller extent, due to post-depositional overgrowths. At lower normal stresses (< 38 kPa), the strength of the locked sands and overgrowths are greater than the shear stress, resulting in considerable topographic relief in the shear band (Figure 3-12). The high dilation rates at failure are then a function of the geometry of the sheared surfaces. As normal stress increases (> 38 kPa), shear stresses become greater than the strength of the locked sands and overgrowths. Topographic relief is reduced (Figure 3-13) and the dilation rates at failure are subdued, and shear strength becomes a function of sliding friction rather than geometry (Table 3-10). More evidence of the change from geometric effects to sliding effects is found by looking at the plot of the residual strength envelope (Figure 3-14). By plotting a linear envelope to the data, the internal friction angle is similar to the densely packed sand but the data points are even more nonlinear than the intact samples. This more clearly demonstrates that at low normal stresses, the shear surface asperities, which were as high as 1.5 mm, contribute greatly to the shear strength of the sandstone while at higher normal stresses, the

asperities themselves are sheared off and sliding friction becomes the dominant source of shear strength in the sandstone.

Table 3-10: Comparison of dilation angles with corresponding friction angles in intact St. Peter sandstone and densely and loosely packed St. Peter sand.

	Dry Intact		Dry Dense		Dry Loose		Saturated Intact		Saturated Dense	
Normal Stress (kPa)	ϕ (deg)	δ (deg)	ϕ (deg)	δ (deg)	ϕ (deg)	δ (deg)	ϕ (deg)	δ (deg)	ϕ (deg)	δ (deg)
5	73	63	N/A	N/A	N/A	N/A	55	11	N/A	N/A
19	68	47	50	14	41	4	52	8	41	6
38	70	20	46	22	37	4	52	14	39	7
76	43	28	44	16	35	3	32	8	36	6
152	48	21	41	12	34	3	33	8	35	5
304	46	26	36	7	34	2	32	8	30	2

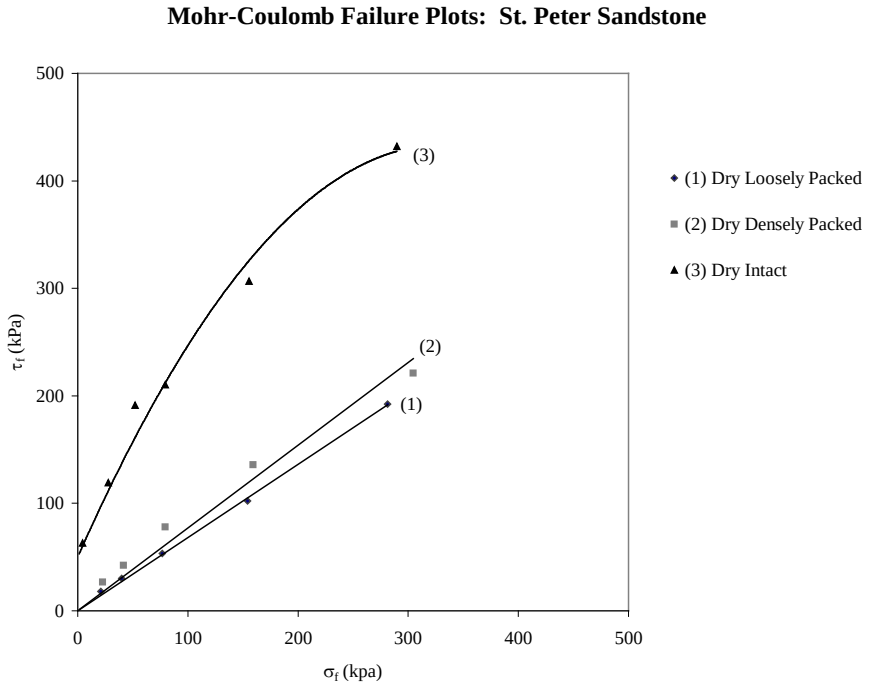

Figure 3-10: Comparison of peak strength failure envelopes of dry, intact St. Peter sandstone, and dry, densely packed and loosely packed St. Peter sand.

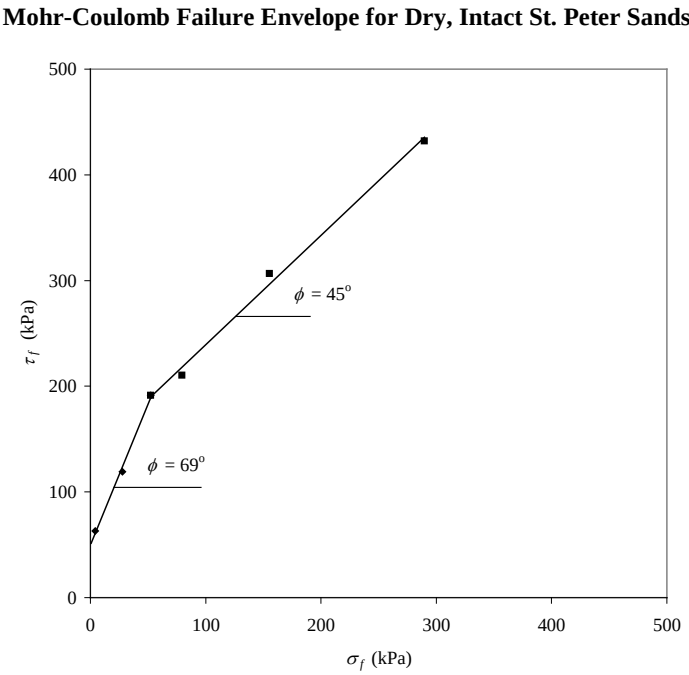

Figure 3-11: Failure envelope of St. Peter sandstone showing noticeable bilinear behavior.

Figure 3-12: St. Peter sandstone sheared at 19 kPa normal stress showing considerable topographic relief in the shear zone.

Figure 3-13: St. Peter sandstone sheared at 152 kPa normal stress. The photo shows diminished topographic relief.

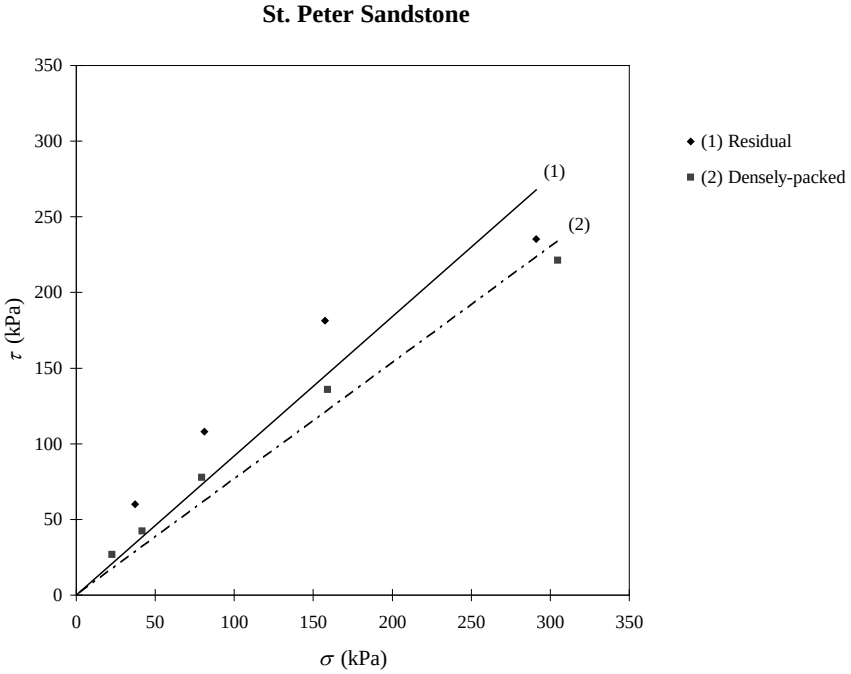

Figure 3-14: Mohr-Coulomb failure envelopes of densely packed St. Peter sand, and residual failure envelope of sheared intact St. Peter sandstone.

The high angle of friction at failure are attributed to the St. Peter sandstone being a locked sand (Dusseault and Morgenstern, 1979) and to post-depositional quartz overgrowths forming an interlocking "finger effect" (Pittman, 1972; Mazzullo and Ehrlich, 1983). If this is indeed the case, then there should not be any appreciable decrease in frictional strength, internal friction angle or dilation rates at failure when the St. Peter sandstone is sheared under saturated conditions. For cohesionless sands, wet sands will often show a decrease in the angle of internal friction by 1 to 2 degrees over dry sands (Al-Khafaji and Andersland, 1992). Examination of St. Peter sandstone under dry and saturated conditions shows something significantly different (Figure 3-15). Most obvious, when looking at Figure 3-15, are the lack of cohesion and the substantial loss of shear strength. This noticeable difference in failure envelopes is apparent in dry and saturated densely packed St. Peter sand as well (Figure 3-16). An examination of the ratios of τ_f, under dry and saturated conditions shows a loss of cohesion and a noticeable drop in frictional strength (Table 3-10). What is also evident is a bilinear behavior similar to dry intact samples (Figure 3-17). At higher values of normal stress, the failure envelopes of the saturated intact samples are very similar to saturated, densely-packed sand (Figure 3-18).

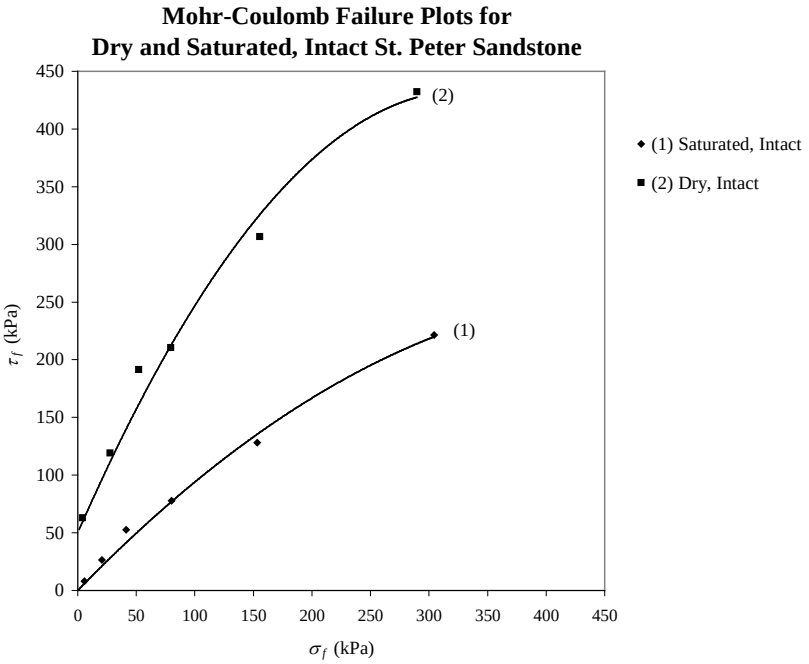

Figure 3-15: Comparison of Mohr-Coulomb failure envelopes of dry intact and saturated intact St. Peter sandstone.

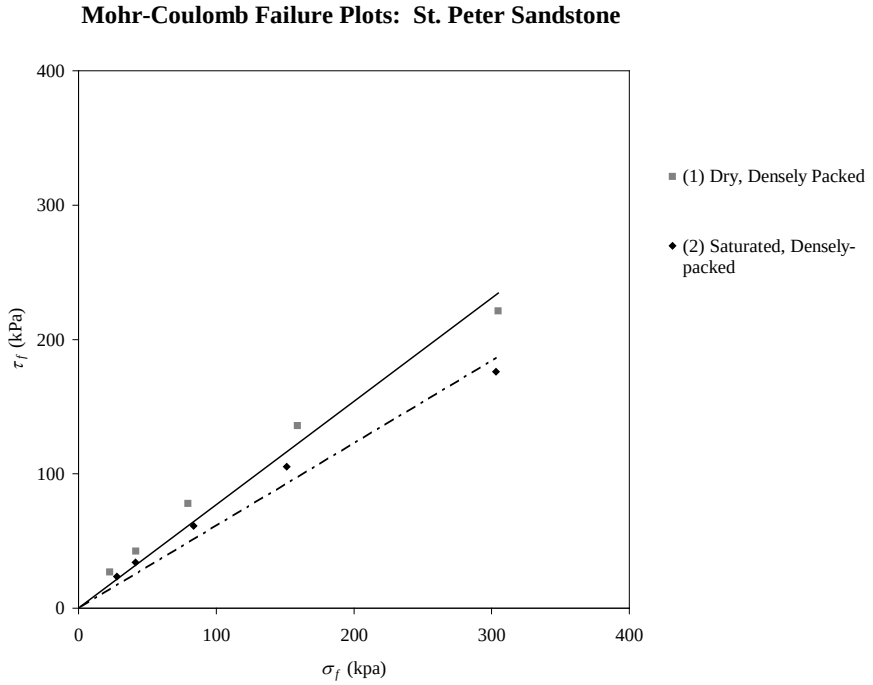

Figure 3-16: Comparison of Mohr-Coulomb failure envelopes of dry densely packed and saturated densely packed St. Peter sand.

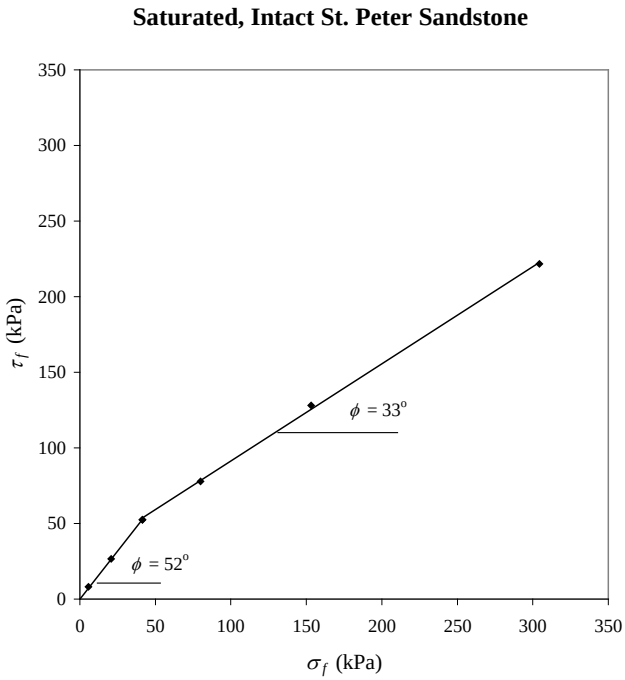

Figure 3-17: Mohr-Coulomb failure envelope in saturated, intact St. Peter sandstone showing bilinear behavior.

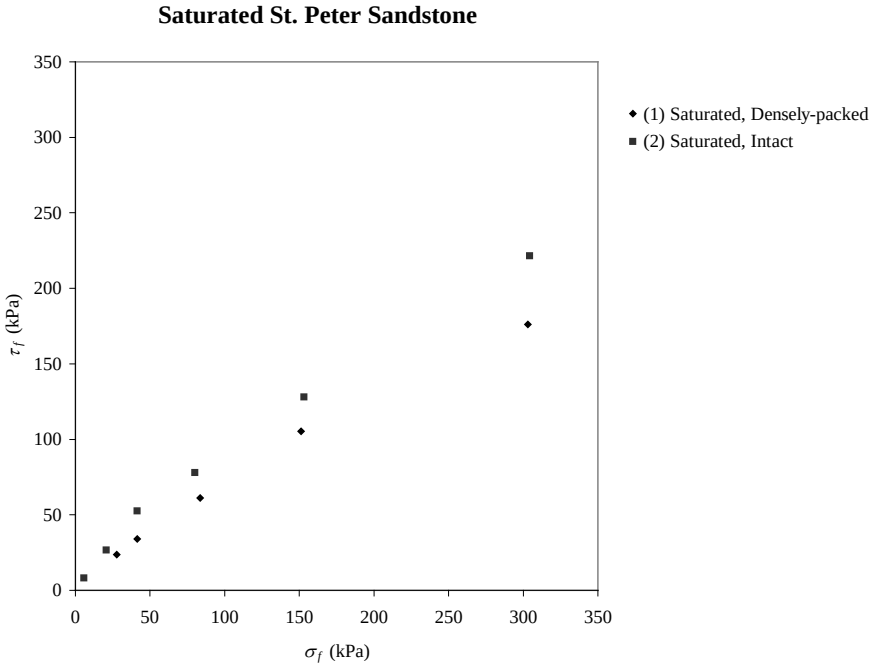

Figure 3-18: Comparison of saturated shear strengths of intact St. Peter sandstone and densely packed St. Peter sand.

Triaxial Compression

The triaxial compression test is the most versatile shear strength test and can be used on all types of soils. This versatility comes from the ability to control drainage conditions for low permeability soils, and as a result, pore water pressures can be measured.

The triaxial test is a 3-dimensional test where confinement is applied uniformly to the axial surface of a cylindrical sample, and the confining stress is symmetrically applied to the surface. This results in the intermediate stress (σ_2') equaling the minor principal stress (σ_3'). The stress applied axially is the major principal stress (σ_1') and is called the deviator stress. With $\sigma_2' = \sigma_3'$, a triaxial test can be represented by a Mohr diagram (Figure 3-4). Running multiple tests at different values of σ_1' and σ_3', and assuming a straight line failure envelope, the angle of internal friction can be graphically determined from the Mohr diagram and the cohesion (c') of the material can be determined from expression (3-14).

Previous triaxial testing has been limited to Watson (1938) at Harvard University and Labuz, Zietlow, and Chen (1996) at the University of Minnesota. In Watson's study, testing was carried out on intact, densely-packed and loosely-packed samples taken from near St. Anthony falls in a desire to determine stress-deformation characteristics of the St. Peter sandstone which was used as a foundation material for the construction of a new navigation lock. Testing was conducted on intact samples by Labuz, et al., to help confirm stress-deformation characteristics for the construction of the Minnesota Library Access Center, an underground library archives on the west bank of the University of Minnesota.

Watson's test results showed that the internal angle of friction varied considerably between intact and disturbed St. Peter sandstone samples. The intact specimens were trimmed into cylinders that were, on average, 6.99cm (2.75in.) in diameter and 16.51cm (6.5in.) in length. These samples were sealed in a rubber liner and evacuated for five minutes and then saturated under a low hydraulic head. Confining pressure was applied to the sample, the vacuum was released and the samples were deformed progressively until failure. In each test, one or more rebound loops were made.

The Mohr failure envelope shows two curves. One is a straight line and the other is a curve. Watson (1938) reports that the failure envelope more closely represents a curved line with an average slope of 60° (Figure 3-19). Triaxial tests on densely packed and loosely packed samples were performed in the same manner as the intact samples, and yielded the following failure envelopes (Figure 3-20).

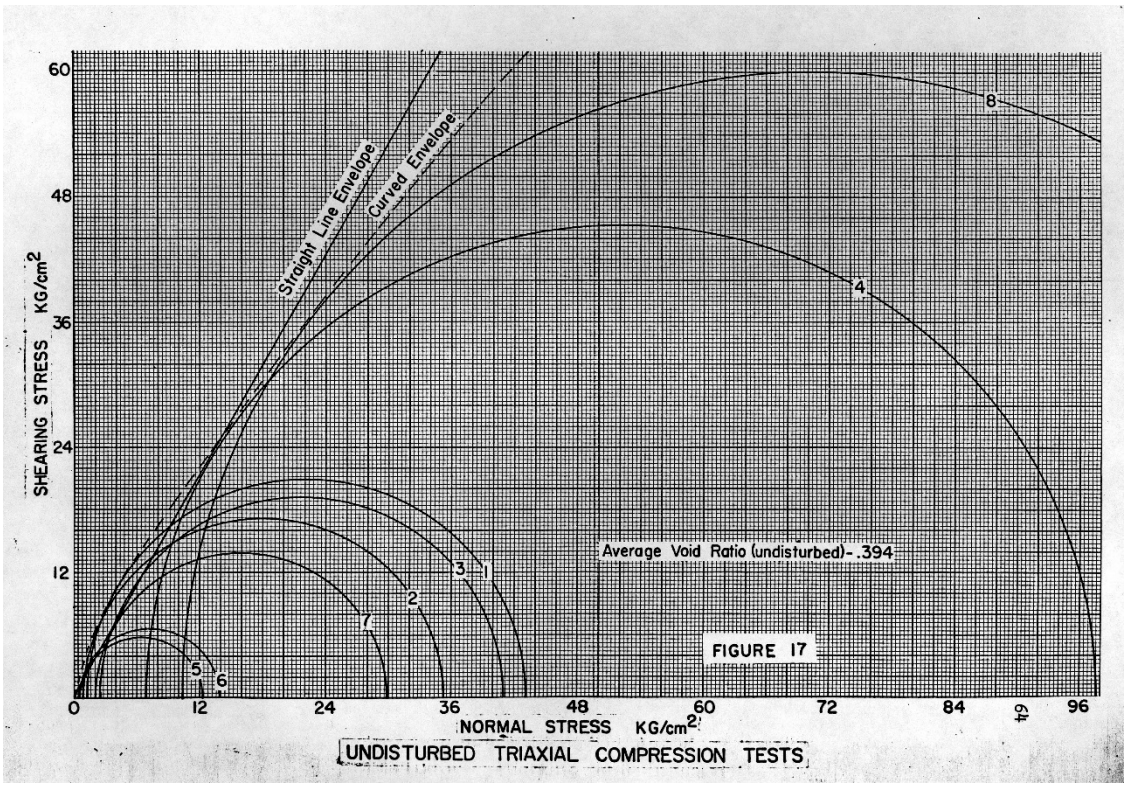

Figure 3-19: Failure envelope from triaxial testing of saturated St. Peter sandstone (Watson, 1938).

Tests performed at the University of Minnesota were done on intact samples only and these samples were tested dry. The sandstone samples were cored with a drill press mounted core bit. This bit has slightly turned in teeth to prevent the cuttings from binding up the bit and damaging or breaking the core. The ends of the core were squared up with the core barrel and leveled to within 0.2mm on the ends. These samples were wrapped in a one millimeter thick Viton rubber sheath and sealed with polyurethane. Test results showed a similar internal friction angle to Watson's study, and the failure envelope was straight rather than curved (Figure 3-21). It was thought that at higher confining stresses the failure envelope would start to curve. The lack of a curved envelope at lower confining stresses is probably due to the samples being tested dry rather than saturated.

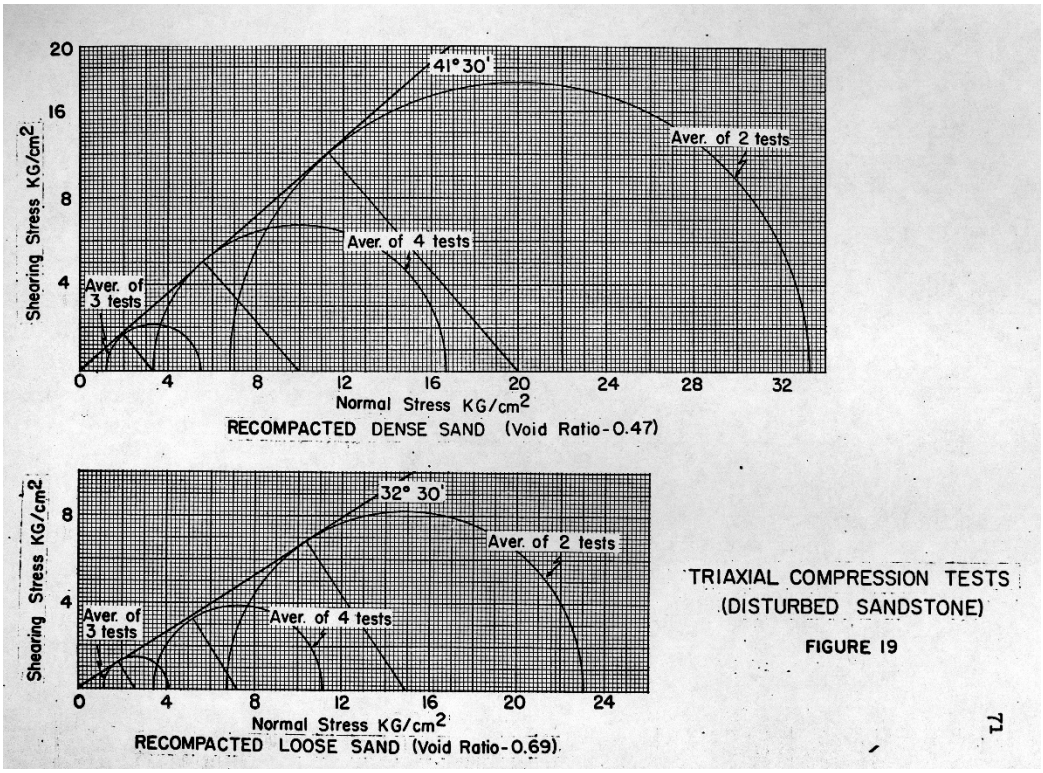

Figure 3-20: Internal friction angles from triaxial testing on saturated loosely packed and densely packed St. Peter sand.

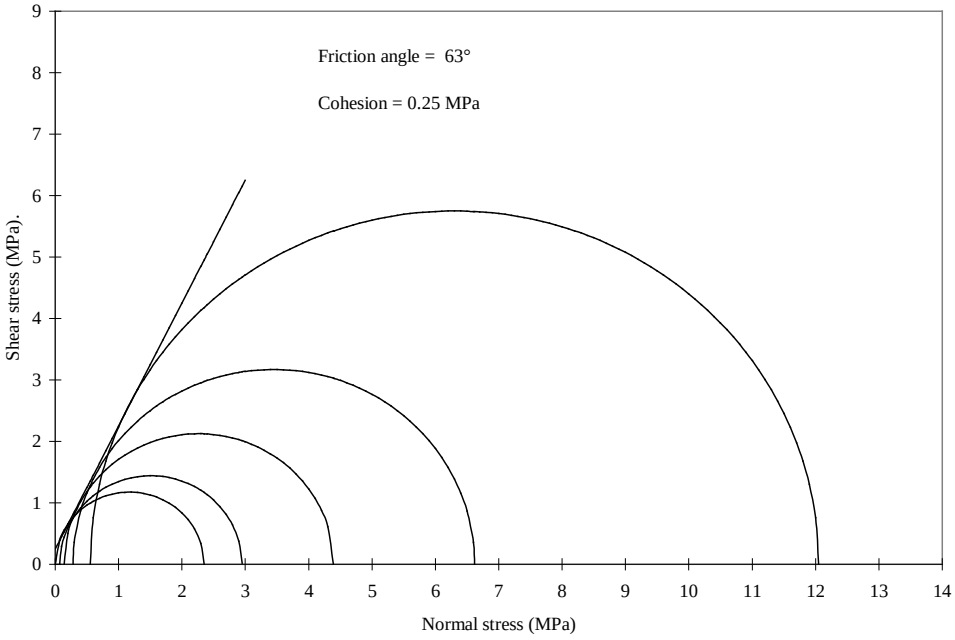

Figure 3-21: Internal friction angle of dry intact St. Peter sandstone determined from triaxial testing (Labuz, et al., 1996).

Uniaxial Compression

Uniaxial compression is a specific example of triaxial testing where testing is done with no confining stress, so $\sigma_2' = \sigma_3' = 0$. This results in expression 3-14b simplifying to:

$$\sigma_1^{'} = 2c'\tan\left(45^o + \frac{\phi'}{2}\right) \qquad (3\text{-}16)$$

This expression also shows that the geo-material must be cohesive to be tested uniaxially.

Prior to interest being taken in the development of underground spaces, the only interest in St. Peter sandstone was in conjunction with tunneling and foundation analysis. Uniaxial compression testing was not of any real value in these studies. As a result, few attempts were made to determine the unconfined compressive strength of the St. Peter sandstone, and these efforts were plagued with difficulties in obtaining suitable samples for shaping and testing (Peterson, 1978).

The overriding concern when sampling and shaping the St. Peter sandstone for testing is the rock itself. The St. Peter sandstone is extremely friable and most power sampling and shaping tools destroy the samples long before they are ready for testing. This means that sampling is usually taken from intact blocks that have detached from outcrops or have been cut out by tools such as electric chainsaws. Shaping the samples generally must be done by hand. This makes the process time consuming and tedious.

The earliest reported efforts to determine a value of unconfined compressive strength comes from Schwartz (1939). A block of St. Peter sandstone was taken from the Ford Motor Company tunnel and was air dried for three weeks prior to preparation. Three blocks that were 5cm (2in.) on a side were fashioned from the sample and tested in the following fashion.

Block (a) was placed in a beaker on a rubber stopper and the beaker was filled with water until approximately 1mm of the sandstone block was submerged. The sample was covered with a damp towel for several hours and subsequently tested. The block failed at a stress of 3.96kPa (0.574psi).

Block (b) was placed in a beaker in the same fashion as block (a) and water was poured into the beaker to just cover the bottom of the beaker and not touch the sandstone in any way. The sample was covered with a damp towel for several hours and subsequently tested. The block failed at a stress of 7.31kPa (1.06psi).

Block (c) was tested dry and failed at a stress of 993kPa (144psi).

In 1951, the U.S. Army Corps of Engineers conducted uniaxial tests on the St. Peter sandstone (Table 3-11). There was no indication of the length to diameter ratio of the samples or if the ends were capped. The tests were conducted on samples taken down section from an elevation of 652 ft. to 597 ft. This places the sampling below an unnamed silt layer in the Tonti member rather than the Starved Rock member. Above this silt layer, the St. Peter sandstone is soft and friable, and it was not possible to retrieve viable cores. Below the silt layer, the sandstone is composed of alternating layers of siltstone and sandstone that could be cored, and some of the layers were highly cemented.

Later testing was conducted by the University of Minnesota on samples taken from outcrops in the Mississippi River valley (Table 3-12). Subsequent efforts by Sterling (1978) were performed while the underground test room was being excavated at the University of Minnesota's Civil Engineering building. These samples were tested with a hydraulic jack assembly that was braced against the ceiling of the room (Table 3-13) (Peterson, 1978).

Table 3-11: Uniaxial test results (U.S. Army Corps of Engineers, 1951).

Sample No.	Elevation (feet)	Moisture content (%)	γ_d (pcf)	σ_1 (psi)	Modulus of Deformation		Poisson's ratio
					Axial (psi)	Lateral (psi)	
7	652.5 - 650.5	14.6	115.2	850	336,000	714,000	0.46
14-3	640.2 - 635.3	10.4	125.1	1370	151,000	2,800,000	0.05
15-2	635.7 - 626.2	13.2	114.6	990	247,000	1,280,000	0.19
16-4	626.3 - 621.1	9.4	122.9	2100	518,000	1,370,000	0.38
18-1	616.5 - 612.1	3.8	113.4	677	173,000	2,220,000	0.08
18-3 Top of core	616.5 - 612.1	5.0	135.0	990	424,000	4,550,000	0.09
18-3 Bottom of core	616.5 - 612.1	5.3	134.0	2370	542,000	4,550,000	0.12
19-3 Top of core	612.1 - 607.7	10.1	123.1	2010	695,000	2,480,000	0.28
19-3 Bottom of core	612.1 - 607.7	10.1	118.7	2820	741,000	2,480,000	0.30
21-3 Top of core	603.1 - 597.4	6.4	127.3	2070	426,000	5,440,000	0.08
21-3 Bottom of core	603.1 - 597.4	3.5	141.1	940	185,000	9,190,000	0.02

Table 3-12: Uniaxial test results recorded by Professor Donald Yardley (Peterson, 1978).

Specimens	**Area (in^2)**	**Total Load (lbs)**	σ_1 **(psi)**	σ_1 **(kPa)**
C - 1	1.00	310	310	2137
C - 2	1.56	440	280	1931
C - 3	3.00	1020	340	2344
C - 4	3.50	1440	410	2827
C - 5	3.50	1540	440	3034
C - 6	3.75	1780	480	3310
C - 7	4.75	2740	570	3930
C - 8	5.00	2800	560	3861
C - 9	4.50	2430	540	3723
C - 10	5.00	2550	510	3516

Table 3-13: Uniaxial test results from Professor Raymond Sterling (Peterson, 1978).

Test	Width (in)	Height (in)	Depth (in)	Area (in^2)	Failure Load (lbs)	Failure Stress (psi)	Failure Stress (kPa)	Young's Modulus (psi)	Young's Modulus (kPa)
1	11.5	11	6	69	45,600	661	4558	N/A	N/A
2	12	7	6	72	71,250	990	6826	N/A	N/A
3	8.5	9	8	68	22,800	335	2310	N/A	N/A
4	8	10	8	64	13,300	208	1434	N/A	N/A
5	8	8	9	72	33,250	462	3185	125,000	861,875
6	9	9.5	9	81	68,400	844	5819	620,000	4,274,900
7	8	6.5	8	64	28,800	450	3103	125,000	861,875
8	7	10	8	56	13,000	232	1600	400,000	2,758,000
9	7.5	7	8	60	28,000	467	3220	N/A	N/A
10	8	4	8	64	55,000	859	5923	350,000	2,413,250

Test results reported by Peterson (1978) show that compressive strength values are highly variable, and in general lower than the samples tested by the Corps of Engineers. This is most likely due to the Corps of Engineers sampling the Tonti member, and later testing by the University of Minnesota was performed on samples from the Starved Rock member.

Peterson (1978) conducted additional uniaxial tests on the St. Peter sandstone. The blocks for shaping were taken from a slide in a cave in St. Paul, MN in 1877. Tests were done on cylinders that were ~30cm in diameter and on cubes that were 4cm to 5cm in length. The aspect ratio for these samples was kept as close to 1:1 as possible. The cylinders were capped with hydrostone to ensure parallel ends. The cubes weren't capped, rather paper was placed between the cubes and the platens on the load frame to reduce friction (Peterson, 1978). Peterson's results are consistent with previous results from the University of Minnesota (Table 3-14).

Table 3-14: Uniaxial test results from Dr. D. L. Peterson (1978).

Nominal Size (cm)	Volume (cm3)	Number of Tests	Average Strength (kPa)	Young's Modulus (kPa)
1.3	2.2	7	1655	N/A
2.5	15.6	5	1758	N/A
3.8	54.9	6	2655	N/A
5	125	4	4344	N/A
5	82	9	4137	896,350
30.5	15,580	2	3689	1,537,585 1,054,935

Uniaxial tests for this project were conducted on cylindrical samples that had average diameters of 9.29cm, 5.59cm, 4.67cm, and one earlier sample was tested with a diameter of 7.45cm. All cores were shaped to maintain an approximate aspect ratio of 2:1 (Figure 3-22).

Figure 3-22: Finished St. Peter sandstone samples for uniaxial testing.

Blocks that were used for testing were cut out of the floor of the Minnesota Library Access Center with an electric chain saw. These blocks were roughly square and approximately 25cm on a side (Figure 3-23). These blocks were cut into fourths. This

Figure 3-23: Rough block of St. Peter sandstone.

was done with a hacksaw blade (Figure 3-24). The next step is to trim the blocks into appropriate sizes to be shaped (Figure 3-25). When the blocks have been trimmed, then they were ready to be shaped. Shaping was done with pieces of schedule-80 PVC that had teeth cut into one end of the pipe. This was done to allow cuttings to fall away from the core and prevent damage (Figure 3-26). Samples were detached from the base of the block with a hacksaw blade, and the ends were squared in a jig (Figure 3-27). This allowed the cores to be parallel to within 0.5mm.

Figure 3-24: Cutting blocks into sizes for shaping.

Figure 3-25: Trimming samples for coring.

Figure 3-26: Coring the sample. This was done by rotating the PVC with slight downward pressure. The teeth cutting into the pipe are clearly visible.

Figure 3-27: Squaring ends of the cores. Cores were squared to within 0.5mm on the ends.

The cores were tested in an MTS model 858 table top load frame. The platens used were rigid, so there was no ability to conform to the ends of the cores. The system was controlled by an MTS-TESTAR II control-data collection software package. Lateral strain was measured by CDI Logic Basic digital displacement gages that measured displacements to 0.001mm. These gages were mounted 120° apart on an adjustable plate

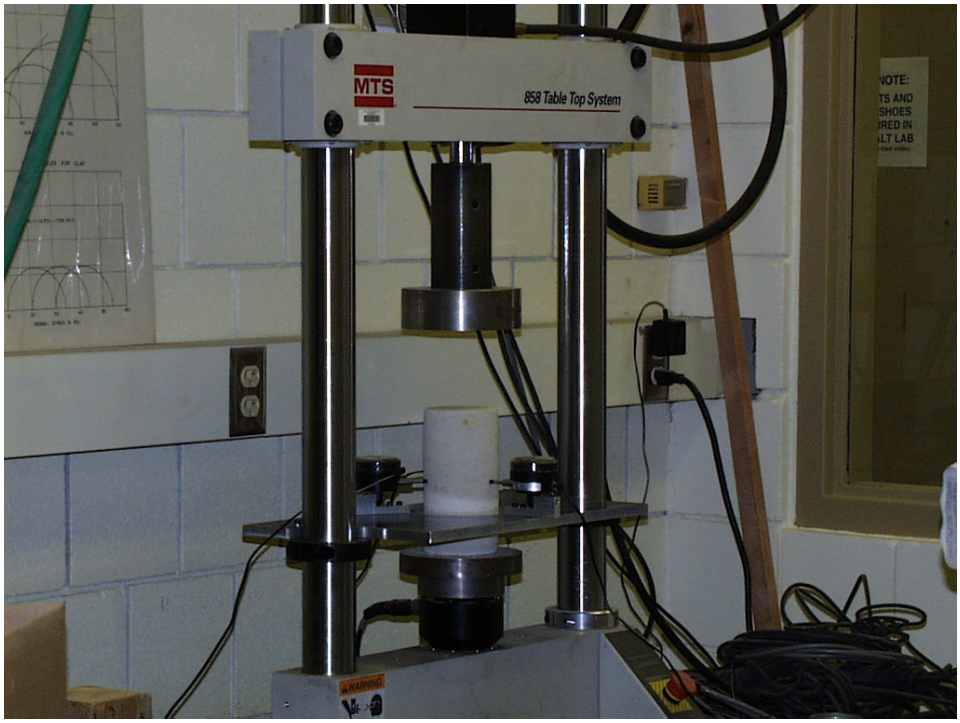

Figure 3-28: St. Peter sandstone core ready for uniaxial testing.

that allowed the gages to be placed at mid-height of the samples (Figure 3-28).

Uniaxial testing for this project differed from previous testing. Adherence to a 2:1 aspect ratio was held to, and the ends of the cores were not capped with hydrostone or separated from the platens in any way. Peterson (1978) reported difficulty in trying to determine whether capping the ends of the cylinders affected the strength. The hydrostone caps (in general) did not break, and the paper used to reduce friction for the

cubes was reported torn demonstrating considerable expansion of the samples when tested. A constant displacement rate of 0.10 mm was used for all tests.

The test results were quite variable and on the smaller samples trying to establish a value for Poisson's ratio from axial and lateral strain was difficult at best (Figure 3-29).

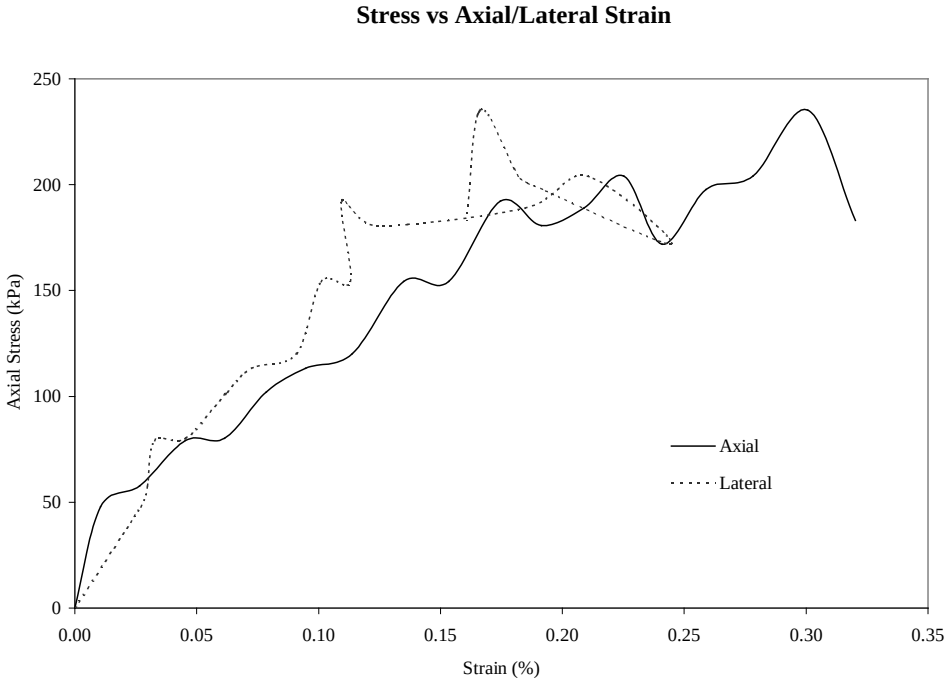

Figure 3-29: Uniaxial test results on St. Peter sandstone cores with an average diameter of 4.67cm.

The largest samples provided the most consistent results (Figure 3-30). As the samples decreased in diameter, the values for unconfined compressive strength decreased as did the values for Young's modulus (Table 3-15). In addition, lateral strains started to match up with axial strains quite closely (Figure 3-29). It is possible that this is the result of dilation in the samples, but more likely these aberrations were the result of damage done to the samples when they were made.

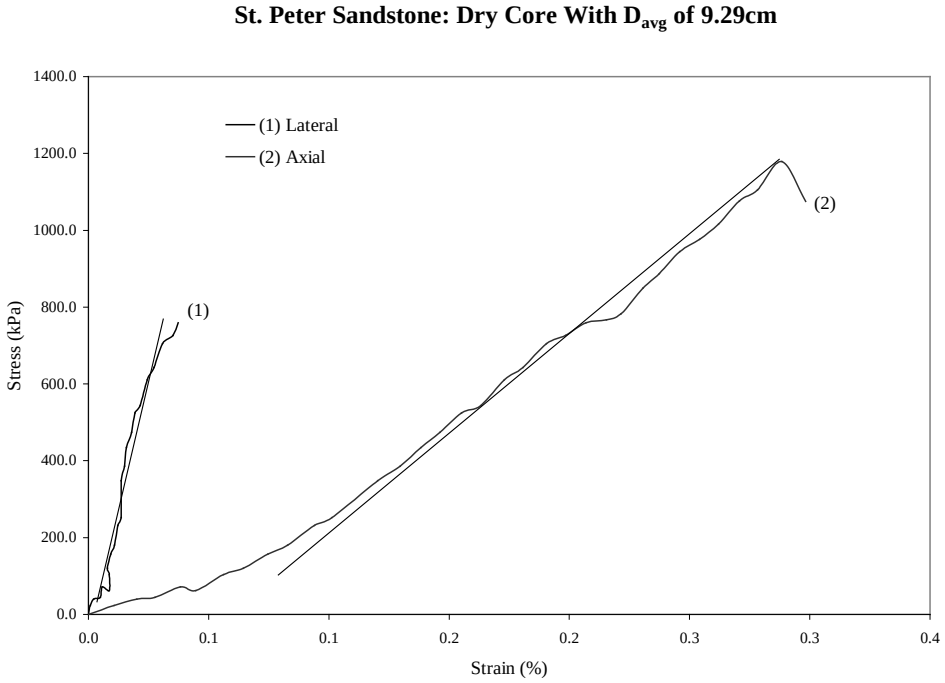

Figure 3-30: Uniaxial test on St. Peter sandstone. Poisson's ratio calculated from the ratio of slopes of lateral and axial strain is low ($v = 0.20$) but still within the recorded range of values.

Table 3-15: Results of uniaxial testing on St. Peter sandstone.

Test	Diameter (cm)	Unconfined Compressive Strength (kPa)	Young's Modulus (kPa)	E_{lat} (kPa)	Poisson's ratio
1	9.29	1179	495,560	2,489,557	0.20
2	9.29	388	261,695	1,433,578	0.18
3	9.29	836	403,914	792,754	0.51
4	5.58	693	357,646	N/A	N/A
5	5.58	699	364,859	N/A	N/A
6	5.58	591	239,297	N/A	N/A
U-1	7.62	236	2,577,177	N/A	N/A

Looking at the results, three things were readily apparent. Values for unconfined compressive strength were low, with the exception of test 1. The second is the values for Young's modulus, with the exception of test U-1, were quite low when compared to the

results of previous researchers. The third is that the values for Poisson's ratio were variable and rather low, though they were certainly within the range of values recorded.

Plate Load Tests

Field bearing tests were performed by the U.S. Army corps of Engineers (1952) to establish the foundation modulus. The foundation modulus (*K*) is found with the following expression:

$$EI\frac{d^4y}{dx^4} = q(x) - Ky$$

These tests were done using three different size load plates (76cm, 122cm, and 183cm in diameter). The results of these tests yielded an average $K = 235{,}769\ KN/m^3$.

Permeability

Permeability testing was performed by the U.S. Army Corps of Engineers (1939) on intact and unconsolidated samples that were extracted from the Ford sand mine at elevations between 216 and 219 meters above mean sea level. Sixteen permeability tests were run on the sandstone blocks collected and on the sand from the blocks. Seven tests were run on intact blocks and from those seven tests and average permeability of 0.0029 cm/sec was measured, and the sand samples tested had an average measured permeability of 0.0126 cm/sec. The sand exhibited an average permeability that was approximately 4 times greater than the sandstone samples.

MICROSCOPIC ANALYSIS

Thin Section Analysis

Thin sections were made using Buehler EPO-THIN low viscosity impregnating resin and hardener. The samples had to be impregnated before they could be shaped and attached to the slides. The samples were impregnated under a vacuum and allowed to cure at room temperature (~22° C) for 24 hours (Figure 4-1). Due to the friable nature of

Figure 4-1: Vacuum apparatus used to evacuate the impregnating resin and the pore space in the St. Peter sandstone samples.

the St. Peter sandstone, considerable care was necessary to make the thin sections, especially the samples that were saturated and sheared. The first attempts to impregnate samples failed rather spectacularly. The sample cups were filled with impregnating resin up to approximately 75% of the sample height, and the samples were left under an active

vacuum for 12 hours. The result is that the samples "exploded," and all that was visible was hardened resin bubbles with St. Peter sandstone fragments and grains trapped between the bubbles. The next attempts were much more successful.

Approximately 3mm of resin was poured into the bottom of the cup and the sample and resin were evacuated for 45 minutes. This vacuum time ensured that all the air was evacuated from the resin and the sandstone samples. The pump was then turned off and the samples were allowed to sit overnight in a static vacuum. While air did infiltrate overnight, the vacuum remained sufficiently long to allow capillary action to pull the resin up through to the top of the samples, resulting in a completely impregnated sample.

The next step was to prepare the sample and the slide for mounting. The samples need to be cut and shaped to fit the slide. The samples were cut with a diamond-coated saw, and the surface to be mounted was flattened with a lap wheel using #240 carbide grit and water. The slides have a dimension of 27mm x 46mm and have to be prepared as well; this was done by roughing one face of the slide with #400 carbide grit and water on a #400 glass plate.

When the slides were roughed and the samples were smoothed and flattened, the samples were ready to be mounted. The glass slides were coated with the same impregnating resin and the sample was placed on the slide. The sample was moved on the slide forcing out any air bubbles that may have been trapped between the sample and slide. Then the thin section assembly was placed in an oven at 45^{o} C overnight to cure.

When the resin cured, the slides were mounted in a thin section saw and cut to a thickness of approximately 80 microns. Once these samples were cut, they were ground

lightly with a diamond-coated grinding wheel. The next step was to reduce their thickness to approximately 40 microns for cross-polarized light analysis. Since the work done in this research involved plane-polarized light and SEM, strict adherence to a thickness of 40 microns was not necessary. The thin sections were smoothed using increasingly fine carbide grit and finally polished to a shine using 9-micron and 6-micron carbide grit suspended in oil on a lap wheel.

Thin sections were studied using both transmitted plane polarized light, and by Scanning Electron Microscopy (SEM). For this paper, samples were studied that are intact (both parallel and perpendicular to bedding), saturated and sheared, and pulverized (dry and saturated). The effort behind thin section analysis was to try to verify the existence of locked sand grains (Dusseault and Morgenstern, 1979), and to try to see post-depositional quartz overgrowths that provide an "interlocking finger" effect (Pittman, 1972; Mazzullo and Ehrlich, 1983). It is thought that these parameters are the reasons for the St. Peter sandstone's uncommonly high angle of internal friction

Locked Sand Grains

Cohesionless sands typically are classified according to density and a distinction commonly used is whether the sand is loose or dense. In addition there is another class of cohesionless sands. Called locked sands, these sands are made up of predominantly sand-size particles and exhibit an in situ relative density of greater than 100% according ASTM standards for achieving minimum porosity of the pulverized material (Dusseault and Morgenstern, 1983). These locked sands exhibit almost no contraction while being tested in direct shear, and have very high rates of dilation at failure (Figure 4-2), and subsequently have peak frictional strengths considerably higher than strengths exhibited

by dense sands (Figure 4-3). As normal stress is increased, the high dilation rates are subdued resulting in a highly curved Mohr-Coulomb failure envelope (Figure 4-4).

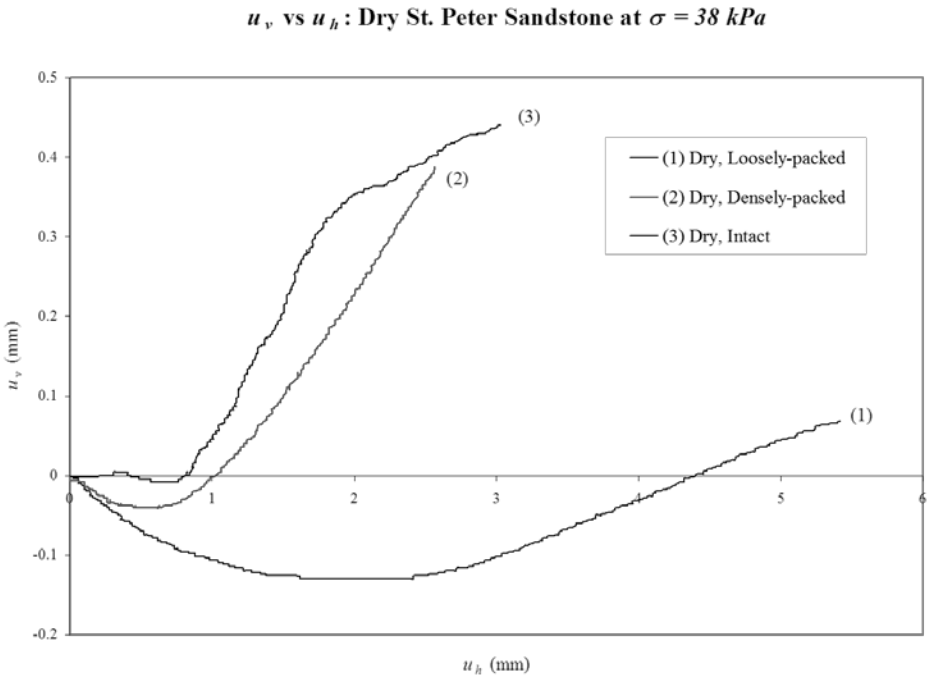

Figure 4-2: Comparison of rates of dilation from St. Peter sandstone samples that have undergone direct shear testing.

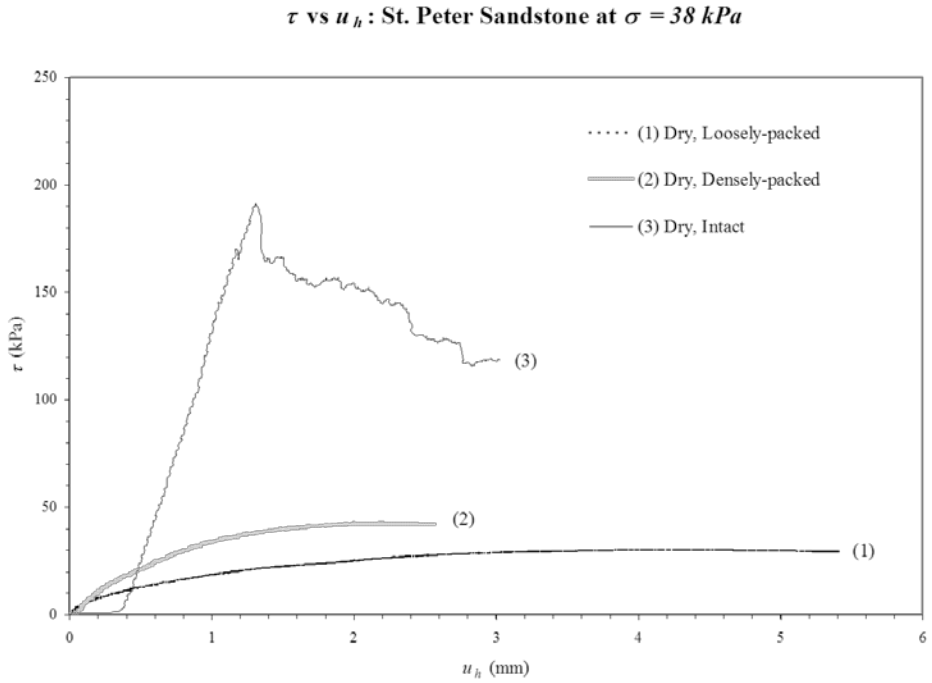

Figure 4-3: Comparison of peak frictional strengths in St. Peter sandstone.

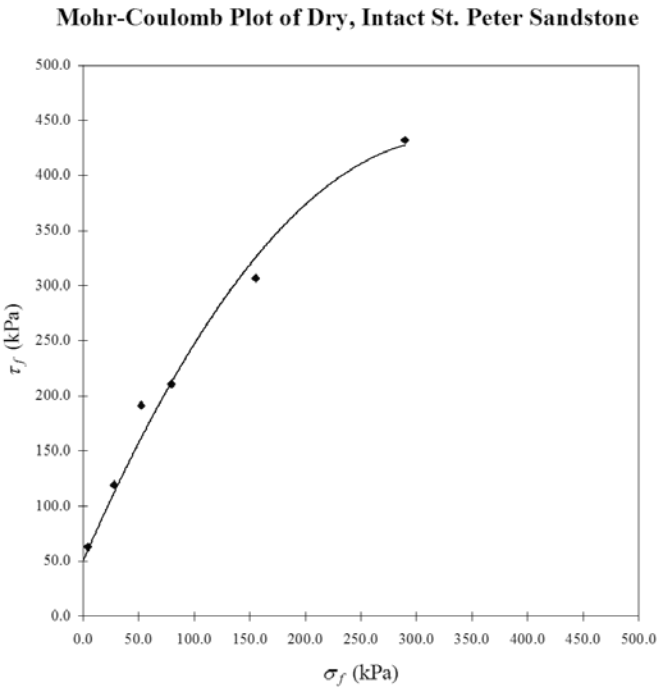

Figure 4-4: Mohr-Coulomb failure envelope of intact St. Peter sandstone failed in direct shear.

The peculiar fabric that locked sands develop is attributed to diagenetic processes that reduce porosity while leaving an essentially uncemented structure. The result of these processes is sand with increased strength, possibly due to its high dilatancy (Dusseault and Morgenstern, 1983).

Transmitted light and scanning electron microscopes were used to identify interlocking textures and interpenetrative contacts. The contacts between grains may be tangential, concavo-convex, sutured or straight. These contacts are dependent on variations in solubility as a result of impurities, and differences in radii of curvature, resulting in the smaller grain penetrating into the larger grain (Figure 4-5). It is important to note that impurities such as clay and hematite occur on St. Peter sandstone grains in

the form of flakes and laminae. These impurities favor pressure solution over secondary quartz (Pittman, 1972).

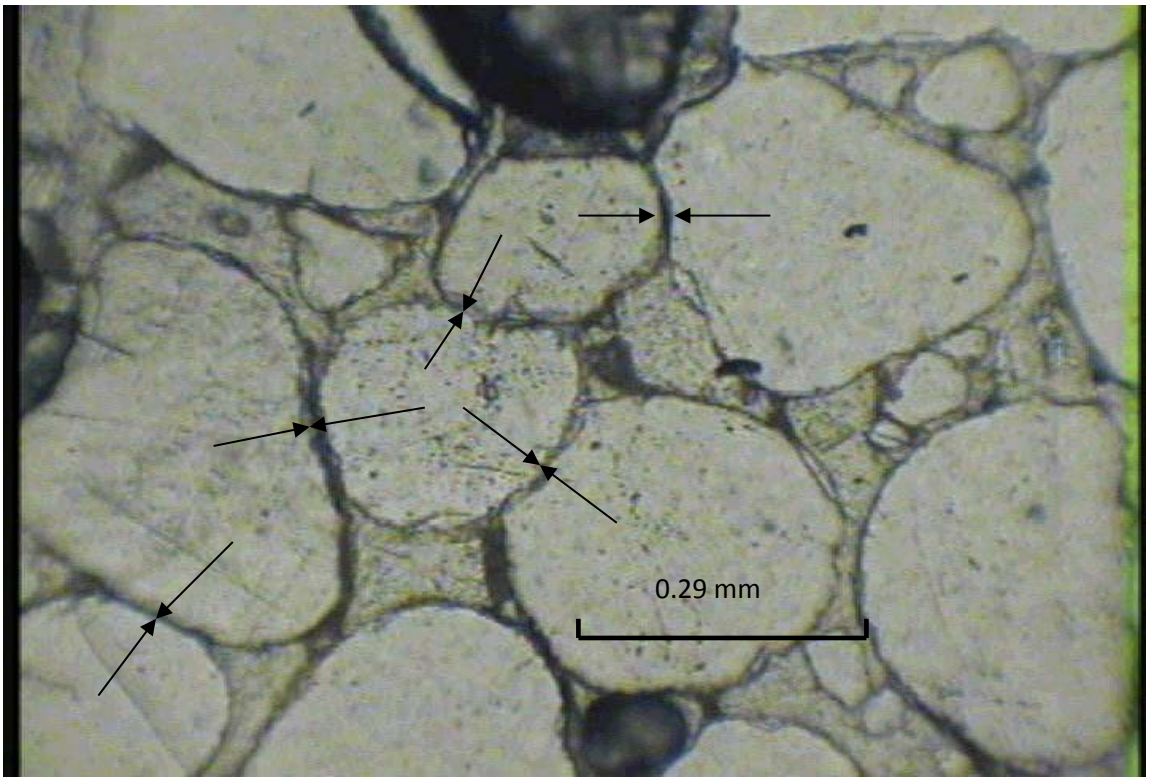

Figure 4-5: Transmitted light photo-micrograph of intact St. Peter sandstone clearly showing locked grains.

Quartz Overgrowths

A scanning electron microscope was used to try to find post-depositional quartz overgrowths that are responsible for the interlocking "finger effect" described by Pittman (1972) and Mazzullo and Ehrlich (1983). The process leading to quartz overgrowths is complex. Post-depositional overgrowths may occur as growths with poorly defined crystal faces that form an interconnected anastomosing system over the grain's surface, or isolated growths with well-defined crystal faces. It is also common to see the formation of secondary quartz growths in the form of incompletely developed crystal faces resulting from the merger of irregular overgrowths (Pittman, 1972). The surface of

loose grains yielded some evidence of post-overgrowths on larger grains (Figure 4-6). This photo shows not only a point contact depression in the surface of the grain,

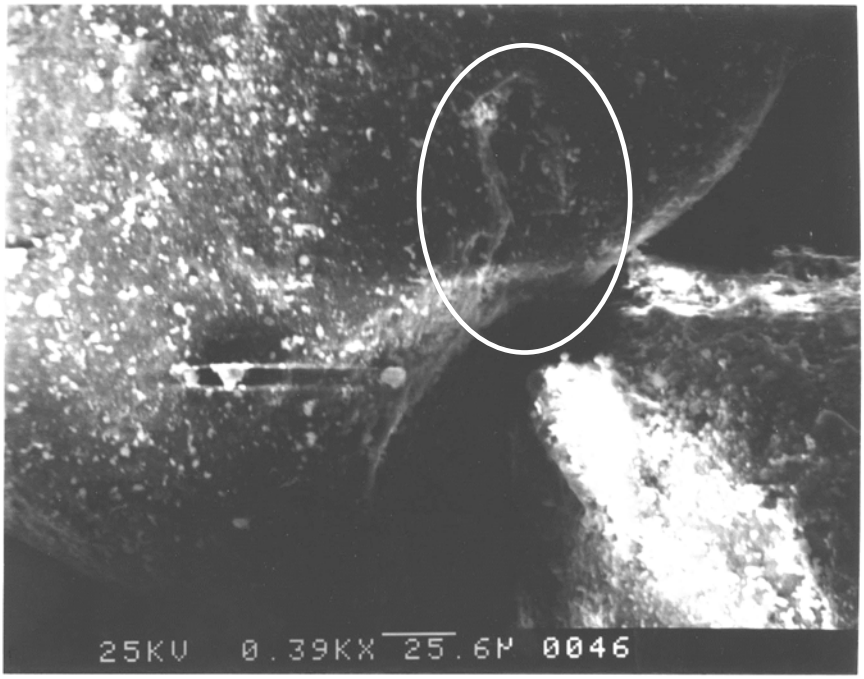

Figure 4-6: SEM micrograph of St. Peter sand grain surface showing a contact depression in the grain surface, and also showing evidence of tearing of the grain surface, possibly due to post-depositional quartz overgrowths.

but there is also a tear in the grain's surface starting within the depression and moving out beyond the rim. What is also visible, is a considerable amount of clay on the surface of the grains, as well as a rime of clay surrounding the penetration boundary. SEM reflects more intensely off certain types of minerals than others. Clay minerals reflect more intensely than does quartz. The clay minerals show up as bright spots on the dark background of the quartz grain. What is also evident from an analysis of the loose grains is that the grains become more angular as they diminish in size (Figure 4-7A-E). Typically, as the erosive process continues, quartz grains become more rounded as they

become smaller. This process continues until they are slowly dissolved as molecules are carried into solution.

(A) #40-size St. Peter sand grains.

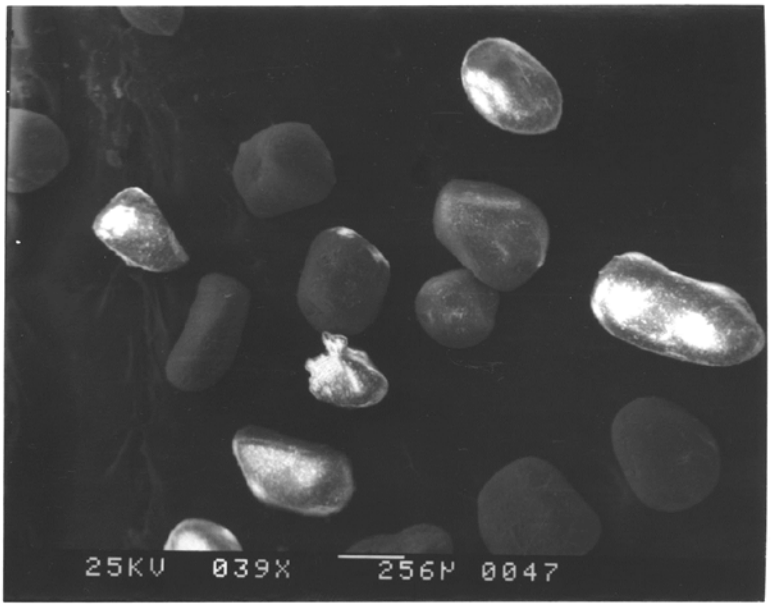

(B) #60-size St. Peter sand grains.

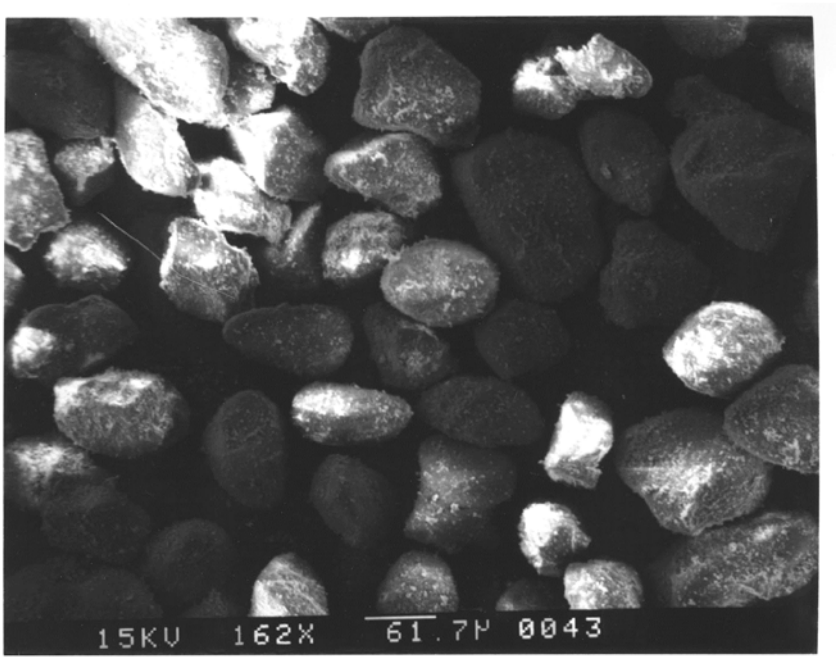

(C) #100-size St. Peter sand grains.

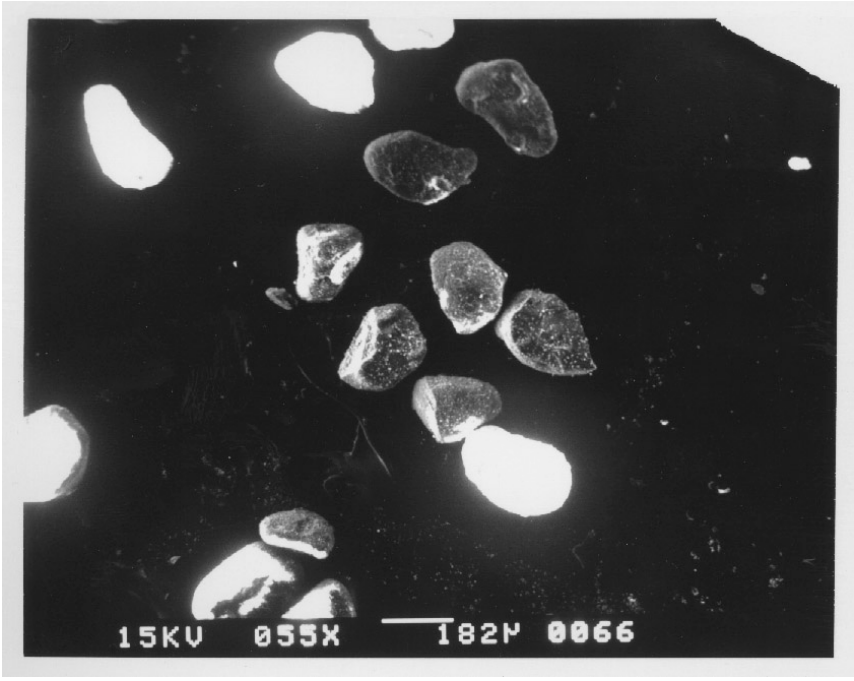

(D) #200-size St. Peter sand grains.

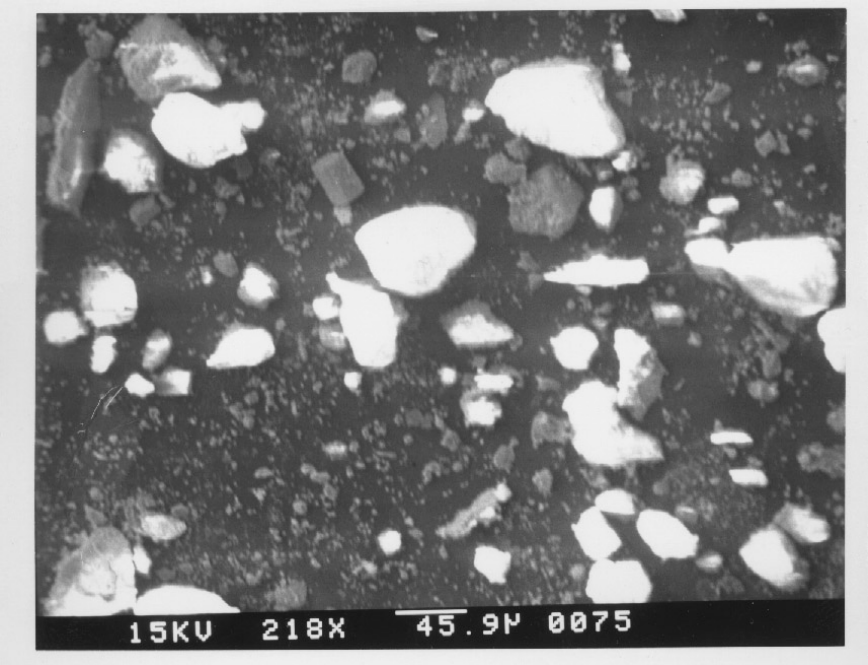

(E) St. Peter fines.

Figure 4-7A-E: Shape comparison of distributed grain sizes of St. Peter sandstone. Very evident is increasing angularity as grain size decreases.

What is seen in Figure 4-7 is a considerable amount of clay and iron oxides on the surface of the sand grains and these impurities occur as flakes and laminae on the grain's surface. Examining thin sections of dry, pulverized samples, there is evidence of pressure solution products that surround the grain contacts in a rime (Figure 4-8). This rime is a mixture of quartz, iron oxides and clay minerals that all dissolved into solution under post-depositional pressure and later recrystalization along the edge of the grain contact. The elemental composition of the rime is shown in Table 4-1. All that can be said about this rime is that it contains elements of clays, quartz and iron oxides. These minerals dissolved under pressure and in solution, but it is not clear that these same minerals precipitated out along the edge of the grain contacts.

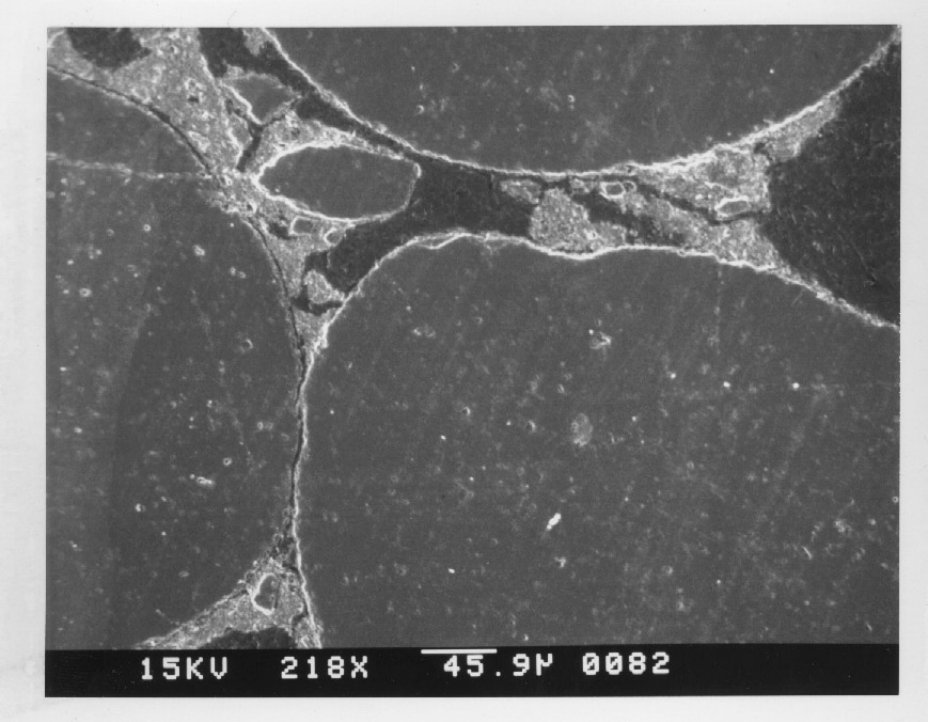

Figure 4-8: SEM micrograph of St. Peter sandstone grain contacts. Clearly evident are rimes at grain contact boundaries.

Table 4-1: Elemental composition of rime minerals in Figure 4-8.

Element	K	[Z]	[A]	[F]	[ZAF]	Atomic %	Weight %
Si-K	0.424	0.974	1.276	0.998	1.240	48.71	44.21
Ti-K	0.009	1.105	1.050	0.992	1.151	0.54	0.83
Al-K	0.226	1.006	1.168	0.984	1.156	25.06	21.93
Fe-K	0.108	1.115	1.011	1.000	1.127	5.66	10.28
Mg-K	0.027	0.962	1.258	0.986	1.193	3.43	2.67
Mn-K	0.003	1.131	1.017	1.000	1.150	0.16	0.28
Ca-K	0.006	1.003	1.103	0.997	1.103	0.42	0.54
K-K	0.151	1.025	1.099	0.997	1.124	11.32	14.31
Na-K	0.000	0.998	1.482	0.993	1.469	0.00	0.00
S-K	0.039	0.985	1.304	0.996	1.279	4.06	4.21
Cl-K	0.007	1.018	1.216	0.992	1.228	0.64	0.73

FIELD RESULTS

Pressuremeter Testing

Introduction

It has been shown that the action of sampling causes significant disturbance due to differences in stress history between laboratory and field elements. Mechanical deformation of cohesive samples or total rearrangement of granular samples can cause these differences in stress history. One method used to overcome these difficulties is the pressuremeter test. The pressuremeter is a test that, when properly performed, can replace some routine laboratory testing on the grounds of both improved accuracy and more favorable economics (Windle and Wroth, 1977).

The pressuremeter test is less expensive than plate load tests, yet it still provides moduli and shear strength values through direct measurements and the use of established theories (Windle and Wroth, 1977). Developed by Menard in 1957, the pressuremeter is made up of two main components: the probe, which can be placed in an existing borehole or is of a self-boring type, and the control module where fluid is injected and the corresponding pressure is monitored.

System Saturation

The pressuremeter is first saturated. Under most conditions this is done with water but in the present study, a 50/50 mixture of water and propylene-glycol was used to allow testing to be done in sub-freezing conditions.

Saturation of the system is done in three stages:

1) saturation of the cylinder,

2) saturation of the gauges, and

3) saturation of the tubing assembly.

A detailed description of these procedures can be found in Appendices (Appendix A through D).

Bladder Stiffness Calibration

When testing soils, bladder resistance becomes an important calibration factor; whereas system stiffness is not taken into account because soil is sufficiently compliant and the system can be taken as infinitely stiff. For relatively stiff materials, such as the St. Peter sandstone, bladder stiffness does not need to be taken into account but the bladder must still be calibrated to ensure it meets proper specifications as set by the manufacturer.

Calibrating for bladder stiffness is done by injecting fluid into the probe in 20 increments of 60 cm^3. After each volume step the pressure is read after 30 seconds has elapsed. The slope of the line of Δp versus ΔV is related to bladder stiffness.

To determine the stiffness of the bladder, it is necessary to determine the ratio of pressure to displacement. By assuming that the bladder expands radially only along the contact length, ΔV can be changed to radial displacement. This is done by first calculating volumetric strain (e)

$$e = \frac{\Delta V}{V_0} \tag{5-1}$$

where V_0 = the initial volume of the probe, and ΔV = the volume of fluid injected at each test step. The radial displacement (u_r) is then calculated with the expression

$$u_r = \frac{R_0 \Delta V}{2V_0} \qquad (5-2)$$

where R_0 = the initial inside radius of the probe. The stiffness of the bladder (k_b) can be calculated from the slope of the linear portion of Figure (5-1).

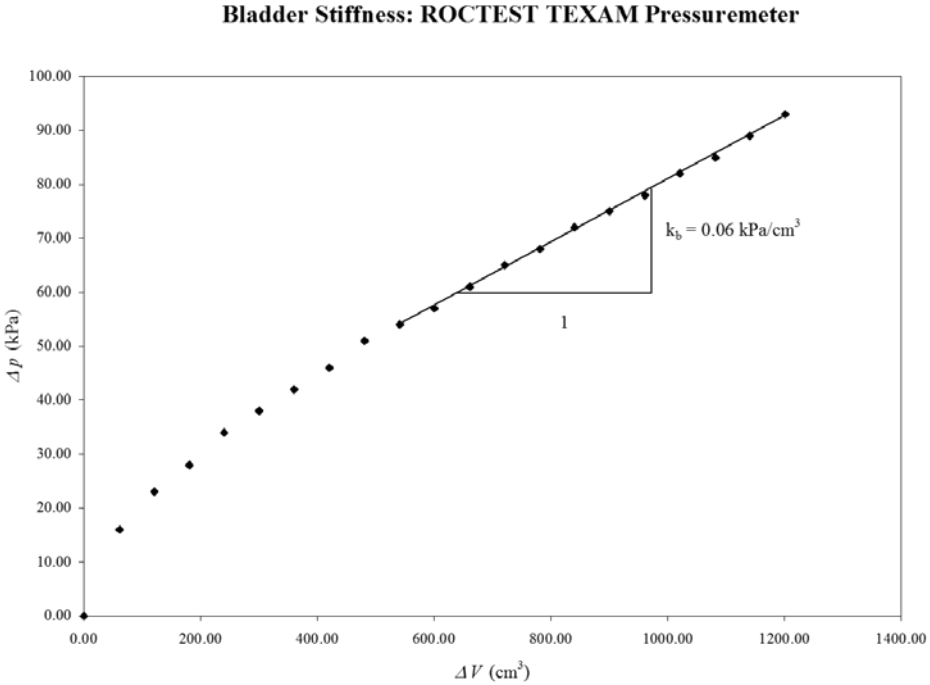

Figure 5-1: Curve for bladder resistance of the ROCTEST TEXAM Pressuremeter.

System Stiffness Calibration

Calibrating the pressuremeter for system stiffness involves calibrating the probe in an instrumented tube of known characteristics. Calibration of the system was done using a tube with approximately the same dimensions as the probe assembly. The tube used was a type 1020AK, DOM-welded (Drawn Over Mandrel) steel tube. The tube was 98.43 centimeters (38.75 inches) long with an inside diameter (ID) of 7.62 centimeters (3.00 inches), and a wall thickness of 0.31 centimeters (0.13 inches). The tube was grade 60 steel and has a yield stress (σ_y) of 413 MPa (60 ksi), a Poisson's ratio (ν) of 0.3, and a

tensile strength (T_t) of 482 MPa (70 ksi). The calibration tube was designed to stand upright and was welded to a steel plate with a 25.40-centimeter (10 inches) diameter and a 1.11 centimeters (0.44 inches) thickness. The calibration tube was instrumented with three Measurements Group, Inc. type EA-06-250BG-120 strain gages with a gage factor of 2.075, and were mounted at 120° intervals and arranged to measure tangential strain ($\varepsilon_{\theta\theta}$). The strain gages were connected to a Measurements Group model SB-10 Switch and Balance unit and a Measurements Group model P-3500 Strain Indicator in a quarter-bridge configuration (Figure 5-2).

Figure 5-2: Pressuremeter calibration tube assembly.

Stress analysis follows from the Lame solution. The expressions for calculating radial and tangential stresses are (tension positive)

$$\sigma_{rr} = \frac{b_0}{r^2} + 2c_0 \qquad (5-3)$$

$$\sigma_{\theta\theta} = -\frac{b_0}{r^2} + 2c_0 \qquad (5-4)$$

$$\tau_{r\theta} = 0 \qquad (5-5)$$

where

$$\sigma_{rr} = -p_i \qquad \text{at } r = a \qquad (5-6)$$

$$\sigma_{rr} = -p_o \qquad \text{at } r = b \qquad (5-7)$$

$\tau_{r\theta} = 0$ because the applied pressure is radial and symmetric.

Since the system is symmetric, u_r is independent of θ and $u_\theta = 0$. The variables, b_0 and c_0, can be evaluated by applying the remaining boundary conditions to

$$\sigma_{rr} = \frac{b_0}{r^2} + 2c_0 \qquad (5-3)$$

leading to

$$\sigma_{rr} = -p_i = \frac{b_0}{a^2} + 2c_0 \qquad (5-3a)$$

$$\sigma_{rr} = -p_o = \frac{b_0}{b^2} + 2c_0 \qquad (5-3b)$$

There are now two expressions with two unknowns (b_0 and c_0). Solving these expressions for one of the unknowns yields

$$b_0 = \frac{a^2 b^2 (p_i - p_o)}{a^2 - b^2} \qquad (5-8)$$

Substitution into expression $\sigma_{rr} = -p_i$ leads to

$$-p_i = \frac{a^2 b^2 (p_i - p_o)}{(a^2 - b^2) a^2} + 2c_0 \tag{5-9}$$

Setting the expression equal to c_0 yields

$$c_{00} = \frac{b^2 p_o - a^2 p_i}{2(a^2 - b^2)} \tag{5-10}$$

Substitution into the initial expressions results in

$$\sigma_{rr} = \frac{a^2 b^2 (p_i - p_o)}{(a^2 - b^2) r^2} + \frac{b^2 p_o - a^2 p_i}{a^2 - b^2} \tag{5-11}$$

$$\sigma_{\theta\theta} = -\frac{a^2 b^2 (p_i - p_o)}{(a^2 - b^2) r^2} + \frac{b^2 p_o - a^2 p_i}{a^2 - b^2} \tag{5-12}$$

$$u_r = \frac{1}{E}\left[-(1+\nu)\frac{a^2 b^2 (p_i - p_o)}{(a^2 - b^2) r} + (1-\nu) r \left(\frac{b^2 p_o - a^2 p_i}{(a^2 - b^2)} \right) \right] \tag{5-13}$$

For the case of the calibration tube, the external pressure $p_o = 0$. The above expressions reduce to

$$\sigma_{rr} = \frac{a^2 b^2 p_i}{(a^2 - b^2) r^2} - \frac{a^2 p_i}{a^2 - b^2} \tag{5-14}$$

$$\sigma_{\theta\theta} = -\frac{a^2 b^2 p_i}{(a^2 - b^2) r^2} - \frac{a^2 p_i}{a^2 - b^2} \tag{5-15}$$

$$u_r = \frac{1}{E}\left[-(1+\nu)\frac{a^2 b^2 p_i}{(a^2 - b^2) r} - (1-\nu) r \left(\frac{a^2 p_i}{(a^2 - b^2)} \right) \right] \tag{5-16}$$

By setting $r = b$

$$\sigma_{rr} = \frac{a^2 p_i}{(a^2 - b^2)} - \frac{a^2 p_i}{a^2 - b^2} = 0 \tag{5-17}$$

$$\sigma_{\theta\theta} = -\frac{a^2 p_i}{(a^2 - b^2)} - \frac{a^2 p_i}{a^2 - b^2} = -\frac{2a^2 p_i}{a^2 - b^2} \tag{5-18}$$

$$u_r = \frac{1}{E}\left[-\frac{a^2 b p_i}{(a^2 - b^2)} (3-\nu) \right] \tag{5-19}$$

Generalized Hooke's law for an isotropic solid gives

$$\varepsilon_{rr} = \frac{\sigma_{rr}}{E} - \frac{\nu}{E}\left(\sigma_{\theta\theta} + \sigma_{zz}\right) \quad (5\text{-}20)$$

$$\varepsilon_{\theta\theta} = \frac{\sigma_{\theta\theta}}{E} - \frac{\nu}{E}\left(\sigma_{rr} + \sigma_{zz}\right) \quad (5\text{-}21)$$

$$\varepsilon_{zz} = \frac{\sigma_{zz}}{E} - \frac{\nu}{E}\left(\sigma_{rr} + \sigma_{\theta\theta}\right) \quad (5\text{-}22)$$

Because $p_o = 0$, the derivation for the expression for σ_{rr} shows that $\sigma_{rr} = 0$. The strain gages were positioned to measure tangential strain, and the system was treated as plane strain

($\varepsilon_{zz} = 0$).

The first step to calibrating the system was to seat the probe in the calibration tube. This was done by injecting fluid into the probe. Fluid was injected until the probe cannot be removed by hand. This constitutes a seated probe. The volume of fluid necessary to achieve this was the seating volume (V_S). When the probe was seated in the calibration tube, the strain values measured by the strain indicator at the seating volume for the three gages were recorded as initial values.

The calibration test itself was done by injecting fluid into the probe in pressure steps of 50 kPa until the pressure indicator reaches 500 kPa. Then the fluid was injected in pressure steps of 500 kPa until the system reached its maximum value of 10,000 kPa.

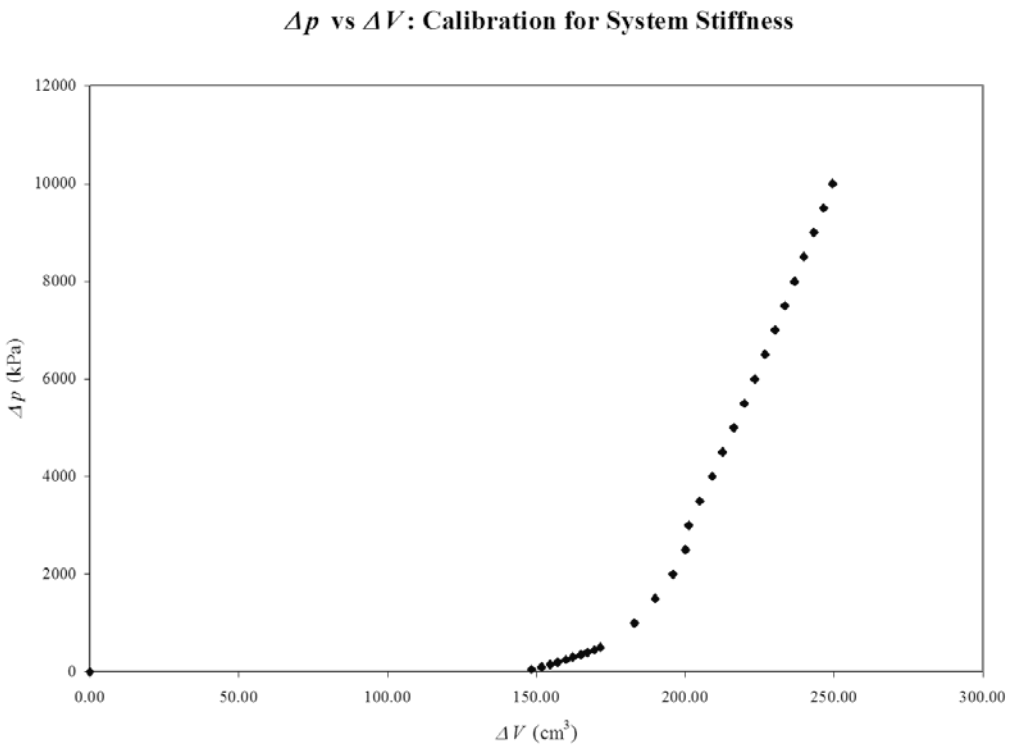

Figure 5-3: Pressuremeter system calibration curve with the seating volume subtracted.

Pressure values were recorded 30 seconds after the pressure step was reached. The strain values were recorded at the same time the pressure values were recorded.

The results were zeroed by subtracting the seating volume and subtracting the initial strain values from the raw data. The values for Δp vs ΔV were plotted to determine the linear portion of the calibration test (Figure 5-3). The values for pressure vs strain were plotted to show the uniform character of the calibration tube under symmetric radial stress (Figure 5-4).

As shown in figure 5-4, channel 3 deviates slightly on the low side from channels 1 & 2. This may be the result of poor bonding of the strain gage by the epoxy, or poor electrical connections. Channels 1 & 2 show very good consistency throughout the calibration test, and channel 3 has been treated as an outlier.

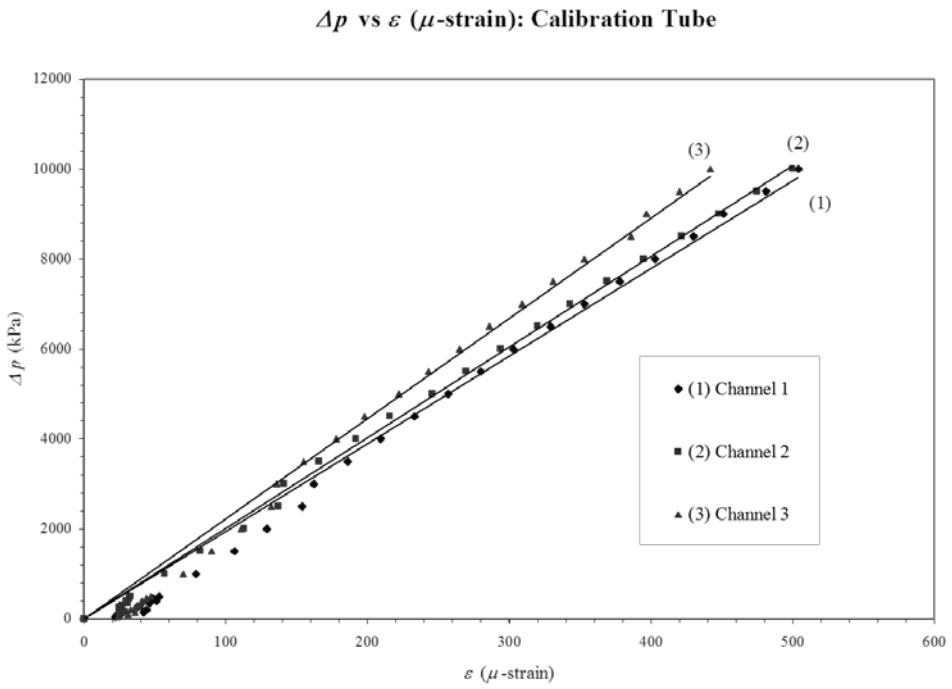

Figure 5-4: Measurements of strain (μ-strains) from the pressuremeter calibration tube.

For calibrating the pressuremeter, the linear portion of the graph is important since this is the portion of the graph that will provide the system stiffness. The linear portion of the curve is plotted and the value of the x-intercept is subtracted from the values of the points on the curve and replotted. By taking the value of the x-intercept and subtracting it from the values of the linear portion of the curve, the values for ΔV are determined. Using these values, the volumetric strain of the calibration tube can be calculated (Figure 5-6).

The next step is to calculate the volumetric expansion of the calibration tube. This is done by calculating the initial volume of the tube that is in contact with the probe's expansible bladder. A constant contact length of 46.10 centimeters was assumed

and used for the calibration and field tests. With the strain gages placed on the outside of the calibration the hoop stress ($\sigma_{\theta\theta}$) on the exterior of the tube using the expression

$$\sigma_{\theta\theta} = \frac{a^2 p_i}{b^2 - a^2}\left(1 + \frac{b^2}{r^2}\right) \tag{5-23}$$

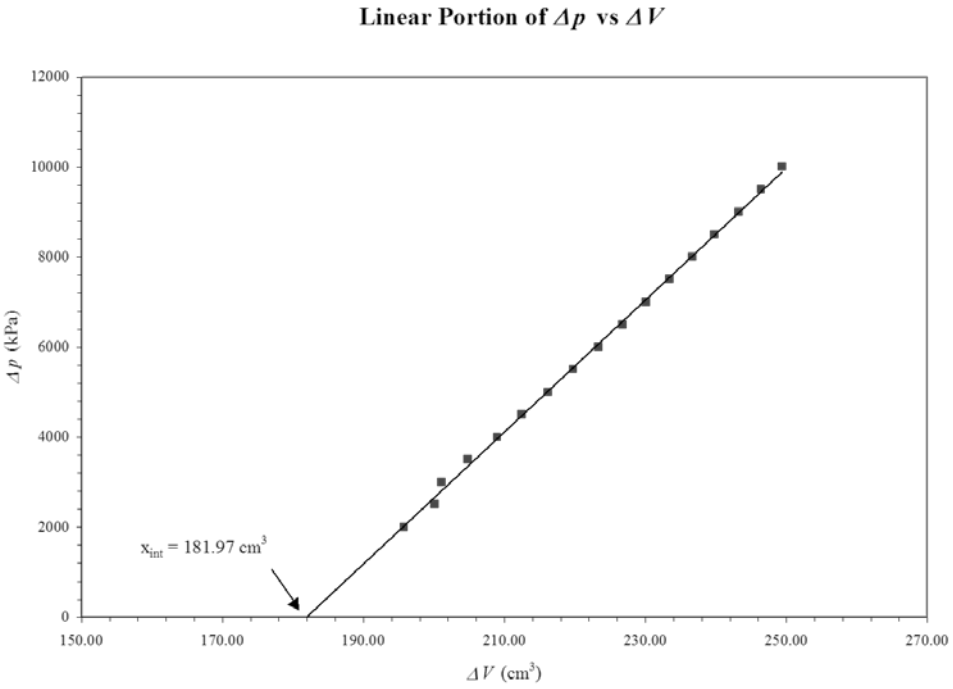

Figure 5-5: Linear portion of the Δp vs ΔV plot showing the slope and the x-intercept.

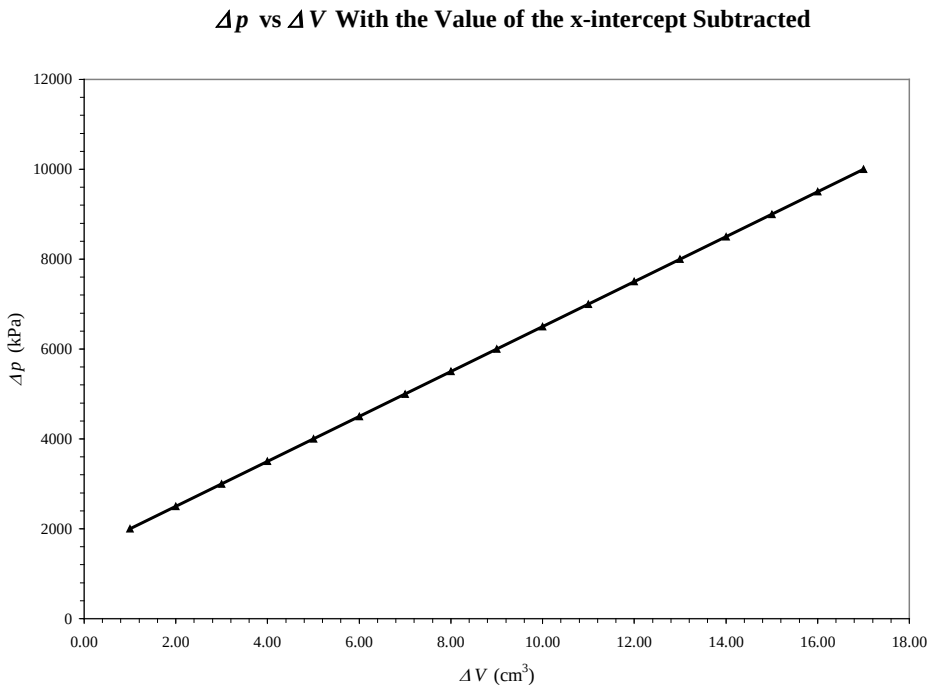

Figure 5-6: Δp vs ΔV for the calibration tube after V_S and the x-intercept have been subtracted.

When $r = b$, expression (5-23) reverts to expression (5-18). From the values of stress and strain on the exterior of the calibration tube, and generalized Hooke's law, an average value for Young's modulus (***E = 218.83 GPa***) was calculated. At $r = a$, and using expression (5-23), the hoop stress on the inside face of the calibration tube can be calculated. Using the values for hoop stress along with the calculated value for Young's modulus, the strain values on the inside face can be calculated, and from that, the radial displacement values can also be determined (Table 5-1).

Table 5-1: Calculated values of tangential stress ($\sigma_{\theta\theta}$) and radial displacement (u_r) for the pressuremeter in the calibration tube.

Pressure, p_i (kPa)	**Pressure, p_{30} (kPa)**	**average (μ-strain)**	**$\sigma_{\theta\theta}$ (MPa)**	**u_r (cm)**
1000	950	68.0	12.46	2.23E-04
1500	1450	94.0	18.69	3.34E-04
2000	1960	113.9	24.92	4.45E-04
2500	2440	142.3	31.14	5.57E-04
3000	2970	170.8	37.37	6.68E-04
3500	3440	199.2	43.60	7.79E-04
4000	3975	227.7	49.83	8.91E-04
4500	4445	256.2	56.06	1.00E-03
5000	4950	284.6	62.29	1.11E-03
5500	5430	313.1	68.52	1.22E-03
6000	5910	341.6	74.75	1.34E-03
6500	6420	370.0	80.97	1.45E-03
7000	6920	398.5	87.20	1.56E-03
7500	7410	427.0	93.43	1.67E-03
8000	7910	455.4	99.66	1.78E-03
8500	8410	483.9	105.89	1.89E-03
9000	8910	512.3	112.12	2.00E-03
9500	9410	540.8	118.35	2.12E-03
10000	9910	569.3	124.58	2.23E-03

Using the values obtained in Table (5-1), the values for ΔV and V_{system} can be calculated (Table 5-2), and from those, the system stiffness can be graphically determined (Figure 5-7).

Table 5-2: Values for Δp (kPa) versus ΔV(cm^3), Δp (kPa) versus u_r (cm).

Zeroed Volume (cm^3)	V_{probe} **(cm^3)**	ΔV_{cal} **(cm^3)**	V_{system} **(cm^3)**	u_r **(cm)**	**Pressure, p_i (kPa)**
182.94	0.97	0.25	0.72	2.23E-04	1000
189.91	7.94	0.37	7.57	3.34E-04	1500
195.82	13.85	0.49	13.36	4.45E-04	2000
200.15	18.18	0.61	17.57	5.57E-04	2500
201.12	19.15	0.74	18.41	6.68E-04	3000
204.85	22.88	0.86	22.02	7.79E-04	3500
209.02	27.05	0.98	26.07	8.91E-04	4000
212.53	30.56	1.11	29.45	1.00E-03	4500
216.29	34.32	1.23	33.09	1.11E-03	5000
219.80	37.83	1.35	36.48	1.22E-03	5500
223.35	41.38	1.48	39.90	1.34E-03	6000
226.83	44.86	1.60	43.26	1.45E-03	6500
230.18	48.21	1.72	46.49	1.56E-03	7000
233.44	51.47	1.84	49.63	1.67E-03	7500
236.73	54.76	1.97	52.79	1.78E-03	8000
239.85	57.88	2.09	55.79	1.89E-03	8500
243.28	61.31	2.21	59.10	2.00E-03	9000
246.44	64.47	2.34	62.13	2.12E-03	9500
249.44	67.47	2.46	65.01	2.23E-03	10000

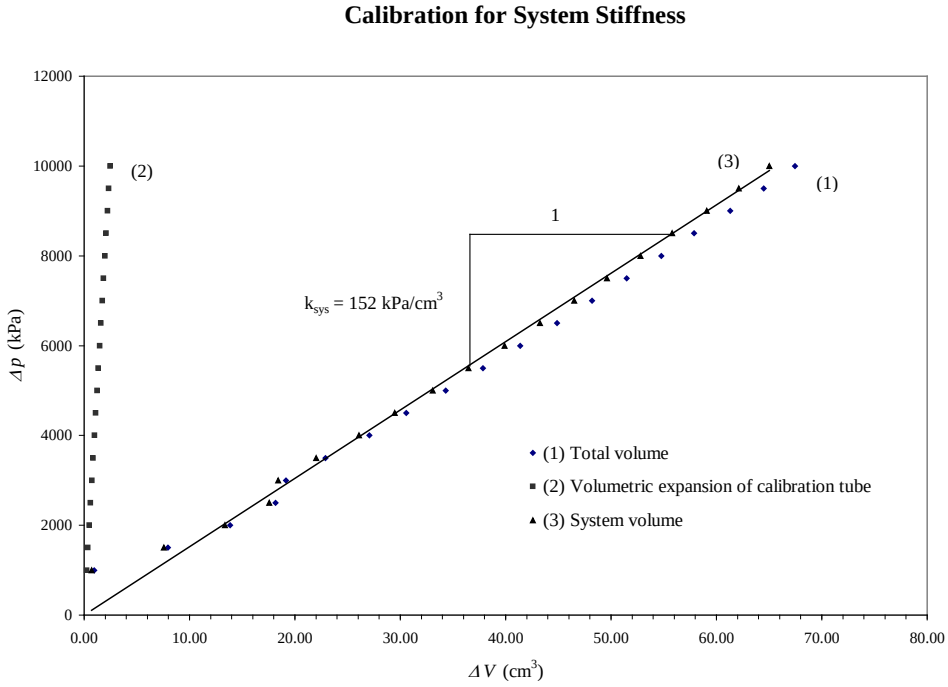

Figure 5-7: Graphical determination of system stiffness.

Pressuremeter Tests

There are two standard procedures for conducting the pressuremeter test. The first type is the stress-controlled test (the Menard test). Constant stress levels are achieved and maintained by injecting fluid into the probe to achieve pressure increments that are one-tenth of p_{max} chosen for the test. In this case p_{max} is the maximum pressure allowed by the system. The pressure exerted by the probe is held constant by continually injecting fluid into the probe. Readings of injected volume are taken initially (at time zero), at 30 seconds, and 60 seconds. Ideally, this test should be done in 10 steps but tests done in as few as seven steps or up to 14 steps are acceptable.

The second procedure is the strain-controlled test. This test is carried out in 20 steps of equal volume increments. For probes that are 44 or 58 mm in diameter, the

volume of fluid injected per step is 40 cc. For probes that are 70 mm in diameter, the volume of fluid injected is 60 cc per step. Fluid is injected in equal increments and the pressure reading is taken 30 seconds after each volume step. Both of these tests are designed to be completed in approximately 10 minutes. Both of these tests require the same steps for system saturation and calibration. The procedures for system saturation and calibration can be found in Appendix B.

Borehole Preparation

Initial attempts to drill boreholes for pressuremeter testing were done horizontally into the excavation face. These attempts were met with difficulties, notably spalling in the borehole. The spalling events started approximately 0.75 m in from the excavation face and proceeded into the back of the borehole. The spalls peaked approximately four centimeters above the top of the borehole. Whether the spalling is a result of gravity breakout or a result of $\sigma_{hor} >> \sigma_{ver}$ is not known.

The next attempts were vertical boreholes into the floor. These were drilled by a 753 Bobcat with a drill attachment and modified auger stems. The auger stems were cut down and were recapped to 7.62 centimeters (3.00 in.). This assembly was capable of drilling vertical boreholes that were nominally 7.7 centimeters (3 in.) in diameter and up to 3.05 meters (10 ft) in depth (Figure 5-8).

Four Menard type tests were conducted on vertical boreholes in the St. Peter sandstone. Borehole #1 was a low pressure test that was carried out in 150 kPa increments to 2400 kPa. Borehole #2 was carried out in 500 kPa increments to a maximum value of 9500 kPa. Boreholes #3 and #4 were done in 1000 kPa increments to the system's maximum value of 10,000 kPa.

Figure 5-8: 753 Bobcat skid loader and drill attachments for drilling boreholes for pressuremeter testing.

Data Correction

As the test is conducted, the data is recorded in the following fashion (Table 5-3).

Table 5-3: Raw data as it is recorded from the control system. This data is from the Menard type test done in borehole #3.

V_S = 185.00 cm^3			
V_i (cm3)	**V_{30} (cm3)**	**V_{60} (cm3)**	**Pressure (kPa)**
185.00	185.00	185.00	0
302.10	302.80	303.25	1000
318.55	319.80	319.85	2000
326.20	327.35	327.50	3000
339.50	340.35	340.70	4000
352.00	353.20	353.65	5000
364.65	365.85	366.30	6000
376.60	377.95	378.55	7000
390.10	391.00	391.20	8000
401.80	403.80	404.40	9000
416.70	418.35	418.80	10000

The raw data from a pressuremeter test has the following appearance when graphed (Figure 5-9). This data needs to be corrected for seating volume (V_S) and because St.

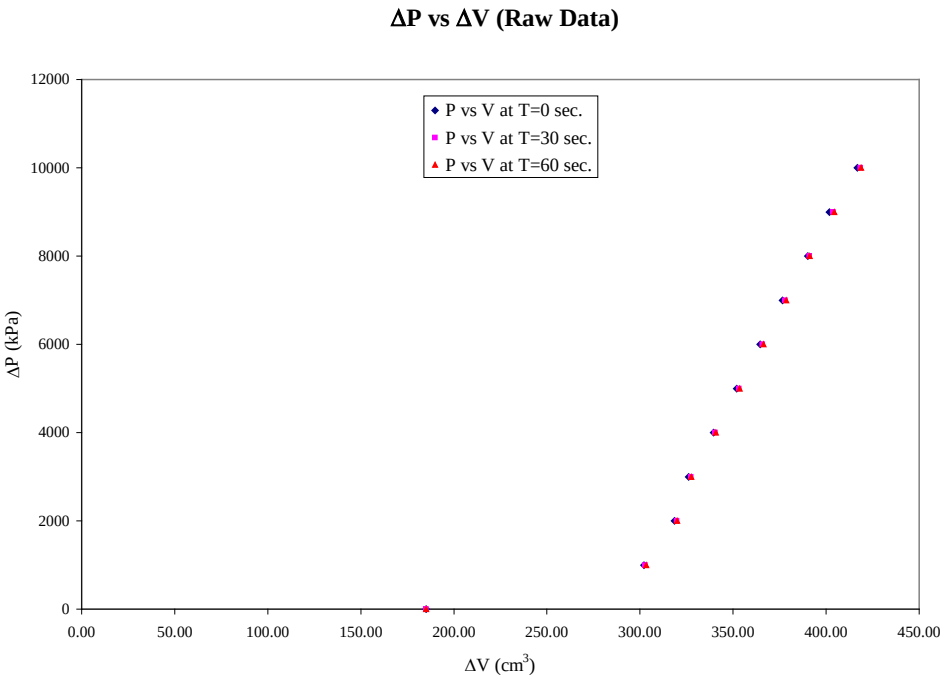

Figure 5-9: Raw pressuremeter data from borehole #3.

Peter sandstone is a relatively stiff material, system stiffness. After the seating volume has been subtracted, the data were further corrected by subtracting the value of the x-intercept. This value was determined by calculating the slope of the linear portion of the curve (Figure 5-10). Subtracting the value of the x-intercept also removed the initial nonlinear portion of the curve. The last step in reducing the data was to correct it for system stiffness using the values calculated for V_{system} (Table 5-2). With this last correction made (Table 5-3), the corrected data were plotted (Figure 5-11). From Figure 5-11, the mechanical properties can be calculated.

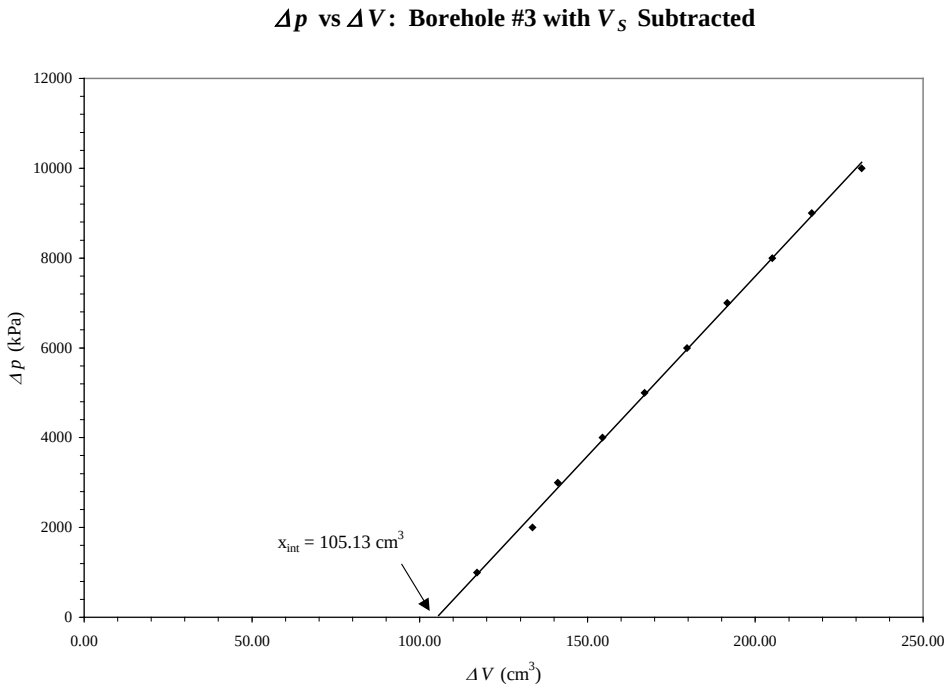

Figure 5-10: Pressuremeter data from borehole #3 with V_S subtracted, and showing the value of the x-intercept.

Table 5-4: Corrected pressuremeter data from borehole #3.

Corrected V_i (cm^3)	**Corrected V_{30} (cm^3)**	**Corrected V_{60} (cm^3)**	**p_i (kPa)**
0.00	0.00	0.00	0
11.25	11.95	12.40	1000
15.06	16.31	16.36	2000
17.66	18.81	18.96	3000
23.30	24.15	24.50	4000
28.78	29.98	30.43	5000
34.62	35.82	36.27	6000
39.98	41.33	41.93	7000
47.18	48.08	48.28	8000
52.57	54.57	55.17	9000
61.56	63.21	63.66	10000

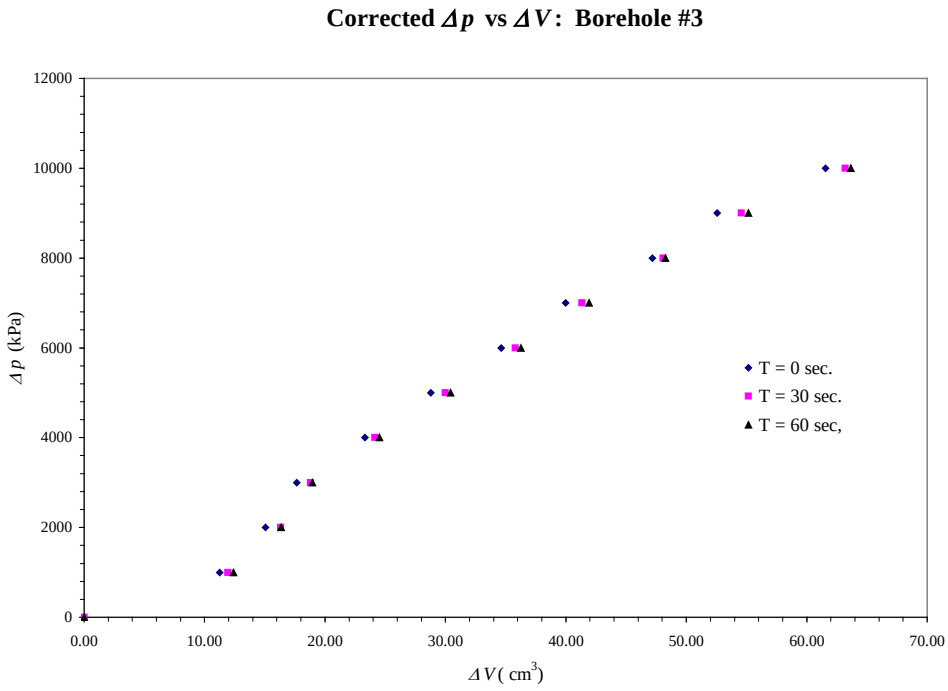

Figure 5-11: Corrected pressuremeter data from borehole #3.

Determination of Young's modulus E

For elastic media, the radial expansion of a cylinder is related to the pressure by the following expression

$$\frac{\Delta R}{R_0} = \frac{(1+\nu)}{E}\Delta p_i \Rightarrow E = (1+\nu)\frac{\Delta p_i R}{\Delta R_0} \qquad (5\text{-}24)$$

where ν is Poisson's ratio. Since the pressuremeter only measures injected fluid volume (ΔV) and resulting pressure (p_i), expression (5-24) must be rewritten. This is done in the following fashion:

$$\frac{V - V_0}{V_0} = \frac{V}{V_0} - 1 = \frac{\pi(R_0 + \Delta R)^2 L}{\pi R_0^2 L} - 1 \qquad (5\text{-}24a)$$

$$\frac{\Delta V}{V_0} = \frac{2\Delta R}{R_0} + 1 - 1 \qquad (5\text{-}24b)$$

Simplification leads to

$$\frac{\Delta R}{R_0} = \frac{\Delta V}{2V_0} \qquad (5\text{-}25)$$

This is possible because L is held fixed, and so the only variable becomes the displacement ΔR. With this in mind, the expression for Young's modulus can be rewritten in the following fashion:

$$E = (1 + \nu) 2V_m \frac{\Delta p_i}{\Delta V} \qquad (5\text{-}26)$$

where Δp_i = change in recorded pressure

ΔV = change in injected fluid

V_m = the sum of the initial volume needed to saturate the probe at rest ($V_{probe} = 790\ cm^3$), and the mean volume injected

Young's modulus was determined by analyzing Δp_i vs ΔV at time zero and plotting the values in Figure 5-12. As shown in Figure 5-12, there is a significant decrease in the slope of the curve at $p_i = 4000\ kPa$ suggesting that the elastic portion of the curve exists between $p_i = 1000\ kPa$ and $p_i = 4000\ kPa$. This decrease in slope is also evident in the results from borehole #4. Throughout testing, there was an inherent problem when changing from the low pressure gage to the high pressure gage on the pressuremeter control panel. This led to the data point at $p_i = 3000\ kPa$, to be shifted

significantly to the left. As a result, $p_i = 3000\ kPa$ is suspect and has been treated as an outlier, and is not used for the calculation of Young's modulus.

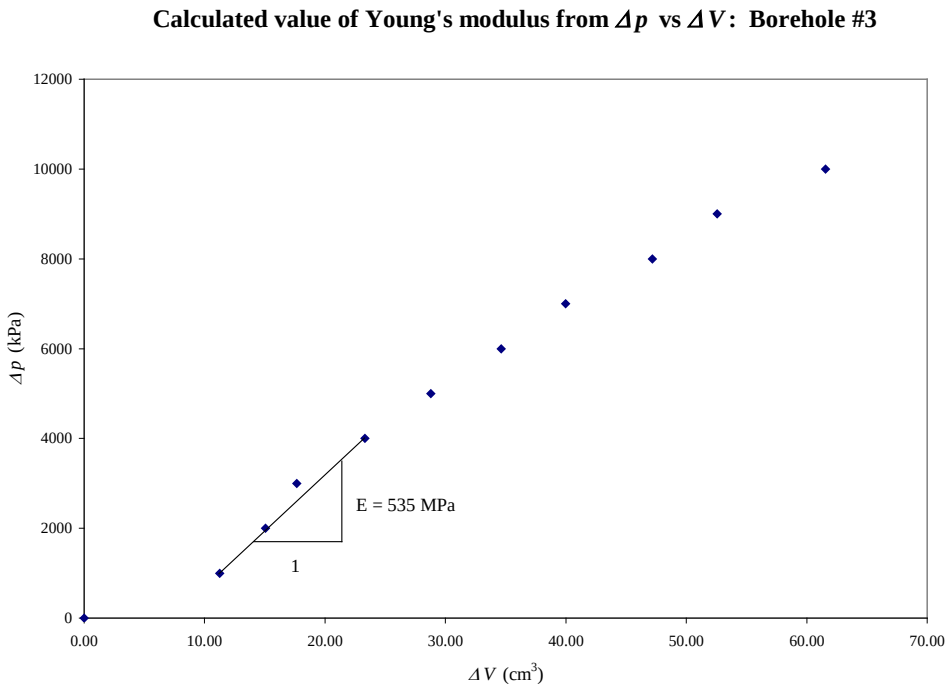

Figure 5-12: Young's Modulus (E), as calculated from the corrected values for Δp vs ΔV from a Menard type pressuremeter test.

The developed expression for Young's modulus was used for both types of pressuremeter tests. All pressuremeter field tests were performed with a ROCTEST Model TEXAM Pressuremeter. Four Menard type pressuremeter tests were performed. Borehole #1 was a low pressure test and so no information concerning Young's modulus is available; borehole #2 was carried out in 18 steps instead of 7 to 14 steps. The test results from borehole #2 show that notable deviation from testing procedures may result in erroneous values for Young's modulus. Boreholes # 3 and #4 were carried out in 10 steps, and these values for Young's modulus are the most reasonable (Table 5-5).

Table 5-5: Calculated values for Young's modulus from Menard type pressuremeter tests in St. Peter sandstone.

Borehole	ν	V_1 **(cm^3)**	V_2 **(cm^3)**	ΔV **(cm^3)**	V **(cm^3)**	p_1 **(kPa)**	p_2 **(kPa)**	Δp **(kPa)**	E **(MPa)**
1	N/A	N/A	N/A	N/A	N/A	N/A	N/A	N/A	N/A
2	0.33	17.61	30.33	12.72	813.97	2000	4000	2000	340.43
3	0.33	11.25	23.30	12.05	807.28	1000	4000	3000	534.61
4	0.33	9.79	18.99	9.20	804.39	1000	4000	3000	697.72

Discounting borehole #2, since this test was not performed within outlined testing guidelines, the average value for Young's modulus was calculated from borehole #3 and borehole #4. The average value ***E = 616 MPa*** is in reasonable agreement with values obtained in laboratory testing.

Two pressuremeter tests using the constant strain method were performed. The constant strain test was designed to be performed in 20 equal volume steps. The test in borehole #5 was done in $\Delta V = 30\ cm^3$ volume steps while the test in borehole #6 was done in $\Delta V = 20\ cm^3$ volume steps.

The raw data is recorded in the following fashion (Table 5-6). Shown in Figure 5-13 is the point at which the bladder ruptured, ending the test. The procedures for correcting the raw data are the same as with the Menard type test (constant stress). For borehole #5, the seating volume was $V_S = 243.00cm^3$, and for borehole #6, the seating volume was $V_S = 458.90\ cm^3$. As with the Menard type test, Young's modulus is calculated in the same fashion using expression (5-26) (Figure 5-14). The values for Young's modulus are shown in Table 5-7.

Table 5-6: Raw data from constant strain test in borehole #5. Injected volume steps were $\Delta V = 30cm^3$.

Injected Volume (cc)	P_i (kPa)	P_{10} (kPa)	P_{20} (kPa)	P_{30} (kPa)
243.00	0	0	0	0
273.20	0	0	0	0
304.60	0	0	0	0
334.80	0	0	0	0
364.50	5	5	5	5
394.20	15	10	10	10
424.60	35	25	25	25
454.50	475	430	410	400
484.20	1100	1020	980	970
511.10	1750	1620	1530	1460
541.10	2375	2125	2035	1950
571.70	3280	200	100	50

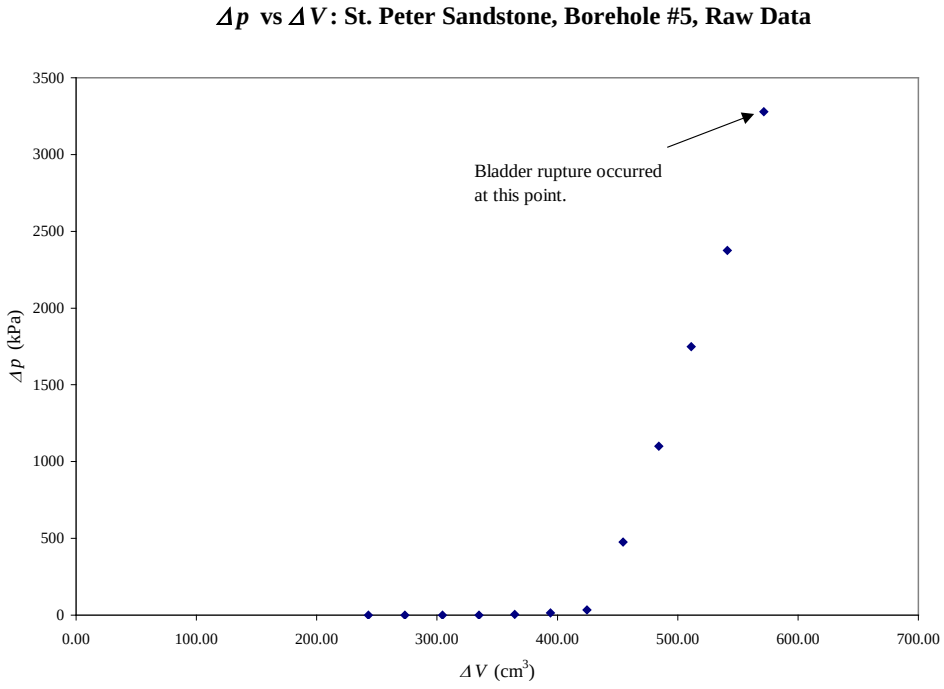

Figure 5-13: Δp vs ΔV of the raw data from a constant strain pressuremeter test where $p \approx 3280kPa$ and $V \approx 571.70cm^3$.

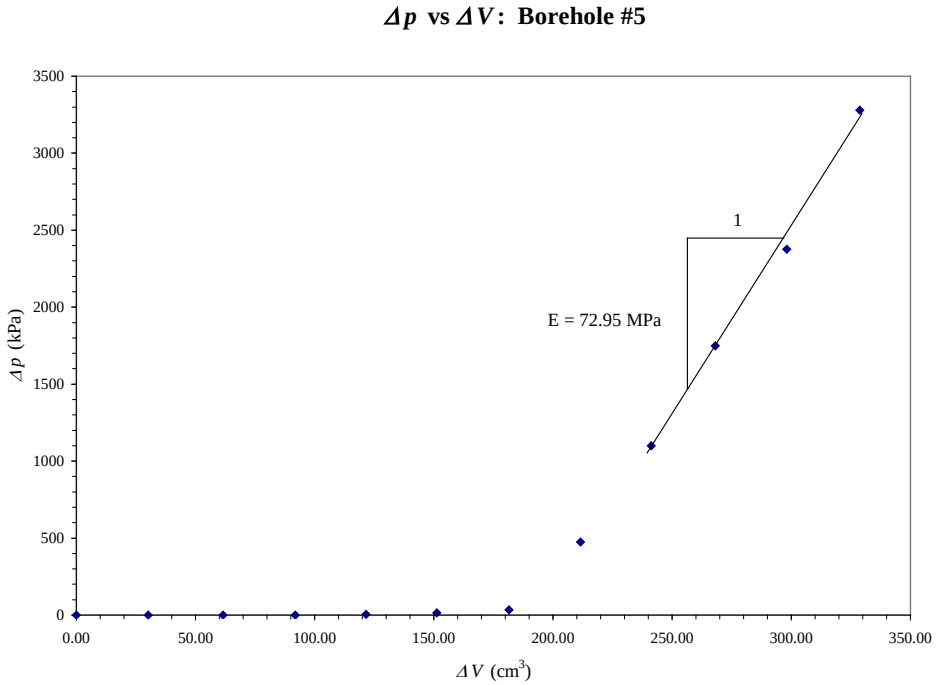

Figure 5-14: Constant strain pressuremeter test results in St. Peter sandstone, borehole #5.

Table 5-7: Constant strain pressuremeter test results.

Borehole	ΔV(cm^3)	ΔP (kPa)	E (MPa)	Volume per step (cm^3)
5	69.16	2180	72.95	30
6	43.83	6800	341.43	20

Table 5-7 shows the results to be abnormally low. What is apparent from the constant strain test results is that there is a correlation between volume of injected fluid and the accuracy of the test results, and the point at which the bladder ruptures. This is possibly due to the design of the probe assembly itself.

Determination of ϕ and δ

The angle of internal friction (ϕ) and the angle of dilation (δ) can also be determined from pressuremeter tests (Hughes et al., 1977). Earlier efforts by Gibson and Anderson (1961) were based on the assumption that the sand behaved elastically up to failure and then continued to fail at a constant ratio of effective stresses (as the stress level increased) and constant volume from the following expression

$$\sigma'_{r_a} = \left(\frac{2\sigma'_{r_0}}{1+N}\right)\left[\left(\frac{E}{2\sigma'_{r_0}(1+\nu)}\right)\left(\frac{1+N}{1-N}\right)\left(\frac{\Delta V}{V}\right)\right]^{(1-N)/2} \qquad (5-27)$$

where σ'_{r_0} is the initial effective lateral stress, E is Young's modulus, ν is Poisson' ratio, and $N = (1-\sin\phi)/(1+\sin\phi)$ which is the ratio of the minor to major principal effective stresses at failure. The flaw in Gibson and Anderson's method is the assumption that the sand deforms at constant volume at failure. It is evident that it is necessary to take into account the dilatant behavior of sands (Figure 5-15) if a reasonable value for ϕ is to be derived (Hughes et al., 1977).

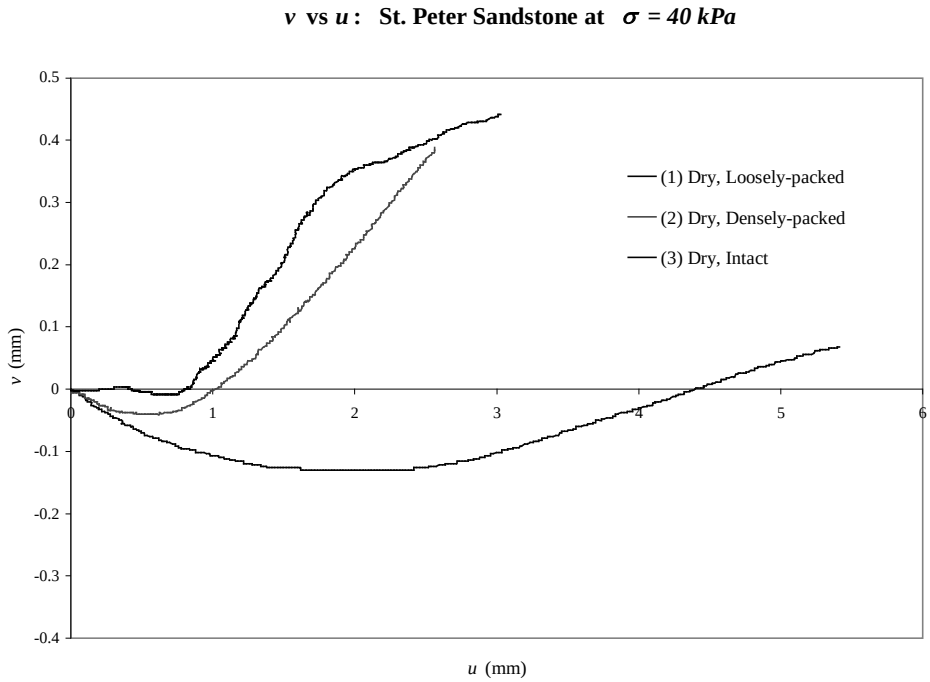

Figure 5-15: *v* versus *u* of St. Peter sandstone showing positive compressive strain.

The expanding pressuremeter is assumed to deform the sandstone under conditions of axial symmetry and plane strain. Because of axial symmetry, the principal stresses acting on an element of the sandstone are σ_{rr}, $\sigma_{\theta\theta}$, σ_{zz} and the strains are given by the expressions

$$\varepsilon_{rr} = -\frac{du_r}{dr} \qquad (5\text{-}28)$$

$$\varepsilon_{\theta\theta} = -\frac{u_r}{r} \qquad (5\text{-}29)$$

$$\varepsilon_{zz} = 0 \qquad (5\text{-}30)$$

where compression is taken as positive.

Inside the failed zone ($a<r<b$), all the sand is assumed to be at the failure stress ratio so that

$$\sigma_{\theta\theta} = N\sigma_{rr} - 2c\sqrt{N} \tag{5-31}$$

where $N = \dfrac{1-\sin\phi}{1+\sin\phi}$ and c = cohesion.

The differential equation of equilibrium must be satisfied:

$$\frac{d\sigma_{rr}}{dr} + \frac{\sigma_{rr} - \sigma_{\theta\theta}}{r} = 0 \tag{5-32}$$

Because pore pressures were not known, total stresses were used. Substituting (5-32) into (5-31) for $\sigma_{\theta\theta}$, and integrating using the boundary condition $\sigma_{rr} = \sigma_{bb}$ at $r = b$, yields

$$\ln\frac{\sigma_{rr}+T}{\sigma_{bb}+T} = (1-N)\ln\frac{b}{r} \tag{5-33}$$

where $T = 2c\dfrac{\sqrt{N}}{1-N}$

Expression (5-33) governs radial distribution of the radial effective stress within the annular zone of failed sand. The sand is also assumed to be failing in such a manner that the ratio of volumetric to shear strains is represented by a straight line. This means the dilation rate is constant and described by

$$\sin\delta = -\frac{u_v}{u_h} = -\frac{\left(\dot{\varepsilon}_{rr} + \dot{\varepsilon}_{\theta\theta}\right)}{\left(\dot{\varepsilon}_{rr} - \dot{\varepsilon}_{\theta\theta}\right)} \tag{5-34}$$

where u_v is normal displacement and u_h is shear displacement, and the dot represents a small increment. As shown by figure 5-14, the y-intercept of the dilation lines is represented by c, which represents a positive compressive strain. In general, it also

indicates that the lines will not necessarily pass through the origin, so the cumulative strains will be related by the expression

$$-\Sigma v = (\Sigma u)\sin\delta - c \qquad (5\text{-}35)$$

Principal strains do not rotate and (5-35) can be rewritten as

$$-\varepsilon_{rr} = n\varepsilon_{\theta\theta} - \frac{c(n+1)}{2} \qquad (5\text{-}36)$$

where $n = \dfrac{1-\sin\delta}{1+\sin\delta} = \text{constant} \quad (0 < n < 1)$

This shows that *n* is directly analogous to *N*.

Substitution for ε_{rr} and $\varepsilon_{\theta\theta}$ in (5-36) from (5-28 and 5-29) yields

$$\frac{du_r}{dr} = -n\frac{u_r}{r} - \frac{c(n+1)}{2} \qquad (5\text{-}37)$$

Expression (5-37) governs the radial distribution of displacement within the annular zone of the failed sand (Hughes et al., 1977).

Multiplying (5-37) by r^n and integrating yields

$$u_r r^n = -\frac{c}{2} r^{n+1} + \text{constant} \qquad (5\text{-}38)$$

By using the boundary condition $r = b$, then

$$u_r r^n = -\frac{c}{2} r^{n+1} + \varepsilon_{rr} b^{n+1} + \frac{c}{2} b^{n+1}$$

Which simplifies to

$$\frac{u_r}{r} = \left(\frac{b}{r}\right)^{n+1}\left(\varepsilon_{bb} + \frac{c}{2}\right) - \frac{c}{2} \qquad (5\text{-}39)$$

Eliminating (*b*/*r*) from (5-33) and (5-39) gives

$$\left(\frac{u_r}{r}+\frac{c}{2}\right)=\left(\varepsilon_{bb}+\frac{c}{2}\right)\left(\frac{b}{r}\right)^{n+1}=\left(\varepsilon_{bb}+\frac{c}{2}\right)\left(\frac{\sigma_{rr}}{\sigma_{bb}}\right)^{(n+1)/(1-N)} \tag{5-40}$$

Expression (5-40) holds throughout the annular zone, and it is especially valid at $r = a$ where the pressuremeter measurements are made:

$$\left(\varepsilon+\frac{c}{2}\right)=\left(\varepsilon_{bb}+\frac{c}{2}\right)\left(\frac{p_i}{\sigma_{bb}}\right)^{(n+1)/(1-N)} \tag{5-41}$$

where $\varepsilon=\dfrac{u_r(r=a)}{a}$ is the strain measured during a pressuremeter test.

Taking the logarithms of both sides yields

$$\log\left(\varepsilon+\frac{c}{2}\right)=\frac{n+1}{1-N}\log p_i+\text{constant} \tag{5-42}$$

This expression predicts a linear relationship by plotting log(p_i) vs log[ε +($c/2$)]. The gradient of this straight line is designated S

$$\frac{1-N}{n+1}=\frac{(1+\sin\delta)\sin\phi}{1+\sin\phi}=S \tag{5-43}$$

Determining ϕ requires that the pressuremeter data be converted from Δp vs ΔV to σ_{rr} vs $\varepsilon_{\theta\theta}$. This is done by first calculating the volumetric strain. From the values of volumetric strain and using expression (5-25), the radial expansion of the borehole can be calculated. Using the values for radial expansion, strain ($\varepsilon_{\theta\theta}$) can be calculated (Table 5-8). Once radial strain is calculated, the data were graphed (Figure 5-16).

Table 5-8: Values necessary to calculate ϕ from pressuremeter tests.

(a) Borehole #3

Volumetric Strain (e)	u_r (cm)	Radial Strain (ε)	Pressure (kPa)
0.000	0.000	0.000	0
0.005	0.010	0.003	1000
0.007	0.014	0.004	2000
0.008	0.016	0.004	3000
0.011	0.021	0.005	4000
0.013	0.026	0.007	5000
0.016	0.031	0.008	6000
0.019	0.036	0.009	7000
0.022	0.042	0.011	8000
0.024	0.047	0.012	9000
0.029	0.055	0.014	10000

(b) Borehole #4

Volumetric Strain (e)	u_r (cm)	Radial Strain (ε)	Pressure (kPa)
0.000	0.000	0.000	0
0.005	0.009	0.002	1000
0.006	0.012	0.003	2000
0.007	0.013	0.003	3000
0.009	0.017	0.004	4000
0.011	0.021	0.005	5000
0.013	0.025	0.007	6000
0.016	0.030	0.008	7000
0.018	0.034	0.009	8000
0.020	0.039	0.010	9000
0.023	0.045	0.012	10000

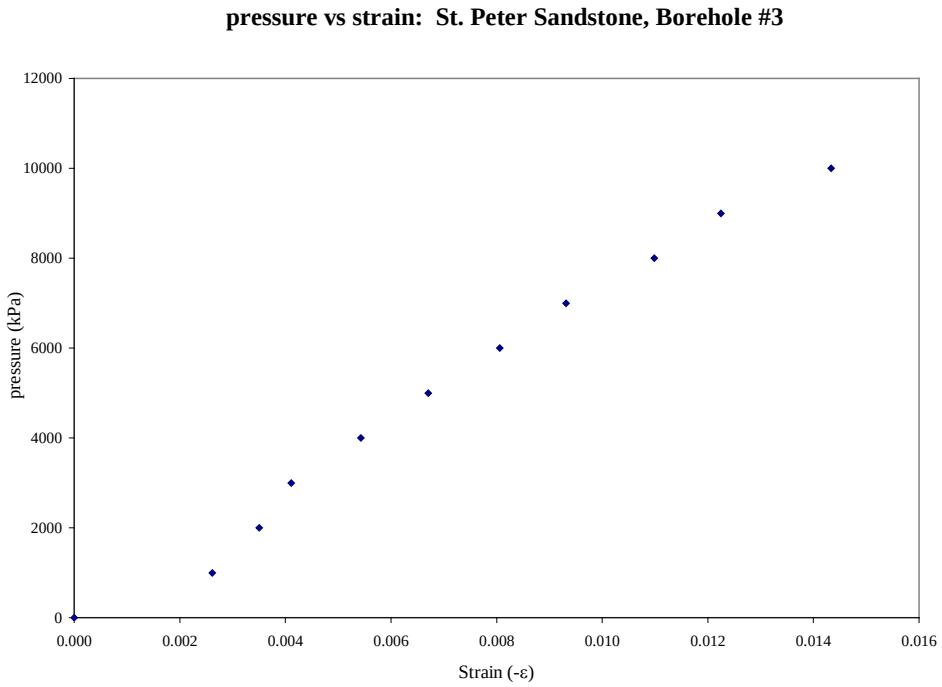

(a) Borehole #3

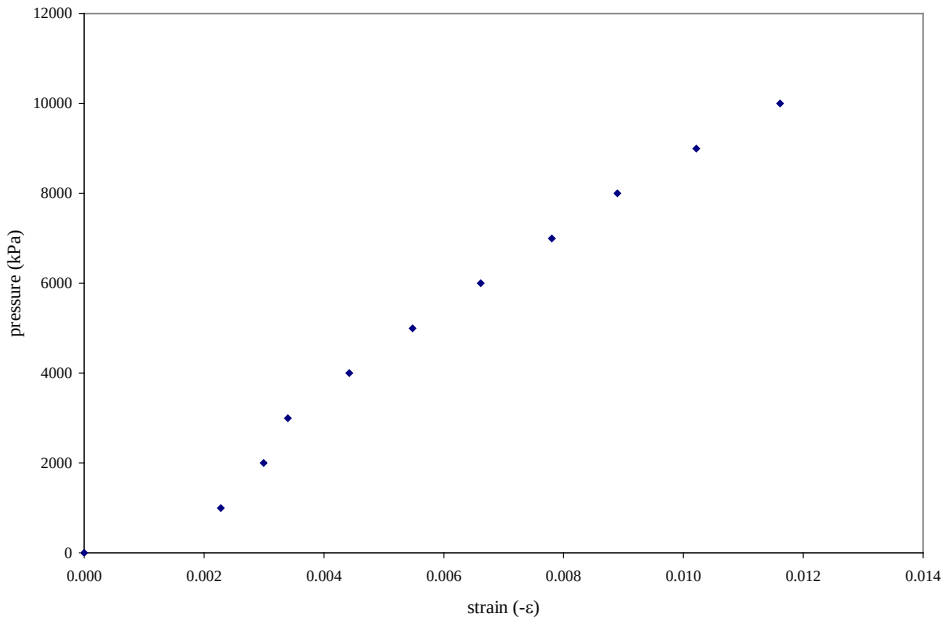

(b) Borehole #4

Figure 5-16: Pressure vs strain graphs for boreholes #3 and #4.

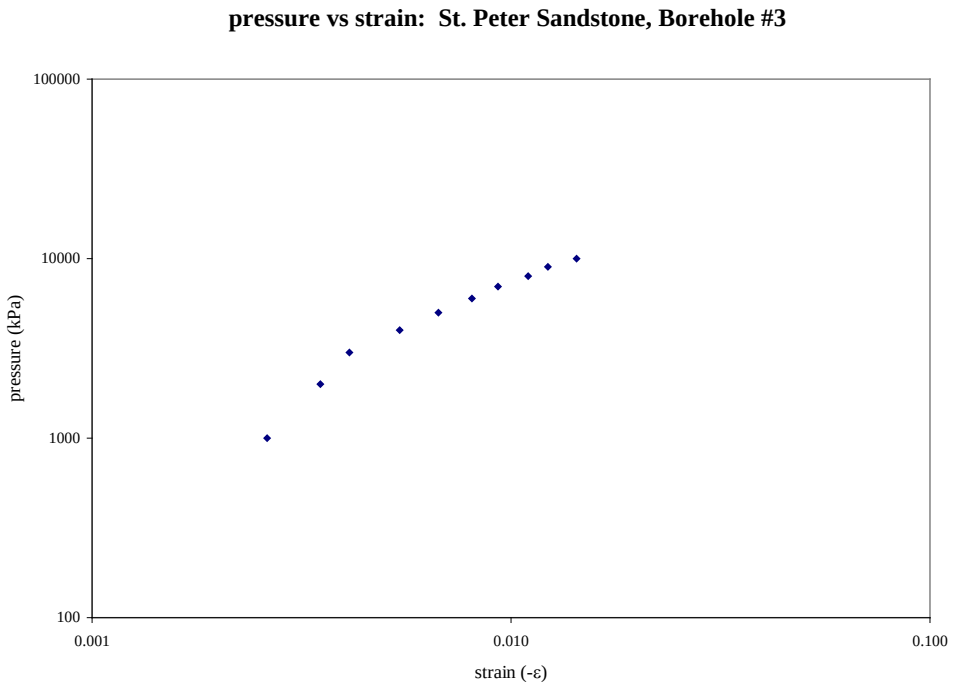

(a) Borehole #3

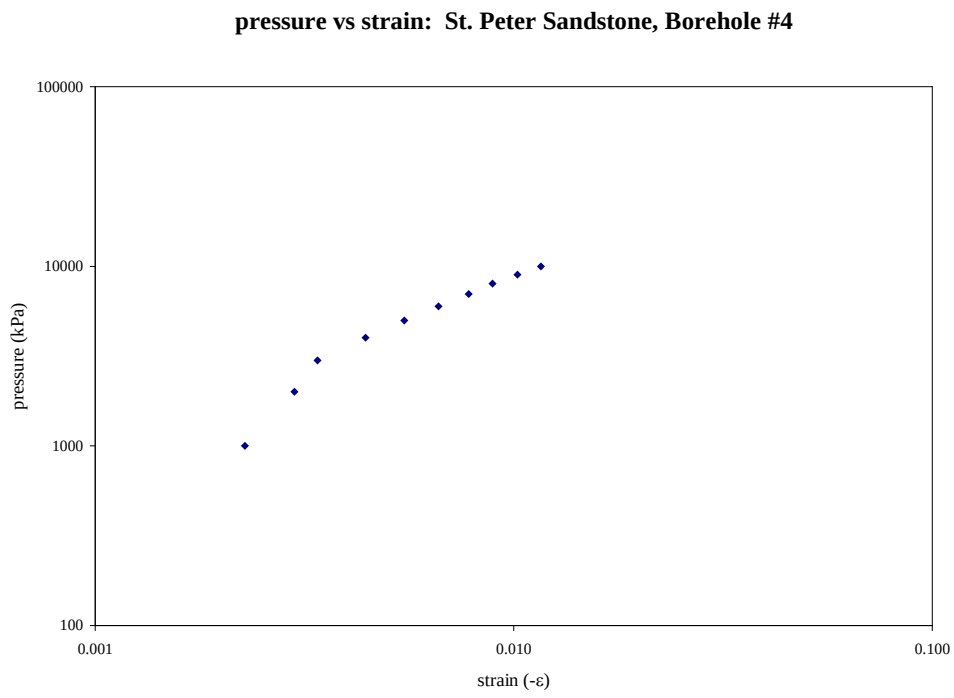

(b) Borehole #4

Figure 5-17: Pressure vs strain for boreholes #3 and #4 in log-log axes.

Once the data have been converted, the next step was to change the axes to log-log scales (Figure 5-17).

The angle of dilation is taken as a range of values between

$\delta = 0$

$\delta \leq \phi$

This results in expression (5-43) becoming

$$S = \frac{\sin\phi}{1+\sin\phi} \quad \text{at} \quad \delta = 0 \qquad (3\text{-}43a)$$

and

$$S = \frac{\sin\phi + \sin^2\phi}{1+\sin\phi} \quad \text{at} \quad \delta = \phi \qquad (3\text{-}43b)$$

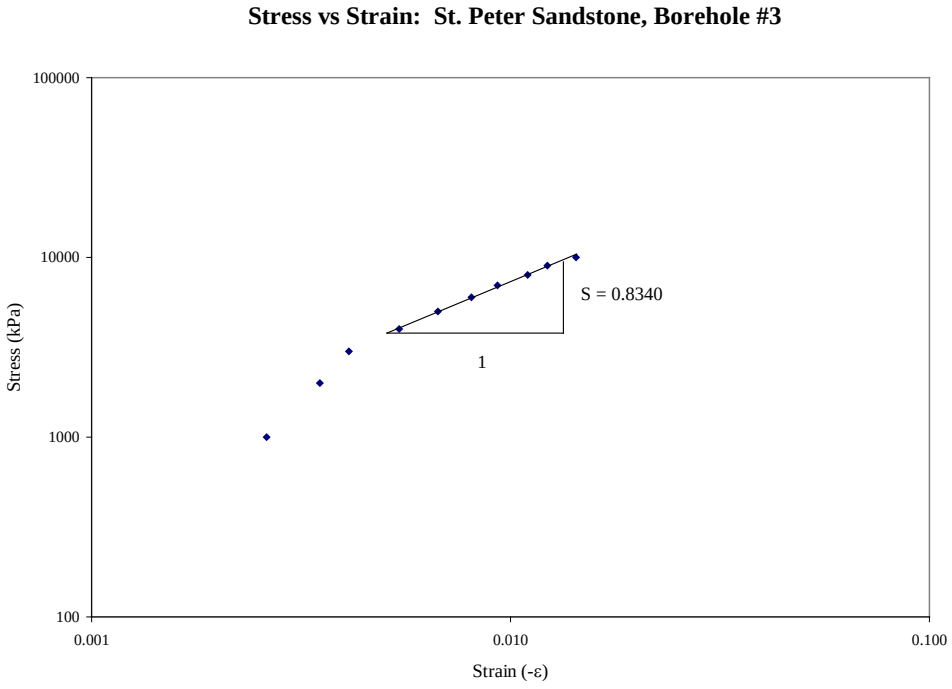

(a) Borehole #3

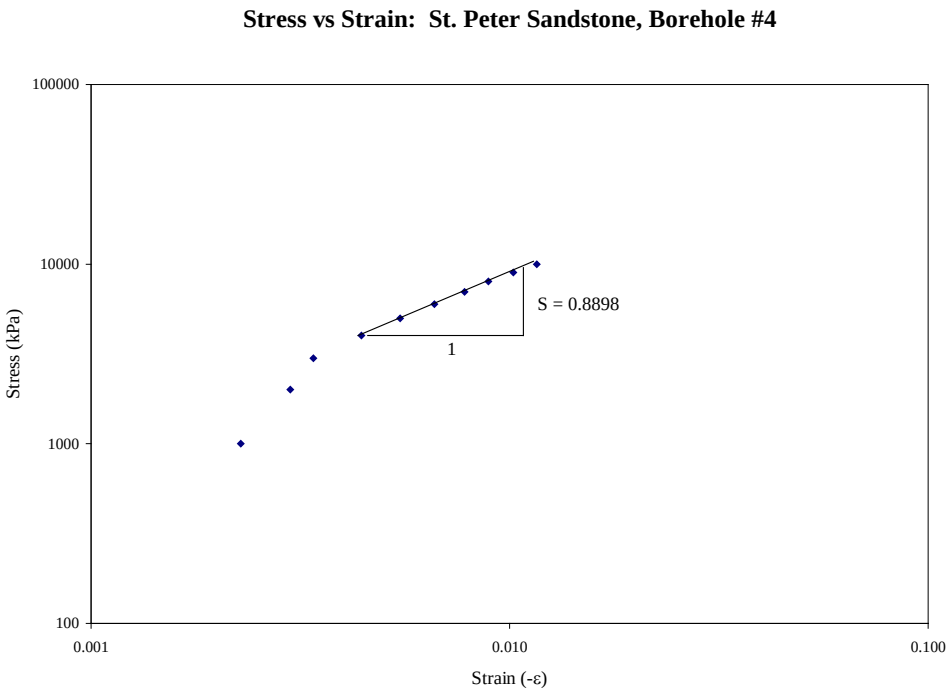

(b) Borehole #4

Figure 5-18: Graphically determined values for *S* from boreholes #3 and #4.

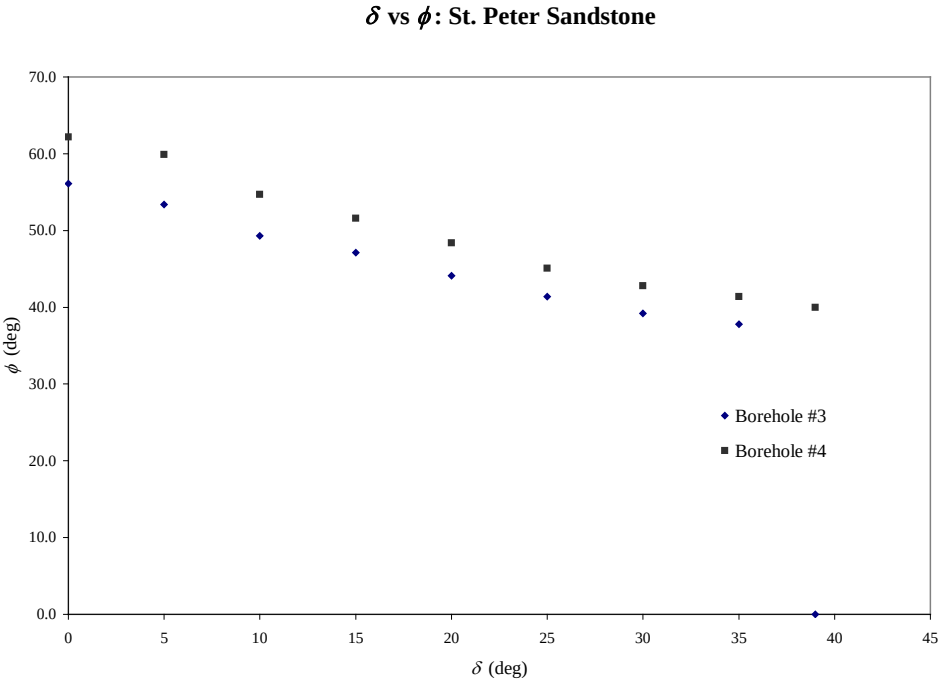

Figure 5-19: ϕ vs δ for borehole #3 and borehole #4.

The value for *S* can be determined graphically (Figure 5-18). With the value of *S* and a range of selected values for δ, a range of values for ϕ can be calculated (Table 5-9). With these values, δ vs ϕ can be plotted (Figure 5-19).

Table 5-9: Values for ϕ based on assumed values of δ and graphically determined values of *S*.

δ (deg)	**ϕ (deg) Borehole #3 (S = 0.8340)**	**ϕ (deg) Borehole #4 (S = 0.8898)**
0	56.1	62.2
5	53.4	59.9
10	49.3	54.7
15	47.1	51.6
20	44.1	48.4
25	41.4	45.1
30	39.2	42.8
35	37.8	41.4
39	N/A	40.0

Several things concerning pressuremeter testing should be noted here. Since effective stresses were not known, the estimated friction angles were associated with total stresses. Pore suction (the sandstone was wet) and borehole disturbance influenced the pressuremeter tests. In all likelihood, the action of drilling the borehole left a zone of disturbance, and combined with the small strain levels (<1% with failure), the zone of disturbance may have influenced the test results. Even though wetting sandstone samples caused them to lose their structure, there may have been some small amount of cohesion that wasn't taken into account, also the elastic behavior of the soft rock was not taken into account. All these assumptions may have contributed to the dilatancy angles that were overestimated.

Shear Modulus G

The pressuremeter test was designed to directly calculate the shear modulus of a geo-material by using the expression

$$G = \frac{\Delta p_i V_M}{\Delta V} \tag{5-44}$$

By substituting expression (5-44) into

$$G = \frac{E}{2(1+\nu)} \tag{5-45}$$

the expression for Young's modulus, expression 5-26, is arrived at.

Using the results from the two Menard type tests and expression 5-44, the shear modulus of the St. Peter sandstone can be calculated. For borehole #3, *G = 201MPa*, and borehole #4, *G = 262MPa*.

CONCLUSIONS

The St. Peter sandstone is a unique formation that is remarkably uniform in mineralogical composition and thickness. Engineering methods of classification identify St. Peter sand as poorly-graded, medium to fine-grained, well rounded to angular, rust to white sand with little fines. The unit has been, and is sometimes, described as a locked sand rather than a sandstone. This classification is based on the identification of locked sand grains, the existence of post-depositional quartz overgrowths, and very little cementing material. Mechanical elements of locked sands include a large dilation angle, a larger friction angle than densely-packed sands, and a nonlinear failure envelope. These characteristics presented themselves during direct shear tests, where under low normal stress (20 kPa), a dilation angle of 14^o and a friction angles from 42^o - 50^o were recorded.

Under saturated conditions, direct shear results deviated strongly from test results under dry conditions. It is possible to explain this deviation by considering the clay fraction in the St. Peter sandstone. Examination of free sand grains under scanning electron microscopy (SEM) showed a considerable amount of clay minerals and iron-oxides attached to the sand grains as flakes and laminae. In addition, under SEM, there was evidence that grain contact boundaries were encased in a rime of minerals that have elements of clay, iron-oxides and quartz. Whether these rime minerals are the parent minerals or a precipitate of a different composition is unknown. Under saturated conditions, these impurities and rime minerals may breakdown and reduce the cohesion and friction between sand grains.

Uniaxial compression testing of dry, intact specimens yielded a uniaxial strength of 1 MPa, and a Young's modulus of 1 GPa, which are comparable to an over-consolidated soil.

Field testing was done using a pressuremeter. It is essential to take system stiffness into account when analyzing the pressurementer data. Testing was performed above the water table at a depth of 1 - 2 meters resulting in the tests being performed in wet but not saturated material. Analysis of the pressuremeter data resulted in a Young's Modulus of about 0.5 GPa, which is lower than laboratory results. These lower values may be the result of sample disturbance at small strain levels. Friction angles were consistent with laboratory results but dilatancy angles, calculated from field tests, were overestimated. Effective stresses were not known, so test data was analyzed using total stresses that resulted in the elasticity of the material and small amounts of cohesion not being accounted for.

BIBLIOGRAPHY

Amaral, E.J. and Pryor, W.A., 1977, Depositional Environment of the St. Peter Sandstone Deduced by Textural Analysis, Journal of Sedimentary petrology, v. 47, no. 1, p. 32-52.

Craig, R.F., 1996, Soil Mechanics, Chapman & Hall, Publishers, 427 pages.

Crook, Keith, A.W., 1968, Weathering and roundness of quartz sand grains, Sedimentology, v. 11, p. 171-182.

Dally, James W., and Riley, William F., 1991, Experimental Stress Analysis, McGraw-Hill, Inc., Publishers, 639 pages.

Dake, C.L., 1921, The Problem of the St. Peter Sandstone, Bulletin Missouri University School of Mines and Metallurgy, Technical Series, Vol. 6, 225 pages.

Dapples, E.C., 1955, General Lithofacies Relationship of St. Peter Sandstone and Simpson Group, Bulletin of the American Association of Petroleum Geologists, Vol. 39, No. 4, p. 444-467.

Dott, R.H. Jr., and Roshardt, M.A., 1972, Analysis of Cross-Stratification Orientation in the St. Peter Sandstone in Southwestern Wisconsin, Geological Society of America Bulletin, Vol. 83, p. 2589-2596.

Dusseault, M. B., and Morgenstern, N. R., 1979, Locked sands, Quarterly Journal of Engineering Geology, Vol. 12, p. 117-131.

Fraser, Gordon, S., 1976, Sedimentology of a Middle Ordovician quartz arenite-carbonate transition in the Upper Mississippi Valley, Geological Society of America Bulletin, Vol. 86, p. 833-845.

Fukagawa, R., Muro, T., Hata, K., and Hino, N., 1998, A new method to estimate the angle of internal friction of sand using a pressuremeter test, Geotechnical Site Characterization, ISC ’98, Vol. 2, p. 771-775.

Gibson, R. E., and Anderson, W. F., 1961, In Situ Measurement of Soil Properties with the Pressuremeter, Civil Engineering and Public Works Review, Vol. 56, No. 658, p. 615-618.

Heinrich, E. WM., 1981, Geologic types of glass-sand deposits and some North American representatives, Geological Society of America Bulletin, Part I, Vol. 92, p. 611-613.

Hughes, J. M. O., Wroth, C. P., and Windle, D., 1977, Pressuremeter tests in sands, *Geotechnique*, 27, No. 4, p. 455-477.

James, Joseph Francis, 1894, The St. Peter's Sandstone, The Cincinnati Society of Natural History Journal, vol. 17, p. 115-135.

Labuz, J.F., Zietlow, W.K., and Chen, L.H., 1996, Laboratory Testing for the Minnesota Library Access Center, Unpublished Report Submitted to CNA Consulting Engineers, 25 pages.

Mazzullo, J.M., Ehrlich, Robert, 1980, A Vertical Pattern of Variation in the St. Peter Sandstone-Fourier Grain Shape Analysis, Journal of Sedimentary Petrology, Vol. 50, No. 1, p. 53-70.

--1983, Grain-Shape Variation in the St. Peter Sandstone: A Record of Eolian and Fluvial Sedimentation of an Early Paleozoic Cratonic Sheet Sand, Journal of Sedimentary Petrology, Vol. 53, No. 1, p. 105-119.

--1987, The St. Peter Sandstone of southeastern Minnesota; mode of deposition, Middle and Late Ordovician lithostratigraphy and biostratigraphy of the Upper Mississippi Valley, Robert E. Sloan ed., Report of Investigations-Minnesota Geological Survey, Vol. 35, p. 44-50.

Olsen, Bruce Michael, 1976, Stratigraphic Occurrence of Argillaceous Beds in the St. Peter Sandstone, Twin City Basin, Unpublished Master's Thesis, University of Minnesota, 89 pages.

Palmer, A.C., 1972, Undrained Plane-Strain Expansion of a Cylindrical Cavity in Clay: A Simple Interpretation of the Pressuremeter Test, Geotechnique 22, No. 3, p. 431-457.

Parham, Walter E., 1970, Petrography of St. Peter sandstone, Minnesota Geological Survey Information Circular, v. 8, p. 10.

Payne, Charles Marshall, 1967, Engineering aspects of the St. Peter sandstone in the Minneapolis-St. Paul are of Minnesota, Unpublished Master's Thesis, University of Arizona, 126 pages.

Peterson, David Lee, 1978, Estimating the Strength of St. Peter Sandstone Pillars, Unpublished Master's Thesis, University of Minnesota, 159 pages.

Pittman, Edward, D., 1972, Diagenesis of quartz in sandstones as revealed by Scanning Electron Microscopy, Journal of Sedimentary Petrology, Vol. 42, No. 3, p. 507-519.
Pryor, Wayne, A., and Amaral, Eugene, J., 1971, Large-Scale Cross-Stratification in the St. Peter Sandstone, Geological Society of America Bulletin, Vol. 82, p.239-244.

Potter, P.E. and Pryor, W.A., 1961, Dispersal centers of Paleozoic and later clastics of the Upper Mississippi valley and adjacent area, Geological Society of America Bulletin, v. 72, p. 1195-1250.

Pryor, W.A. and Amaral, E.J., 1971, Large-Scale Cross-Stratification in the St. Peter Sandstone, Geological Society of America Bulletin, v. 82, p. 239-244.

Sardeson, F.W., 1896, The Saint Peter sandstone, Minnesota Academy of Natural Sciences, Vol. 4, Paper D, p. 64-88.

--1932, The Saint Peter Group of Minnesota, Pan American Geology, Vol. 58, No. 3, p. 191-196.

Schwartz, George, M., 1936, The geology of the Minneapolis-St. Paul metropolitan area, Minnesota Geological Survey bulletin 27.

--1939, Final report of foundation conditions at the sites of the proposed St. Anthony Falls locks Minneapolis, Minnesota, U.S. Army corps of Engineers, St. Paul District.

--1961, Origin and characteristics of the St. Peter sandstone, Minnesota Engineer, v. 11, no. 5, p. 12-13.

Thiel, G.A., 1935, Sedimentary and Petrographic Analysis of the St. Peter Sandstone, Bulletin of the Geological Society of America, Vol. 46, p. 559-614.

U.S. Army Corps of Engineers, St. Paul District, 1939, Permeability Tests on St. Peter Sandstone Specimens, 43 pages.

--1952, Report of Field Bearing Tests on St. Peter Sandstone Using Different Size Bearing Plates, 22 pages.

--1958, Design Memorandum No.3 Upper Lock, Part UL-3 Foundations and Geology, St. Paul District final report.

Watson, John D., 1938, Triaxial Compression Tests on St. Peter Sandstone, Unpublished report to the U.S. Army Corps of Engineers, St. Paul District, 44 pages.

Windle, D., and Wroth, C. P., 1977, The use of a self-boring pressuremeter to determine the undrained properties of clays, Ground Engineering, Sept. 1977, p. 37-46.

Wroth, C.P., 1984, The Interpretation of In Situ Soil Tests, Geotechnique 34, No. 4, 449-489.

APPENDICES

Appendix A: Filling and Saturating the Instrument

1) Connect two lengths of flexible tubing to quick connects 4 and 5.
2) Set valve no. 8 on FILL and valve no. 9 on TEST.
3) Raise the cylinder to its uppermost position. This corresponds to 1732.00 cm^3 on the volume counter.
4) Place the free ends of the flexible tubing into a reservoir of clean water or appropriate antifreeze mixture. Make sure the tube ends stay submerged to prevent the introduction of air in the reservoir.
5) Lower the piston by turning the crankhandle at approximately 45 rpm.
6) When the volume counter reads 0.00 cm^3, stop turning and allow the system to sit for one minute so the suction can stop.
7) Incline the unit slightly forward (toward the operator) and crank the handle 16 revolutions (192.00 cm^3) on the counter to evacuate air trapped in the cylinder. Repeat this step until the fluid flowing through the tubing is bubble free.
8) Return the instrument to the vertical and turn the crank to 0.00cm^3 and allow the system to sit for 30 seconds.

Appendix B: Saturating the Pressure Gauges

1) Hook up short tube with a male quick disconnect to port no. 1; the water outlet to the probe.
2) Place valve no. 8 on TEST with GAUGE no. 6. Raise the piston by cranking the handle 8 revolutions (96.00cm^3 on the counter). Ensure the water flowing out of the tubing does not contain any air bubbles.
3) Disconnect the tube from port no. 1.
4) Place valve no. 8 on TEST with GAUGE no. 6 and valve no. 9 on GAUGE no. 6.
5) Raise the piston by turning 8 revolutions (192.00cm^3 on the counter).
6) Place valve no. 8 on TEST with GAUGE no. 7 and valve no. 9 on GAUGE no. 7 and raise the piston 8 revolutions (288.00cm^3 on the counter).
7) Place valve no. 9 on TEST.
8) Place valve no. 8 on TEST with GAUGE no. 3.
9) Hook up short tubing with quick disconnect on port no. 3, and raise the piston by turning the crank 8 revolutions (380.00 cm^3 on the counter).
10) Disconnect the tubing from port no. 3.
11) Place valve no. 8 on FILL. Return the piston to its lowermost position (0.00cm^3 on the counter) and wait one minute.
12) Repeat steps 7 and 8.

Appendix C: Saturation Check

1) Place valve no. 8 on TEST with GAUGE no. 6 and valve no. 9 on TEST.
2) Install the large crank handle on the rear section of the actuator.
3) With the indicator reading zero, apply 2500 kPa to pressure gauge no. 6 and no. 7 by rotating the large crank handle. Read the counter.
   If the counter reads more than $0.18cm^3$, the instrument is not completely saturated. Return to step 7 of ***Saturating the Pressure Gauges*** and continue to step 3 of the ***Saturation Check*** until the instrument is fully saturated.

Appendix D: Saturating the Tubing Probe Assembly

1) Connect the probe line to port no. 1 on the control instrument.
2) Remove the plug at the lower end of the probe. Slightly incline the probe and make sure the saturation tubing is at the twelve-o'clock position.
3) Inject water into the probe until only air free water is flowing out. Valve no. 8 is on TEST with GAUGE no. 6 and valve no. 9 is on TEST.
4) Hold the probe at the same elevation as the control system gauges and allow water to run out until the probe returns to its original diameter. Replace the saturation-tubing plug and tighten.
5) Disconnect the tubing from port no. 1. Refill the cylinder by placing valve no. 8 on FILL and returning the piston to its lowermost position. Wait one minute.
6) Disconnect the flexible tubing from port no. 4 and no. 5.

Appendix E: Dittes, M., Labuz, J.F., 2002, Field and Laboratory Testing of St. Peter Sandstone, Journal of Geotechnical and Geoenvironmental Engineering, Vol. 128, No. 5, May 1, p. 372-380.

Dittes, Michael

From: PERMISSIONS <permissions@asce.org>
Sent: Tuesday, December 01, 2015 10:14 AM
To: Dittes, Michael; PERMISSIONS
Subject: RE: Thesis publication

Dear Michael E. Dittes,

The information from RightsLink must fit all types of request.

Permission is granted for you to reuse you ASCE paper for your thesis. A full credit line must be added to the material. For reuse in non-ASCE publications, add the words "With permission from ASCE" to your source citation. For Intranet posting, add the following additional notice: "This material may be downloaded for personal use only. Any other use requires prior permission of the American Society of Civil Engineers."
Regards,

Joann

Joann Fogleson
Manager, Product and Subscription Services
American Society of Civil Engineers
1801 Alexander Bell Drive
Reston, VA 20191

PERMISSIONS@asce.org

703-295-6112

E-mail: jfogleson@asce.org
Internet: www.asce.org/pubs | www.ascelibrary.org | http://ascelibrary.org/page/rightsrequests

A full credit line must be added to the material being reprinted. For reuse in non-ASCE publications, add the words "With permission from ASCE" to your source citation. For Intranet posting, add the following additional notice: "This material may be downloaded for personal use only. Any other use requires prior permission of the American Society of Civil Engineers."

Each license is unique, covering only the terms and conditions specified in it. Even if you have obtained a license for certain ASCE copyrighted content, you will need to obtain another license if you plan to reuse that content outside the terms of the existing license. For example: If you already have a license to reuse a figure in a journal, you still need a new license to use the same figure in a magazine. You need separate license for each edition

Field and Laboratory Testing of St. Peter Sandstone

M. Dittes, A.M.ASCE,[1] and J. F. Labuz, M.ASCE[2]

Abstract: The purpose of this project was to evaluate mechanical properties of St. Peter sandstone by in situ testing, and to compare the field data with laboratory results. Direct shear tests were conducted to evaluate the strength-dilatancy behavior, and thin-section microscopy was used to help explain the significant friction angles associated with the material. St. Peter sandstone is nearly cohesionless, but it possesses a friction angle of 57–63° at low confinement. The large angle of internal friction at failure may be due to locking of sand particles or to postdepositional quartz overgrowths. Tests on pulverized densely packed sand and loosely packed sand were conducted in the same manner as the intact specimens and yielded friction angles of about 42 and 34°. Pressuremeter tests were performed in situ and the results were interpreted using an elasto-plastic analysis in terms of total stresses. By appropriate consideration of system stiffness, Young's modulus was found to be about 0.5 GPa, slightly lower than the laboratory value, although unload-reload cycles were not attempted. Assuming associative behavior, the friction angle was estimated to be at least 56°.

DOI: 10.1061/(ASCE)1090-0241(2002)128:5(372)

CE Database keywords: Laboratory tests; Dilatancy; Shear tests; Sand; Rocks.

Introduction

St. Peter sandstone is an arenaceous, ortho-quartzitic, sublittoral cratonic sheet sand of middle Ordovician age. It is remarkable in geographic coverage, mineralogical composition, and thickness. For a vast majority of its extent it is buried; only in the upper Mississippi River valley is it readily exposed. St. Peter sandstone has been excavated for tunnels and foundations in the Minneapolis-St. Paul area for decades. The earliest test results were for these endeavors (Watson 1938; Schwartz 1939). As the interest in the design of underground space has grown, the need for providing material properties of St. Peter sandstone has changed to meet that need.

As shown by the results from triaxial testing [Fig. 1(a)], St. Peter sandstone is nearly cohesionless yet it fails at friction angles of 59–69° at low confinement, with an average value of approximately 63° (Watson 1938; Means and Parcher 1963). Triaxial tests on pulverized densely packed [Fig. 1(b)] and loosely packed [Fig. 1(c)] sand specimens have been performed in the same manner as the intact specimens (Watson 1938), and yielded friction angles of 42 and 33° [Fig. 1(b)]. When dry intact specimens are subjected to unconfined compression, St. Peter sandstone exhibits values of strength, approximately 1 MPa, and Young's modulus, approximately 1 GPa, associated with a heavily overconsolidated soil, but sampling the material poses significant difficulty (Payne 1967; Petersen 1978).

[1]Research Assistant, Dept. of Civil Engineering, Univ. of Minnesota, Minneapolis, MN 55455.

[2]Associate Professor, Dept. of Civil Engineering, Univ. of Minnesota, Minneapolis, MN 55455. E-mail: jlabuz@tc.umn.edu

Note. Discussion open until October 1, 2002. Separate discussions must be submitted for individual papers. To extend the closing date by one month, a written request must be filed with the ASCE Managing Editor. The manuscript for this paper was submitted for review and possible publication on June 21, 2000; approved on October 11, 2001. This paper is part of the ***Journal of Geotechnical and Geoenvironmental Engineering***, Vol. 128, No. 5, May 1, 2002. ©ASCE, ISSN 1090-0241/2002/5-372–380/$8.00+$.50 per page.

Analysis of St. Peter sandstone in particular and weak rock in general under in situ conditions seem to be lacking, as conventional hard rock techniques are not appropriate, while soil-testing apparatus may need modifications. Recorded field studies of St. Peter sandstone have been limited to plate bearing tests for foundation design (U.S. Army Corps of Engineers 1939). The purpose of this project was to evaluate mechanical properties of St. Peter sandstone by in situ testing, and then to compare the field data was laboratory results. Direct shear tests were conducted to evaluate the strength-dilatancy behavior, and microscopy analysis was used to help explain the significant friction angles associated with the material. Pressuremeter tests were performed and the results were interpreted using an elasto-plastic analysis. By appropriate consideration of system stiffness, modulus and friction angle were found to approximately match those measured in the laboratory.

Geology

Captain Jonathan Carver, while exploring the interior of the continent in 1766–1768, provided the initial description of St. Peter sandstone. Carver wrote about a cave in sandstone that was so soft he could cut the rock with his knife. Major Stephen H. Long, in 1817, described St. Peter sandstone as a whitish-yellowish material that could be called a sand rather than sandstone. Dr. D. D. Owen, in a paper in 1847, described the geologic formation by name for the first time. He called it St. Peter's sandstone for the excellent exposures found below Fort Snelling at the mouth of the St. Peter's River. With the St. Peter's River renamed the Minnesota River, the name St. Peter's sandstone was eventually amended to St. Peter sandstone (Sardeson 1896).

St. Peter sandstone is a cratonic sheet sand that covers more than 576,000 km^2 of middle North America. Most of this arenaceous terrain is subsurface (Thiel 1935; Amaral and Pryor 1977; Mazzullo and Ehrlich 1988). Early efforts to map St. Peter sandstone were limited to exposures in southeastern Minnesota, northeastern Iowa, the southern third of Wisconsin, and northern Illinois (Sardeson 1896). The most likely source material comes from pre-Croixian sandstone of the Laurentian Shield (Thiel

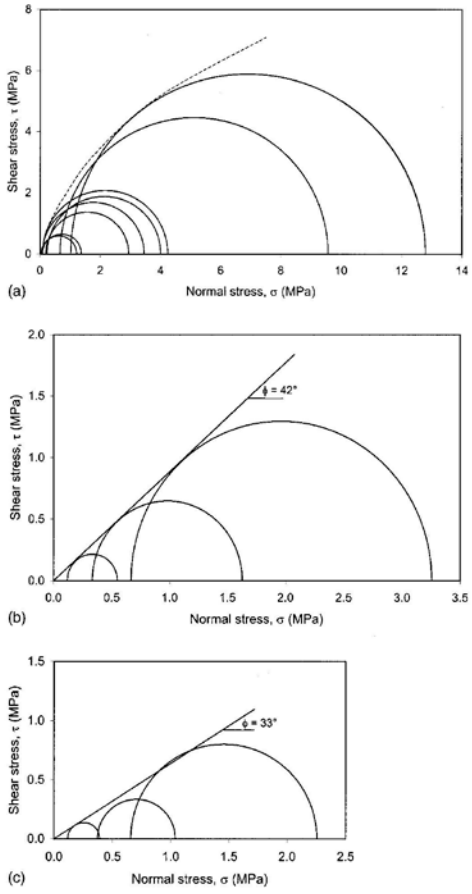

Fig. 1. Failure envelopes of St. Peter sandstone: (a) intact, (b) recompacted dense (Watson 1938), and (c) recompacted loose

1935). North of Minneapolis-St. Paul, St. Peter sandstone pinches out in heavily torn and glaciated terrain. The formation dips to the south and is identified through borehole cuttings. St. Peter sandstone was originally considered to be limited in distribution to the Upper Mississippi Valley (Minnesota, Wisconsin, Iowa, Illinois, and Missouri). It is now recognized that St. Peter sandstone probably existed into Canada at the time of deposition, extended as far south and west as Nebraska, South Dakota, Kansas, Arkansas, and Tennessee, and extended eastward into Michigan, Ohio, and northeastern Kentucky.

St. Peter sandstone is Middle Ordovician in age, and in southern Minnesota, southwestern Wisconsin, and Iowa unconformably overlies the Shakopee dolomite of the Lower Ordovician Prairie du Chien group. St. Peter sandstone itself is composed of two members. The lower unit is the Tonti member, which is a fine-grained quartz arenite with a thin basal unit that contains cross-bedded sandstone, green silty shales, and brecciated limestone and cherty nodules. The upper unit is the Starved Rock member, a medium-grained quartz arenite that grades conformably into the Glenwood formation. Separating the two members is an unnamed band. Originally described as a shale band, it was classified by drill cuttings as a marl-rock zone (Sardeson 1932) and later reclassified as a slit bed that varies in thickness from approximately 1.5 to 9 m (Thiel 1935; Schwartz 1939). The upper contact is a conformable transition crossing three formations, marking a lithologic change from quartz arenites of the St. Peter sandstone to sandy shale, shale, and calcareous shale of the Glenwood formation to shallow water carbonates of the Platteville limestone (Schwartz 1939; Fraser 1976).

St. Peter sandstone varies in thickness from tenths of meters in eastern Wisconsin to greater than 150 m at Joliet, Ill. (Thiel 1935). Throughout its distribution, St. Peter sandstone averages 30 m in thickness. In the Twin Cities basin, measurements from 57 wells have resulted in an average thickness of 48 m. Lateral variations in thickness are extreme, and St. Peter sandstone may vary in thickness by 30 m in as little as 0.4 km (Thiel 1935).

St. Peter sandstone has a silica (SiO_2) content that is approximately 99% on average. The SiO_2 is in the form of clear limpid grains of quartz. The sandstone is extremely friable with almost no cementing material. However, irregular masses are cemented with calcium or silica and form dense sandstone (Schwartz 1939). The sandstone is typically white but where water is able to infiltrate, iron oxide stains the sand grains yellow, brown, or red (Sardeson 1896). Sand grains are cemented by iron oxide into dark brown nodules that are dense and hard. Below a conspicuous layer of green sand, iron staining of the sand grains diminishes rapidly with depth. X-ray diffraction of the green sand shows well-defined peaks for illite (Payne 1967). Just below this green sand layer the highest occurrence of iron nodules are found. These iron nodules also diminish rapidly in size and number with depth.

A unique quality of St. Peter sandstone is that, unlike most sandstones or sand deposits, the grains of St. Peter sandstone become more angular as the grain size decreases. This is a reversal of normal grain shape patterns where the grains become more rounded as they decrease in size. This reversal in grain shape could be the result of preferential transport mechanisms of Pre-Devonian times.

Laboratory Tests

The construction of a large cavern within St. Peter sandstone on the campus of the Univ. of Minnesota provided an opportunity for studying the mechanical behavior of this material. Conventional triaxial testing was conducted on intact specimens to verify the strength characteristics of St. Peter sandstone, with results (Fig. 2) similar to Watson (1938). It proved difficult, however, to measure dilatancy behavior, which may be needed to explain the large angle of internal friction associated with the material. For this reason, as well as for ease of testing and specimen preparation, it was decided that further testing would be conducted under direct shear. Both intact and pulverized sandstone specimens in dry and saturated conditions were tested in direct shear to evaluate friction and dilatancy. Uniaxial tests were conducted on dry, intact specimens to estimate elastic properties. All tests were performed at a strain rate of less than 10^{-4}/s under drained conditions.

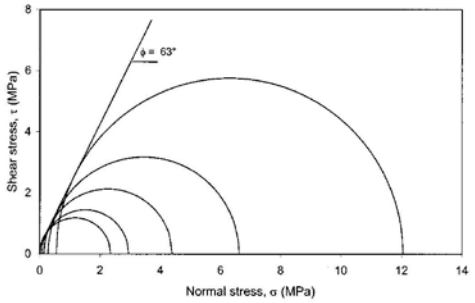

Fig. 2. Failure envelope and strength parameters of intact St. Peter sandstone from triaxial compression tests (Labuz et al. 1998)

Index Tests

The average dry unit weight of the intact St. Peter sandstone tested was 19 kN/m^3, with a corresponding porosity value of 27% (voids ratio of 0.37), in reasonable agreement with values other researchers have reported (Schwartz 1939; Payne 1967; Dusseault and Morgenstern 1979). Grain size analysis was performed on samples taken at elevations of approximately 229 and 224 m. An unnamed green sand layer is at an elevation of ~228 m. St. Peter sandstone above the green sand layer is heavily stained with iron oxides, while below the green sand layer, oxidizing fluids rapidly diminish with depth, and as a result of this, oxide staining diminishes as well. Iron oxide nodules are prominent; some are large, and the iron nodules also diminish in size and frequency rapidly with depth. Along with this loss of oxidizing fluids comes a significant change in color. St. Peter sandstone below this green sand layer takes on the characteristic white color and a substantial change in grain-size distribution. The effective grain size (D_{10}) and coefficients of uniformity (C_u) and gradation (C_c) are given in Table 1.

According to the Unified Soil Classification System (USCS), St. Peter sandstone at the 229 m elevation can be classified as a poorly graded, angular to well rounded, medium to fine-grained lightly rust-colored sand with little fines. For St. Peter sandstone samples taken from the 224 m elevation, the grain size distribution shifted significantly toward smaller grain sizes and was much more evenly distributed from the #60 to #200 sieve sizes. The sandstone from an elevation of 224 m was poorly graded, angular to well rounded, medium to fine-grained white-colored sands with little fines and infrequent occurrences of iron nodules that were 0.25–0.43 mm in size.

Specimen Preparation

St. Peter sandstone is extremely friable and shaping must be done by hand on dried samples. Blocks, approximately 250 mm on a side, were cut out of the floor of the Minnesota Library Access Center with an electric chainsaw. The blocks were quartered, and these samples were oven dried for 24 h at 105 °C. The intact samples were trimmed with a hacksaw and a steel square to within 1.0 mm of the dimensions of the shear box, and then pressed into the shear box. The sandstone can be cut easily, but considerable care needs to be taken or the specimens break, rendering them useless. The edges of the box performed the final act of trimming, resulting in a specimen that matched the inside dimensions of the shear box. The height from the top of the specimen to the top of the shear box was measured in each corner and an average value was taken assuming that the surface of the specimen was planar. The typical voids ratio was 0.38.

The pulverized specimens were produced by taking pieces roughly 100 mm in diameter and gently breaking them down within a metal container. The sandstone is friable and easily separated into individual particles. The loosely packed samples were poured into the shear box through a funnel, and then smoothed approximately parallel and within 5–10 mm of the top of the shear box. The average voids ratio was 0.65. The densely packed samples were poured into the shear box in five lifts and each lift was vibrated with ten taps from an 8 oz hammer on each side of the shear box. The samples were then smoothed until they were approximately parallel and within 5–10 mm of the top of the shear box. The average voids ratio was 0.46.

The direct shear tests, for both intact and pulverized St. Peter sandstone specimens, were performed with a GEOTEST (Evanston, IL) model S2215A direct shear machine, which conforms to all aspects of ASTM D3080 and U.S. Army Corps of Engineers standards. Measurements used to establish unit weights of intact, loosely packed, and densely packed specimens were made in the standard square, 102 mm shear box.

Table 1. Gradation Characteristics at Two Elevations

Sample elevation (m)	D_{10} (mm)	D_{30} (mm)	D_{60} (mm)	C_u	C_c
~229	0.214	0.331	0.515	2.407	0.994
~224	0.095	0.136	0.208	2.189	0.936

Direct Shear Tests

The volume change response of intact St. Peter sandstone is shown in Fig. 3. An increase in applied normal stress was associated with a decrease in dilatant behavior, which produces a nonlinear failure envelope over a large range of confinement (Fig. 1). At very low normal stress (5 kPa), the sandstone displayed no compaction. The dilation rates at the peak states (shear displacement of 1–1.5 mm) were more or less constant at a given stress level. Fig. 4 illustrates the mechanical behavior of the sandstone and the sand. The softening response of the intact rock was associated with fracture. The large peak strengths were indicative of significant dilation rates.

Assuming that the deformation was confined to a zone of height, h, the thickness of the shear band, and neglecting elastic deformation, the dilatancy behavior can be estimated. The intact St. Peter sandstone specimens exhibited dilation angles at failure from 45° at 19 kPa normal stress [Fig. 5(a)] to 21° at 152 kPa normal stress [Fig. 5(b)]. These dilation angles were much larger than the loosely packed (4–3°) or even densely packed sand, which showed dilation angles from 14° to 12° [Figs. 5(a and b)]. Examination of Fig. 5(a) shows that initially there was almost no contraction at low normal stress (<19 kPa) for the sandstone and the dense sand. With higher normal stress (>152 kPa), as shown in Fig. 5(b), the intact sandstone started to behave more like the densely packed sand, though the dilation angle at failure (21°) remained larger than the densely packed sand specimens (12°). The volume change behavior of the sandstone at the residual state was similar to the densely packed sand at large normal stress [Fig. 5(b)].

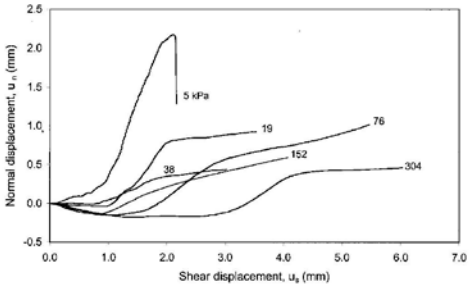

Fig. 3. Dilation of intact St. Peter sandstone over range of normal stresses

The 57–63° angle of internal friction at failure for the intact rock (Figs. 2 and 6) has been postulated to be a result of St. Peter sandstone being a locked sand (Dusseault and Morgenstern 1979) or a result of true mineral contact (Means and Parcher 1963). In addition, postdepositional quartz overgrowths forming an "interlocking finger effect" (Pittman 1972; Mazzullo and Ehrlich 1983) may contribute to the large friction angles. These effects are lost when the sandstone is recompacted. Examining Figs. 1 and 6, it is evident that there is a substantial change in the slope of the failure envelope for the intact material. Watson (1938) and Dusseault and Morgenstern (1979) also assign a curved failure envelope to intact specimens. The nonlinear response can be attributed to the increasing normal stress subduing the dilation.

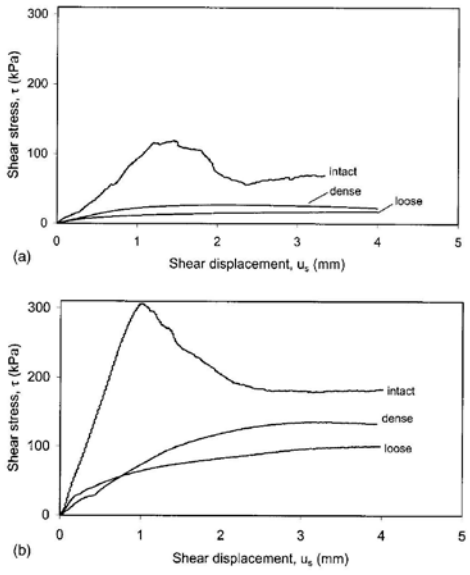

Fig. 4. Mechanical response of St. Peter sandstone in direct shear: normal stress of (a) 19 kPa and (b) 152 kPa

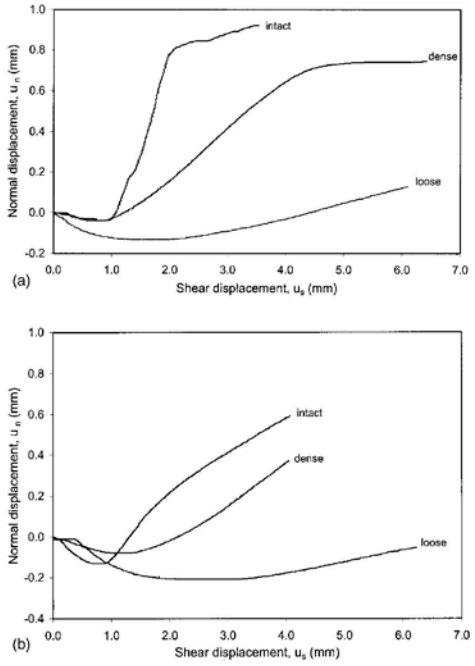

Fig. 5. Dilation of intact and recompacted (densely and loosely packed) St. Peter sandstone: normal stress of (a) 19 kPa and (b) 152 kPa

The behavior of St. Peter sandstone under saturated conditions in direct shear was more complex. The breakdown of cohesion of the intact specimens was apparent (Fig. 7). Furthermore, the Mohr–Coulomb failure envelopes showed that the friction angle was reduced by the presence of water, from 57 to 46°; linear failure envelopes were constructed as best-fit lines in a least-squares sense for the intact dry and saturated specimens. The reduction in friction may have been due to the dissolution of calcium and iron oxide, and to the small amount of impurities such as clay and hematite in the form of flakes and laminae on some St. Peter sandstone grains. Loss of cementation upon wetting was also described by Schwartz (1939). He placed a specimen in a beaker on a rubber stopper and the beaker was filled with water until approximately 1 mm of the sandstone block was submerged. The sample was covered with a damp towel for sev eral hours and subsequently tested. The block failed at a stress of 4 kPa. Another specimen was tested dry and failed at a stress of 993 kPa. Thus, moisture has a significant effect on the cohesion of the material.

Uniaxial Compression Tests

Uniaxial compression tests were conducted on dry, intact specimens with diameters of 50–100 mm. All cores were shaped to maintain an approximate aspect ratio of 2:1. The cores were tested in a closed-loop, servo-hydraulic load frame in an attempt

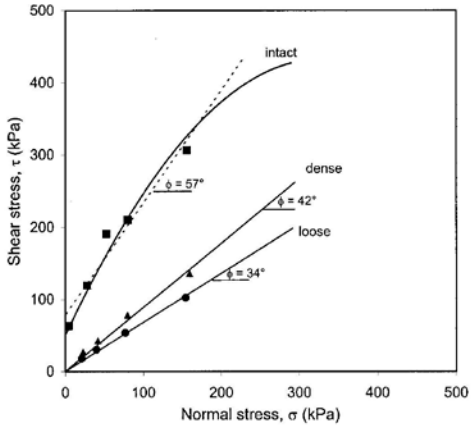

Fig. 6. Failure envelopes of St. Peter sandstone and sand in direct shear

to acquire information on the peak state and the softening response. The system was controlled by the *TESTSTAR* (MTS Systems, Minneapolis, MN) software package, which also provided the ability to sample data such as load, axial displacement, and lateral displacement at discrete intervals. A constant axial displacement rate of 0.10 mm/min was used for all tests.

To determine axial strain, the overall change in length was measured; this deformation included contact at the specimen-platen interface, which contributed to the nonlinearity at the initial loading (Fig. 8). Machining the ends of St. Peter sandstone to a reasonable tolerance (<1 mm) was difficult. Lateral strain was estimated from digital displacement gauges with point contacts

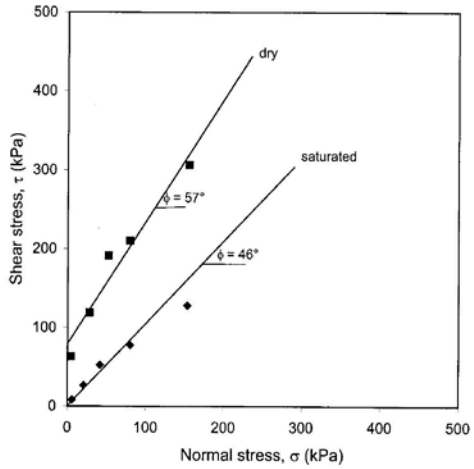

Fig. 7. Failure envelopes of intact St. Peter sandstone in direct shear

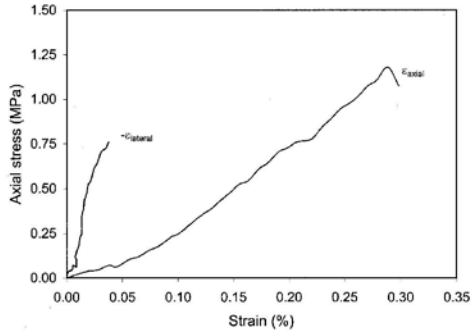

Fig. 8. Mechanical response of intact St. Peter sandstone in uniaxial compression

that measured radial displacements to an accuracy of 0.001 mm. Three gauges were mounted 120° apart on an adjustable plate placed at the midheight of the specimens. The radial deformation was determined by averaging the three sensors. The point contacts of the probes contributed to spurious signals once microcracking localized and surface spalling occurred. The test results indicated a Young's modulus of 0.4–2.0 GPa (a mean value of 1.1 GPa) and a Poisson's ratio of 0.2–0.33 at axial strain levels of 0.05–0.1% (Fig. 8). The negative value of the lateral strain is shown up to a stress level of approximately 50% of the peak stress; beyond this point localized deformation was detected and further readings were not representative of an element response. Compressive strength of the dry specimens varied from 0.6 to 2 MPa.

Thin Section Analysis

The effort behind thin section analysis was to offer some insight into the locked sand and/or postdepositional overgrowth theories for the large angle of internal friction. Due to the friable nature of St. Peter sandstone, considerable care was necessary to make the thin sections, which were studied using both transmitted plane polarized light and scanning electron microscopy (SEM).

Locked sands (Dusseault and Morgenstern 1979) exhibit almost no contraction while being tested in direct shear, have very high rates of dilation at failure, and subsequently have peak frictional strengths considerably higher than strengths exhibited by dense sands. As normal stress is increased, the high dilation rates are subdued, resulting in a nonlinear failure envelope. The peculiar fabric that locked sands develop is attributed to diagenetic processes that reduce porosity while leaving an essentially uncemented structure. The result of these processes is sand with increased strength due to its high dilatancy (Dusseault and Morgenstern 1979).

Transmitted light and scanning electron microscopes were used to identify interlocking textures and interpenetrative contacts. These contacts are dependent on variations in solubility as a result of impurities, and differences in radii of curvature, resulting in the smaller grain penetrating into the larger grain [Fig. 9(a)]. It is important to note that impurities such as clay and hematite occur on St. Peter sandstone grains in the form of flakes and laminae. These impurities favor pressure solution over secondary quartz (Pittman 1972).

Postdepositional quartz overgrowths may be responsible for an "interlocking finger effect" (Pittman 1972; Mazzullo and Ehrlich 1983). The growths may occur with poorly defined crystal faces that form an interconnected anastomosing system over the grain's surface, or isolated with well-defined crystal faces [Fig. 9(b)]. It is also common to see the formation of secondary quartz growths in the form of incompletely developed crystal faces resulting from the merger of irregular overgrowths (Pittman 1972). The surface of loose grains yielded some evidence of postovergrowths on larger grains. Fig. 9(c) shows not only a point contact depression in the surface of the grain, but there is also a tear in the grain's surface starting within the depression and moving out beyond the rim.

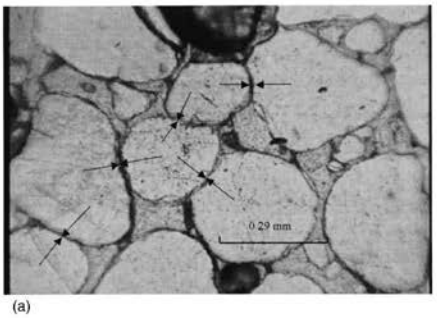

(a)

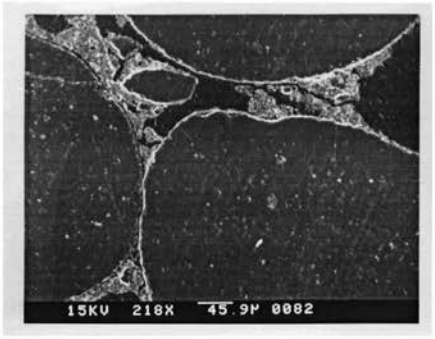

(b)

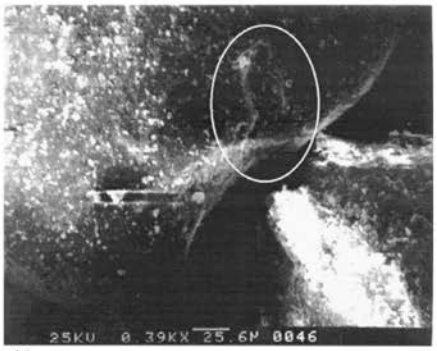

(c)

Fig. 9. (a) Transmitted light micrograph of intact St. Peter sandstone showing locked grains. (b) Micrograph of St. Peter sandstone showing grain contacts. (c) Micrograph of St. Peter sand grain surface showing contact depression and evidence of tearing of grain surface, possibly due to postdepositional quartz overgrowths.

Field Testing—The Pressuremeter

For hard to sample materials, such as St. Peter sandstone, the pressuremeter test offers an alternative to laboratory testing in order to obtain modulus and shear strength through direct measurements and the use of established theories. The pressuremeter is a test that, when properly performed, can replace some routine laboratory testing on the grounds of both improved accuracy and more favorable economics (Briaud 1992). When testing soils, bladder resistance becomes an important calibration factor, whereas system stiffness is not taken into account because soil is sufficiently compliant and the system can be taken as infinitely stiff. For relatively stiff materials, such as St. Peter sandstone, system stiffness is critical and a correction for system displacement is necessary.

The pressuremeter apparatus was calibrated using a tube with approximately the same dimensions as the probe assembly. The grade 60 steel (Young's modulus of 205 GPa and Poisson's ratio of 0.3) tube was 984 mm long with an inside diameter of 76.2 mm and a wall thickness of 3.1 mm. The calibration tube was instrumented with three Measurements Group (Raleigh, N.C.) type EA-06-250BG-120 strain gauges mounted at 120° intervals and arranged to measure tangential strain (ε_θ).

Stress analysis follows from the Lame' solution, and the expressions for calculating radial and tangential stresses and radial displacements are well known (Dally and Riley 1991). For the case of the calibration tube, the external pressure $p_o = 0$. The calibration test itself was performed by injecting fluid into the probe in pressure steps of 500 kPa until the system reached its maximum pressure of 10 MPa. Strains were recorded 30 s after the pressure step was reached. The system stiffness was estimated to be 150 kPa/cm^3, which was of the same order as the stiffness of the sandstone.

Initially, boreholes for pressuremeter testing were drilled horizontally into the excavation face. These attempts were met with difficulties, notably spalling in the borehole. The spalling events started approximately 0.75 m in from the excavation face and proceeded into the back of the borehole. The spalls peaked approximately 40 mm above the top of the borehole. Whether the spalling was a result of gravity breakout or a result of $\sigma_{hor} > \sigma_{ver}$ is not known.

Vertical boreholes were drilled into the floor using a 753 Bobcat with a drill attachment and modified auger stems. These auger stems were cut and recapped to 76.2 mm. This assembly was capable of drilling vertical boreholes that were nominally 77 mm in diameter and up to 3 m in depth. Three Menard-type (stress-controlled) tests were conducted at a depth of 1–2 m below the surface in wet St. Peter sandstone; the horizontal stress was estimated to be 15–30 kPa. Fluid was injected into the probe to achieve pressure increments of 1 MPa, one-tenth of the maximum pressure (10 MPa) allowed by the system. Readings of injected volume were taken at time zero, 30 s, and 60 s. The results from borehole #3, corrected for system stiffness, are shown in Fig. 10(a).

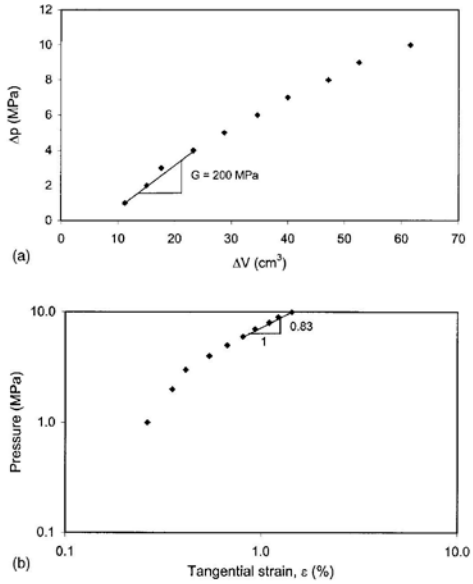

Fig. 10. Pressuremeter test results: (a) mechanical response of wet intact St. Peter sandstone, (b) method for estimating friction angle

Elasto-plastic analysis

The deformation of an elastic solid due to a pressurized hole is directly related to the shear modulus (G) of the material. To calculate Young's modulus, E, an additional elastic parameter must be known. It is typical to assume a value of Poisson's ratio, ν. For St. Peter sandstone, a value of 0.33 was used. Young's modulus was determined by analyzing Δp_i vs ΔV [Fig. 10(a)] for tangential strains on the order of 0.01%. From the three different boreholes, E was 340, 535, and 700 MPa, a mean value of 520 MPa, somewhat lower than the laboratory tests, although an unload-reload cycle was not attempted. The initial modulus is affected by sample disturbance, especially at the small strain levels associated with the relatively stiff sandstone. It should be mentioned that the stiffness correction of the system was critical, as E determined without the correction was reduced by a factor of 2.

The angle of internal friction (ϕ) and the angle of dilation (δ) can be estimated from pressuremeter tests by utilizing an elasto-plastic analysis (Hughes et al. 1977; Fahey 1986; Fukagawa et al. 1998). The expanding pressuremeter can be assumed to deform the sandstone under conditions of axial symmetry and plane strain (Palmer 1972); both experiments and numerical analyses support these assumptions (Hartman and Schmertmann 1975; Laier et al. 1975). Because of axial symmetry, the principal stresses acting on an element of the sandstone are $\sigma_r, \sigma_\theta, \sigma_z$ and the strains are given by

$$\varepsilon_r = -\frac{du}{dr}, \quad \varepsilon_\theta = -\frac{u}{r}, \quad \varepsilon_z = 0 \tag{1}$$

where u=radial displacement and compression is taken as positive.

As pressure increases within the hole of radius a, the failed zone ($a<r<b$) of radius b develops where the sandstone obeys the Mohr–Coulomb failure criterion

$$\sigma_\theta = N\sigma_r - 2c\sqrt{N} \tag{2}$$

where $N=(1-\sin\phi)/(1+\sin\phi)$ and c=cohesion

Total stresses were used because the sandstone was wet and pore pressures were not known. Substituting Eq. (2) into the differential equation of equilibrium and integrating using the boundary condition $\sigma_r(b)=\sigma_b$ yields

$$\ln\frac{\sigma_r+T}{\sigma_b+T} = (1-N)\ln\frac{b}{r} \tag{3}$$

$$T = 2c\frac{\sqrt{N}}{1-N} \tag{4}$$

Neglecting elastic deformation, which is reasonable when the normalized shear modulus G/p_h (p_h is the in situ horizontal stress) is large, the ratio of volumetric strain ϑ to shear strain γ can be represented by the dilatancy angle δ

$$\sin\delta = -\frac{(\dot{\varepsilon}_r+\dot{\varepsilon}_\theta)}{(\varepsilon_r-\varepsilon_\theta)} = -\frac{\dot{\vartheta}}{\dot{\gamma}} \tag{5}$$

where the dot represents a small increment. As principal strains do not rotate during a pressuremeter test, the sum of the incremental strains equals the total strains such that the flow rule is

$$\varepsilon_r = -n\varepsilon_\theta \tag{6}$$

$$n = \frac{1-\sin\delta}{1+\sin\delta} \tag{7}$$

Eq. (6) may be rewritten by making use of Eq. (1), integrating, applying the boundary condition $\varepsilon_b=u(b)/b$, and using Eq. (3) to give

$$\varepsilon = (\varepsilon_b)\left\{\frac{p_i+T}{\sigma_b+T}\right\}^{(n+1)/(1-N)} \tag{8}$$

where $\varepsilon=u(a)/a$ is obtained from the pressuremeter test. Taking the logarithms of both sides, with $T \ll p_i$ and ε_b=constant, predicts a linear relationship between $\log p_i$ and $\log\varepsilon$. The slope of this straight line is designated S

$$S = \frac{1-N}{n+1} = \frac{(1+\sin\delta)\sin\phi}{1+\sin\phi} \tag{9}$$

Determining ϕ and δ requires that the pressuremeter data be converted from Δp vs ΔV to $\log p_i$ vs $\log\varepsilon$, as shown in Fig. 10(b). With S determined graphically [Fig. 10(b)], friction angles of 56° (S=0.829 for borehole #3) and 61° (S=0.875 for borehole #4) were calculated by assuming associative behavior. However, the requirement that $\phi=\delta$ yields dilatancy angles that are too large. Although a dilatancy angle of 45° was estimated from a direct shear test at a similar stress level as the pressuremeter tests (15–30 kPa), the axisymmetric, plane strain condition in the field would limit volume change. For elastic response, no volume change occurs. If nonassociative behavior is considered with the angle of internal friction taken between 57 and 69°, the range of the obliquity angles measured in the laboratory tests, the dilatancy angle δ is estimated to be 50–41° (Fig. 11), which is still rather large.

Several items related to the difference in laboratory and field conditions should be mentioned. The friction angles estimated

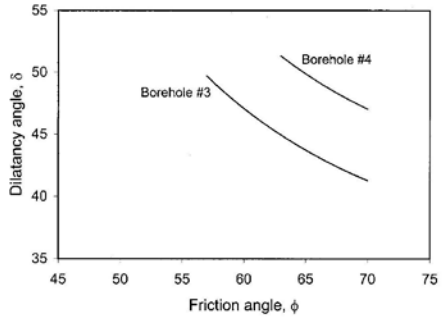

Fig. 11. Possible range of dilatancy angles

from the field testing were associated with total stresses, as effective stresses were not known. The pressuremeter tests were influenced by pore suction (the sandstone was wet) and borehole disturbance. Because the strain levels associated with failure were less than 1%, sample disturbance may influence the results. Also, a small amount of cohesion that may have been present in the wet sandstone was neglected in the analysis, as was the elastic behavior of the soft rock. These assumptions may have contributed to the overestimate of the dilatancy angle.

Conclusions

St. Peter sandstone is a unique formation that exhibits characteristics of both rock and soil. When confined, it is capable of supporting large loads with small deformations, even under saturated conditions, yet when confinement is removed it disintegrates and readily flows. If dry intact specimens are subjected to unconfined compression, then St. Peter sandstone exhibits values of a uniaxial strength (approximately 1 MPa) and a Young's modulus (approximately 1 GPa) associated with an overconsolidated cohesive soil, but sampling the material poses significant difficulty.

The purpose of this project was to evaluate mechanical properties of St. Peter sandstone by in situ testing, and to compare field and laboratory results. Direct shear tests were conducted to evaluate the strength-dilatancy behavior, and microscopy analysis was used to help explain the significant friction angles associated with the material. St. Peter sandstone is nearly cohesionless, but it possesses a friction angle of about 60° at low confinement. The large angle of internal friction at failure may be due to locking of sand particles or to postdepositional quartz overgrowths. Tests on pulverized densely packed and loosely packed sand specimens were performed in the same manner as the intact specimens and yielded friction angles of 42 and 34°.

Pressuremeter tests were performed at a depth of 1–2 m within a wet sandstone and the results were interpreted using an elasto-plastic analysis. Young's modulus was found to be around 0.5 GPa, slightly lower than the laboratory value, possibly due to sample disturbance at the small strain levels. Appropriate consideration of system stiffness was critical for the determination of modulus. Although the friction angles were within the range of values measured in the laboratory, the dilatancy angles were overestimated from the field tests. Ignoring elastic displacement and slight cementation may have contributed to the observed behavior. Furthermore, effective stresses were not known, so the angle of internal friction was associated with total stresses. As with the modulus estimate, the effect of disturbance may be significant, because the strain at failure was less than 1%.

Acknowledgments

This research was partially supported by the National Science Foundation (CMS-9604684) and the Center for Transportation Studies of the Univ. of Minnesota. CNA Consulting Engineers (Minneapolis) assisted with the sampling and field testing.

References

Amaral, E. J., and Pryor, W. A. (1997). "Depositional environment of the St. Peter sandstone deduced by textural analysis." *J. Sediment. Petrol.*, 47(1), 32–52.

Briaud, J. L. (1992). *Pressuremeter*, Balkema, Rotterdam, The Netherlands.

Dally, J. W., and Riley, W. F. (1991). *Experimental Stress Analysis*, McGraw-Hill, New York.

Dusseault, M. B., and Morgenstern, N. R. (1979). "Locked sands." *Q. J. Eng. Geol.*, 12, 117–131.

Fahey, M. (1986). "Expansion of a thick cylinder of sand: A laboratory simulation of the pressuremeter." *Geotechnique*, 36, 397–424.

Fraser, G. S. (1976). "Sedimentology of a middle Ordovician quartz arenite-carbonate transition ni the Upper Mississippi Valley." *Geol. Soc. Am. Bull.*, 86, 833–845.

Fukagawa, R., Muro, T., Hata, K., and Hino, N. (1998). "A new method to estimate the angle of internal friction of sand using a pressuremeter test." *Proc., 1st Int. Conf. Site Characterization*, 2, 771–775.

Hartman, J. P., and Schmertmann, J. H. (1975). "FEM study of elastic phase of pressuremeter test." *Proc., In Situ Measurement of Soil Properties, ASCE Specialty Conf.*, Raleigh, N.C. 1, 190–207.

Hughes, J. M. O., Wroth, C. P., and Windle, D. (1977). "Pressuremeter tests in sands." *Geotechnique*, 27(4), 455–477.

Labuz, J. F., Zietlow, W. K., and Chen, L-H. (1998). "Laboratory testing for the Minnesota Library Access Center." *Tech. Rep.*

Laier, J. E., Schmertmann, J. H., and Schaub, J. H. (1975). "Effect of finite pressuremeter length in dry sand." *Proc., In Situ Measurement of Soil Properties, ASCE Specialty Conf.*, Raleigh, N.C., 1, 241–259.

Mazzullo, J. M., and Ehrlich, R. (1983). "Grain-shape variation in the St. Peter sandstone: A record of eolian and fluvial sedimentation of an early Paleozoic cratonic sheet sand." *J. Sediment. Petrol.*, 53(1), 105–119.

Means, R. E., and Parcher, J. V. (1963). *Physical properties of soils*, Merrill, Columbus, Ohio.

Palmer, A. C. (1972). "Undrained plane-strain expansion of a cylindrical cavity in clay: A simple interpretation of the pressuremeter test." *Geotechnique*, 22(3), 431–457.

Payne, C. M. (1967). "Engineering aspects of the St. Peter sandstone in the Minneapolis-St. Paul area of Minnesota." Master's thesis, Univ. of Arizona, Ariz.

U.S. Army Corps of Engineers, St. Paul District. (1939). *Permeability tests on St. Peter sandstone specimens*.

Petersen, D. L. (1978). "Estimating the strength of St. Peter sandstone pillars." Master's thesis, Univ. of Minnesota, Minn.

Pittman, E. D. (1972). "Diagenesis of quartz in sandstones as revealed by

scanning electron microscopy." *J. Sediment. Petrol.*, 42(3), 507–519.
Sardeson, F. W. (1896). "The Saint Peter sandstone." *Minnesota Academy of Natural Sciences*, 4, Paper D, 64–88.
Sardeson, F. W. (1932). "The Saint Peter group of Minnesota." *Pan Am. Geo.*, 58(3), 191–196.
Schwartz, G. M. (1939). "Foundation conditions at the sites of the proposed St. Anthony Falls locks Minneapolis, Minnesota." *Rep. to the U.S. Army Corps of Engineers*, St. Paul District.
Thiel, G. A. (1935). "Sedimentary and petrographic analysis of the St. Peter sandstone." *Bull. Geol. Soc. Am.*, 46, 559–614.
Watson, J. D. (1938). "Triaxial compression tests on St. Peter sandstone." *Rep. to the U.S. Army Corps of Engineers*, St. Paul District.